Multi-Spatial-Mode Quadrature Squeezing from Four-Wave Mixing in a Hot Atomic Vapour

By

Matthew Turnbull

A thesis submitted to the

University of Birmingham

for the degree of

DOCTOR OF PHILOSOPHY

Midlands Untracold Atoms Research Center

School of Physics and Astronomy

University of Birmingham

August 2, 2013

UNIVERSITY OF
BIRMINGHAM

University of Birmingham Research Archive

e-theses repository

This unpublished thesis/dissertation is copyright of the author and/or third parties. The intellectual property rights of the author or third parties in respect of this work are as defined by The Copyright Designs and Patents Act 1988 or as modified by any successor legislation.

Any use made of information contained in this thesis/dissertation must be in accordance with that legislation and must be properly acknowledged. Further distribution or reproduction in any format is prohibited without the permission of the copyright holder.

Abstract

Noise suppression across multiple spatial modes of a light field would serve to improve the field's imaging capabilities and allow it to act as a more effective carrier of quantum information. This thesis describes a scheme that utilises a nonlinear process (four wave mixing (4WM)) in ^{85}Rb in order to generate a single beam of light that demonstrates sub quantum noise limit (QNL) quadrature fluctuations of up to -4dB across a multitude of spatial modes simultaneously.

Included is a description of sub-QNL (squeezed) light, followed by a breakdown of how this 4WM arrangement generates the desired quantum noise suppression. Analysis has been performed that displays explicitly how the phase matching arrangement that maximises the noise suppression differs from that which optimises the efficiency of the process. This consideration is crucial to understanding why the setup achieves the levels of squeezing observed despite the presence of a strong absorption feature.

Finally, the multi-spatial-mode nature of the generated squeezing is observed directly via homodyne detection using local oscillators with a range of transverse profiles. These profiles select the mode of the signal to be analysed and as such the ability to detect squeezing using a range of them demonstrates its presence across all of these modes simultaneously.

Acknowledgements

This document has taken me the best part of four years to arrive at. But to even arrive at the starting point of those four years took another twenty two. If you'd told a 12 year-old me that one day I'd be finishing a Physics PhD, I'd probably have been fairly incredulous, but first you'd likely have to establish what a PhD actually was.

Firstly, my greatest of thanks have to go out to Dr Vincent Boyer, my supervisor, who accepted me onto this program and was one of the greatest teachers I've ever had the joy to operate under. It is through his expertise, skill at conveying this knowledge and constant attendance and patience that any of this was possible. Other thanks must go to those who helped work on the project through the years, including Etienne Pertreux, who helped take some of the preliminary data for the phase matching experiment, Plamen Petrov who brought his post-doctoral knowledge into the project and Christopher Embrey, who was constantly helpful and now continues this research in my stead. I hope my notes were useful enough. Also for providing invaluable contributions and a welcome second-sight at my research my thanks go out to my Viva-ing pair Andre Kaplan and Sonja Franke-Arnold.

Thanks also to two people I have in fact never met, but whose work was enormously useful in terms of their achievements in analysing the theoretical framework of the four-wave mixing process under consideration. Alberto Marino and Quentin Gloreaux, two of the giants on whose shoulders this work is assembled.

Prior to the PhD, my meeting with Dr Boyer was facilitated in relation to my masters work under Professor Kai Bongs, coincidentally another of the greatest teachers I have known. His friendly running of the entire group made it a joy to be a part of during my five years there, the first of which was spent largely under his tutelage as I cut my teeth learning about cold atomic systems and experimental design from one of the best. Myself and my partner were aided throughout this by Dr

Mike Holynski (then a starting PhD student) and Dr Jochen Kronjaeger (post-doc and electronics guru) with the project (aim: to build a MOT) finally coming to completion at the hands of a collection of 3rd year students, some years later, but in the same system originally put together by ourselves. Thankyou to all involved for making the project a success and for gifting me all the knowledge used in doing so.

My undergraduate time at the University of Birmingham was fantastic overall, with a wide range of influential lecturers and demonstrators helping me through my four years. Special thanks must go to Dr David Evans, head of the first year labs, where I demonstrated for four years after having first gone through them myself, and Dr Chris Mayhew, partly responsible for my being on the course in the first place, being as he was the admissions tutor at the time.

Continuing my education back still further I must give a mention to my high-school physics teachers, specifically Mr Thomas-hay, whom again without his enthusiasm and approach to teaching physics, I would never have taken this route.

But there's been more to all this than the work and the education, more to why my time at Birmingham was so special, and mostly that's down to the people I spent my time with. From the office of 213a to Staff House to international trips, every second spent in the company of these people was a pleasure, and apologies, but this might result in a fairly long list so to keep it simple, I'll group then list alphabetically. From the office, I would like to thank Mathis Baumert, Mark Brannan (learned scholar of Glasgow), Wei He, Mike Holynski (Innocent prank master), Steve Johnson, Ole Kock (our guide to Hamburg), Nadine Meyer (defenestrator), Charlotte O'Neill, Marisa Perea (all businesss), and Amy Rudge. From the wider floor there's Vincent Boyer, Kai Bongs, Rob Culver, Chris Embrey, Chris Gill, John Goldwin, Andrew Hinton, Alex Holmes, Jochen Kronjaeger, Komal, Rich Lycett, John Malcolm, Lawrence Mudarikwa, Alex Niggebaum, Plamen Petrov, Emanuele Rocco, Yeshpal Singh, Lyndsie Smith, Tristan Valenzuela and Dominick Walliman. Over in the Astro group

I need to thank Charlotte Bond, Mark Burke (awarded Most Appropriate 2011-2012), Chris Collins (awarded Most Inebriate, same year), Carl-Johan Haster, Ilya Mandel and Trever Sidery. Lasting friendships from my time as an undergraduate necessitate mentions of Heather Audley, Al Cameron, Martin Cuddy (quiz master), Laura Harper (Ski master), (Chancellor) Brigid Jones, (Chancer) Matt Lazell, Amy Perry, Jim Phillips, Tony Price, Patrick Scott, Sarah Townson, and on the 'non-physicist tagalong' side we have John Boissonade, Emily and Ben Gravestock, Hannah Lake, Claire Sacre, Andrew Slattery, Jim Smyth, and Peter Rothery.

Deserving of their own section are the paintball club, which I first joined as a fresher and over time built up some long-lasting friendships that have lasted beyond many of their times at Birmingham. While there was some physics crossover more often it was nice to have access to an entire group of others with no real interest in what I was doing on a daily basis. Here's to Gurpreet Bhaath, Jessie Blaynee, Andrew and Emma Bridges, Sam Burt, Richard Charlton, Greg DeQuidt, Phil Duxbury, Tom Farmery, Martin Fitzpatrick, Simon Menashy, Fabian Neuner, Francis Shaw, Steve Simpson, Charlie Thouaille, and Steve Hancock, the puppetmaster.

Through the whole time I've been backed also by the love and support of my family. My mum and dad, sister, stepsister and Simon Greatrix and Nicky White. Thanks so much to all of you for always being there.

Finally three people who haven't yet been mentioned, but deserve highlighting. These three all fall into the catagory of fellow undergrad physicists, but have since become my closest friends. Always there when needed be it socially, academically or just for a quick catchup. Byron, Rory and Sameera, this one's for you.

Contents

List of Figures

Introduction

Imaging is a term used to describe the transmission or recreation of information about a physical object's spatial profile that has been encoded in the form of light. We are all familiar with a variety of imaging systems ranging from the eyeballs in our skulls to the cameras in our phones. The optical elements that comprise such systems are all generally well understood and many have been almost second nature for many years, i.e. mirrors in bathrooms, lenses in glasses or filters in sunglasses. All of these act as tools to affect the incident light fields and present our eyes with the information required.

In science, imaging techniques are often used to show us things not visible to the naked eye, whether it's using a telescope to view images of distant galaxies or a camera to image a Bose-Einstein condensate. The ability of an imaging system to accurately recreate fine details present in the original object is of absolute importance in imaging, and was long thought to be limited ultimately by the laws of classical physics.

Over the last ten to twenty years, methods of overcoming these classical imaging limitations have been developed that take advantage of the quantum nature of the light field. This research is termed quantum imaging, a relatively young field that has developed out of investigations into quantum optics. Quantum imaging asks if we can take our knowledge about the quantised nature of the light field and apply it to the field of imaging, where multiple spatial modes of the field are considered, i.e. those

that characterise the transverse structure of the field, in order to improve imaging techniques or alternatively to investigate new forms or mechanisms for imaging purposes. Notable achievements in the field have been to produce, for example, images of objects in the absence of any direct scattering of the light (known as Ghost Imaging [1]) or the generation of a focussed point of light with spatial fluctuations on its central position below the level allowed by the quantum noise limit (QNL) (known as a quantum laser pointer[2]). A review of the field conducted in 2002 [3] listed a selection of uses and directions for research focus, including the observation of weak amplitude/phase objects[4], quantum optical lithography[5] [6], reduced displacement measurement [7], image amplification[8], increased optical resolution[9][10], as will discussed in this thesis, and more. The factor all of these studies have in common is that they utilise the higher order spatial modes of the light field, rather than simply the overall amplitude or phase of the beam.

In classical imaging, the diffraction limit of resolution is given by the Rayleigh criterion[11](defined in chapter 1). However, there exist a range of 'super-resolution' techniques[12][13][14] that can be put in place to try and extract a more detailed description of the original object from the information received from the field. The limiting factor in the effectiveness of some of these techniques is the degree of the light field's amplitude variance [9]. In other words the key limiting variable in the resolving capabilities of classical imaging is the level of amplitude noise.

All scientific measurements are limited to some level of precision by noise, errors produced on measurements by unavoidable factors such as statistical fluctuations on discrete data sets or electronic noise on detectors. As experiments aim to detect ever smaller signals with ever higher precision, a point has been reached in some cases where the effects of quantum uncertainty become the limiting factor in the experiment. In imaging, this fundamental quantum noise on the amplitude of the field is related to the Poissonian nature of the photon distribution within the field

and is referred to as the shot noise level (SNL). The first reduction in this distribution uncertainty came in the form of photon anti-bunching, described theoretically by both Kimble and Mandel[15] and Carmichael and Walls[16]. Photon anti-bunching refers to a photon stream featuring a sub-Poissonian photon distribution, and was first detected experimentally by Mandel et al in 1977 [17].

A widely used technique in recent years for noise reduction at such quantum-limited levels is known as squeezing and operates by, in effect, 'transferring' some of the uncertainty on a variable that is to be measured onto some conjugate variable whose precision is less important. The focus of this thesis is the usage of this squeezing technique to reduce the amplitude noise on a light field across multiple spatial modes, enabling the utilisation of this field as an imaging resource with noise below the SNL.

The concept of generating squeezing as a result of strong atomic coherence in a nonlinear medium was put forward by Reid in 1985 [18] and the first observation of the sub-shot noise continuous-variable amplitude fluctuations corresponding to squeezed light was in 1985 by Slusher [19] using a nonlinear optical process known as four-wave mixing (4WM) in sodium (Na) vapour. A measured reduction in the noise of 7% was recorded, and calculated to equate to a 20% drop when factors such as jitter and losses were taken into account. Limits on the optimal value of achievable squeezing via such an arrangement were estimated [20], with factors such as spontaneous emission and Doppler broadening being the main causes of reduced effectiveness.

Over the next ten years or so many further experiments were performed utilising 4WM in vapours in a variety of setups[21][22], including cold atoms [23], but these consistently showed what would today be considered low squeezing levels[1] (maximum

[1]The measure of a squeezed quantity is typically defined by how far the measured noise is reduced from the shot noise, measured on a log scale in decibels (dB). This is discussed further in section 1.4.

2.2 dB below the SNL) in comparison to other squeezed light techniques, such as 4WM in fibres [24][25][26] (used to show squeezing up to -4dB) and parametric down-conversion in crystals[27][28] (currently the squeezing champion with a record maximum of -12 dB at wavelengths of 1064 nm [29] and 1550 nm[30].) All these methods work on the principle of producing correlated photon pairs through nonlinear optical interactions between the field and the surrounding medium, as described in more detail in chapter 2.

The motivation for pursuing increasing degrees of squeezing extends beyond pure scientific endeavour as many practical purposes have been put forward for such states. These include improving the security of quantum communications by decreasing potential signal disruption[31] [32] or reducing the noise on ultra-sensitive interferometers[33], such as those used in gravitational wave detectors [34][35].

Due to the general limitations found when using vapours, even when cooled to ultra-low temperatures, the primary source of correlated photon pairs has long remained crystals, used successfully as sources for entangled photon pair-production and as optical parametric amplifiers (OPAs [36], used to increase the power of a seed beam by subtracting energy from some pump field) and oscillators (OPOs [37], used in the generation of additional frequencies of the field.) These have in fact been utilised to generate photon correlations across multiple spatial modes of the light field[38][39][40][41] as can be seen by using spatial light modulators [42]. For example, ghost imaging can build up the image of an aperture by integrating over a single photon count in many positions and measuring coincidence counts[43] and the entanglement between arbitrary orbital angular momentum (OAM) light modes has been demonstrated[44]. However, such systems operate in the single photon regime. Whilst the production of photon pairs demonstrates the highly correlated nature of the amplitudes, the intensity and gain of the system are all small in comparison to that seen in the continuous variable (CV) regime where bright beams are used

rather and individual photons. As will be shown in section 2.3.1, this gain level is intrinsically linked to the degree of squeezing produced. In this thesis we wish to view strong quadrature squeezing across multiple spatial modes in the CV regime, meaning such crystal-based nonlinear resources are inappropriate. Although crystals have been used to generate multi-spatial-mode (MSM) squeezed light by combining the output of a number of individual crystals, each resonant to a separate field mode [45] [46], this has yet to be performed across the number of modes needed to truly improve the imaging capability of the light source for an essentially arbitrary object.

A number of different avenues for MSM squeezed light have been pursued in addition to that presented here. A self-imaging cavity is one example, as posited in 1969[47], that operates by encasing the nonlinear medium inside a cavity designed to be degenerate across a number of spatial modes. Self-imaging occurs when the trajectory of a ray emitted with an arbitrary position/momentum within the resonant field follows a path that leaves it in its original position/direction after a round trip through the cavity. As such the cavity is to some extent spatially degenerate. This degeneracy implies the correlations on the output can be obtained for each simultaneously resonant spatial mode. This has been used to show the effects of correlated photon pairs in both the near and far-field regimes[48]. It has also been shown that once a squeezed state has been generated, the spatial mode it occupies can be altered with minimal reduction of the squeezing present [49], however it is still only present on a single spatial mode at any one time.

Temporal mode squeezing has also been experimentally detected[50], in which the shape of an applied pulse into a cavity containing a nonlinear medium is synchronised to the round-trip time of the cavity. In this manner the multi-mode degeneracy of the signal is across the frequency spectrum of the cavity emissions, rather than the spatial profile, in a manner akin to the lines on a frequency comb.

However in 2006, McCormick et al [51] found a high gain feature capable of

generating twin beams of similar intensity from heated Rb. Initially posited as a good source for viewing a slow light effect [52] it became apparent that due to the lack of a required cavity, the source might also be capable of generating strongly entangled multi-mode fields. That the emitted twin beams are entangled across multiple spatial modes was shown in 2008 [53]. Currently this source is being investigated in terms of its potential as a source of squeezed light[54], a low-noise quantum multi-spatial-mode amplifier[55] and, as shown here, a quantum imaging resource[56].

This thesis is generally concerned with the twin concepts of further investigating the feature at the source of this new-found squeezing centre and also a modification of the previous investigation into the entanglement of images by turning the results into a single beam of MSM squeezed light. Presented is a scheme for the generation of a single beam of light that will demonstrate sub-QNL quadrature fluctuations (-4dB) across a multitude of spatial modes simultaneously, purely as the result of one squeezing setup. In this case, the variable we wish to measure precisely is the amplitude of the field, and the conjugate variable is the phase. The specific demonstration takes the form of a homodyne detector in which the signal field of squeezed vacuum is interrogated by a local oscillator with a selectable transverse profile. Thus when squeezing is measured with a multitude of these profiles, it is evidently present across each mode interrogated.

This arrangement could be taken forward for use in quantum imaging systems or instead could be implemented in a quantum information protocol in which qubits can be stored in various transverse spatial modes of the beam and then transported and read out with reduced noise and as such greater accuracy.

My contribution to this work consists of the creation of the experimental setup from a start-up lab and the collection of all data contained herein. A paper covering the key findings of chapter 4 has been published in Physical Review A[57].

Thesis Outline

The **first** chapter describes the theoretical framework on which the notion of squeezed light is based, linking the concepts of squeezing to the multi-mode framework required. It also describes the physics behind squeezed light measurements made further on and how they demonstrate the reduction in fluctuations below the standard quantum limit.

The **second** chapter gives an introduction to nonlinear optics and explains how squeezed light can be obtained from a source of rubidium (^{85}Rb). It also categorises the effectiveness of the source used in this experiment with reference to a number of experimental parameters.

The **third** chapter is a breakdown of the experimental setup used to generate the squeezed light that forms the source of the later experiments.

The **fourth** chapter is a more detailed investigation into the 4WM process in ^{85}Rb and attempts to demonstrate that the optimum parametrisation for generating strongly correlated twin beams is rather distanced from those that generate the most efficient 4WM.

Finally, the **fifth** chapter presents the methodology and results obtained from the primary investigation into the usage of 4WM in ^{85}Rb to generate a beam of light with reduced amplitude fluctuations across multiple spatial modes. This is followed by a brief discussion of the current outlook and planned future of the experiment.

Chapter 1

Squeezing in Quantum Imaging

This thesis revolves around the ability to generate light sources with amplitude fluctuations below the QNL[1]. This chapter seeks to derive and explain how this is possible and how such light sources operate.

The classical description of the type of imaging under consideration will be defined, as well as its inherent limitations. The concept of super-resolution techniques will be introduced, techniques that attempt to overcome these limitations. This will be followed by an explanation of why the effectiveness of such techniques is limited by the amplitude fluctuations of the field. The extension will then be made to squeezed light fields and how they can lend themselves to reducing these fluctuations and thus improving the effectiveness of the super-resolution technique.

Following the imaging section, a description will be given firstly of the form of these squeezed fields, then details about how they can be detected and measured in an experimental setup. Finally some time will be spent describing what it means to say that squeezing is present across multiple spatial modes, and why this is of importance to the field of quantum imaging.

[1]The SNL is essentially the QNL of amplitude variation.

1.1 Limits of Classical Imaging

We begin by describing a classical imaging system, as shown in figure 1.1. Consider a collimated light source illuminating a compact object. The object is compact in that it is small compared to the breadth of the illuminating field. A lens of focal length f placed at a distance $s = f$ from this source will capture a portion of the light and focus it towards a point on the far side of the lens at $s' = 2f$ from the object. If a second lens, also focal length f, is placed in line at a distance $s'' = f$ from the focussed image then the light beyond this lens will form an image of the point source at a distance $4f$ from the object. Such a system is one of the simplest optical systems to describe and is known as a 'Four-f' system as $4f$ describes the distance from the object to the image. Such a system is shown in fig. 1.1.

Imperfections in the resulting image will always be present due to the finite size of the lenses. This allows for the capture of only a finite solid angle of the original field. The capture width of the system is referred to as the numerical aperture ($NA = n \sin\theta$).

Instead of an ideal replication of the object, the image will be some function of the source. The function that defines the image of a point source for a given optical system is named the point spread function (PSF). Similarly, the effect of imaging a pair of point sources is to produce a pair of spread functions and there is a limit on the minimum separation between the sources before the overlap of the imaged functions results in an inability to differentiate the sources from each other. The most famous characterisation of this limit is the Rayleigh criterion[11], which states that the two sources are just resolved when the maxima of the first spread function coincides with the principle minima of the second. Extrapolating this to the case of imaging an arbitrary object, it is clear that the effect of the PSF is to cause a reduction in sharpness between the image and the original object.

The techniques used to image with a greater level of resolution than that defined by this criterion are known as super-resolution techniques. The one under consideration here involves analytical extrapolation of the portion of the Fourier transform captured by the imaging device to reproduce additional features present in the original object. In fig. 1.1, the Fourier transform of the object is reproduced and then effectively clipped as a result of the finite numerical aperture of the system. In order for this technique to work it is of course a requirement that the Fourier transform of the object is indeed an analytical function. The super-resolution technique operates on the principle analytical functions can be extrapolated from a sample of the Fourier transform[9]. This technique has recently been shown to reduce the noise to between 45 and 89% of the Rayleigh limit depending on the degree of angular information in the object[58]. In this setup the selection of objects that can be described as analytical functions in this manner are those that are compact with respect to the illuminating field.

Figure 1.1 shows a 4f system where on the left an object is present that can be described as a sharp-edged top hat function given by

$$f_O(x) = \begin{cases} x & \text{if } -\frac{L}{2} \leq x \leq \frac{L}{2}, \\ 0 & x \leq -\frac{L}{2}, x \geq \frac{L}{2}. \end{cases} \tag{1.1}$$

The light field is incident on this object then passes through a lens, giving a field in the Fourier plane described by a sinc function

$$\tilde{F}(k) = \int_{-\infty}^{\infty} f_O(x) e^{2\pi i x k} dx \tag{1.2}$$

$$= \text{sinc}(x) = \frac{\sin(x)}{x}. \tag{1.3}$$

The NA acts to limit the transmission of higher order spatial frequencies of this

transform through the second lens, such that the transform is clipped. Thus the function at the image plane is described by

$$f_I(x) = \int_{-L/2}^{L/2} \tilde{F}(x) e^{2\pi i x k} dk. \tag{1.4}$$

This function lacks the higher frequency components of the original $f_O(x)$, which are the frequencies that allow for the sharpness of the edge of the top-hat function. The result in the image plane is a broader function with reduced sharpness.

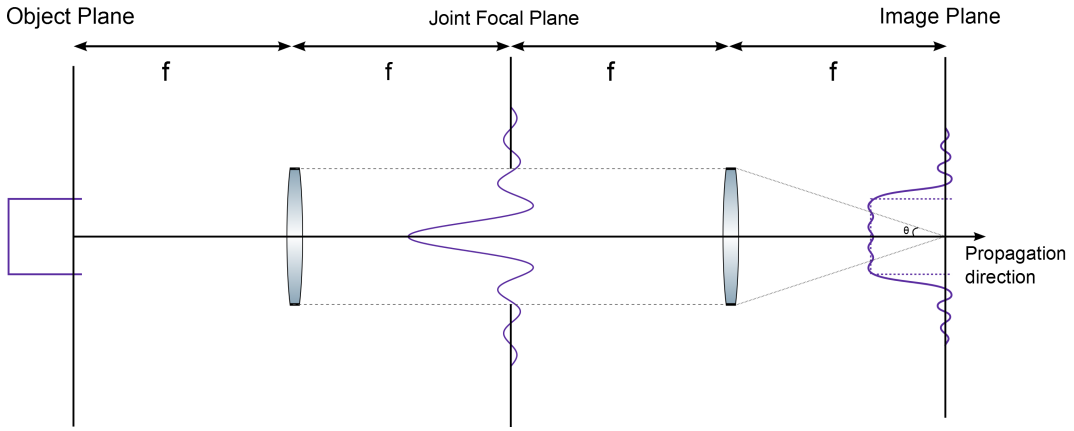

Figure 1.1: Shows a 4f imaging system consisting of a pair of lenses. The lens pair forms a numerical aperture for the system that effectively clips the Fourier transform produced by the first lens, generating reduced sharpness in the image plane. The functions show the amplitude profile across a cut-through the field at each location.

By collecting information about the complex amplitude of the field across the image plane, the Fourier analysis can be performed and reconstruction of the object to accuracy greater than that achievable in the diffraction-limited case can be achieved.

The limitations on this have been shown to rest fundamentally on the amplitude fluctuations received in the final image [9][59]. These fluctuations generate noise on the reconstructed transform and therefore on the ability to accurately re-form the object. By reducing the extent of these fluctuations it is hoped the accuracy of such techniques can be pushed further. However, as will be shown, there is a fundamental

limit to the degree of these fluctuations on any classical source that is mandated by the laws of quantum mechanics. The next section intends to show the origins of this limit and how this limitation can be overcome with specifically engineered non-classical illumination sources.

1.2 Breaking the Classical Resolution Limit

1.2.1 Coherent States and Uncertainty

Having stated that the ability of the given super-resolution technique to improve the imaging accuracy of an appropriate imaging system is limited by the amplitude noise on the measured signal, the question of how to increase the final accuracy further becomes one of whether this amplitude noise can be reduced. The following section will show that it can, and how this is achieved.

Classically, a field of arbitrary amplitude and phase can be depicted on a diagram as a phasor, a vector with length proportional to the amplitude of the field and angle with respect to the x axis corresponding to the phase. An example is shown in figure 1.2 with amplitude A and phase ϕ. In terms of the field equation this is produced by decomposing the field into components proportional to the two quadratures X and Y [60] that form the axes of the diagram such that

$$E(t) = 2\mathcal{E}_0(X\cos(\omega t) + Y\sin(\omega t)). \tag{1.5}$$

where $\mathcal{E}_0 = \sqrt{\hbar\omega/2\epsilon_0 V}$, ω is the angular frequency of the field, ϵ_0 is the permittivity of free space and V is the volume in which the field is excited.

Taken to the quantum mechanical level the field operator takes the form

$$\hat{E}(t) = 2\mathcal{E}_0(\hat{X}\cos(\omega t) + \hat{Y}\sin(\omega t)), \tag{1.6}$$

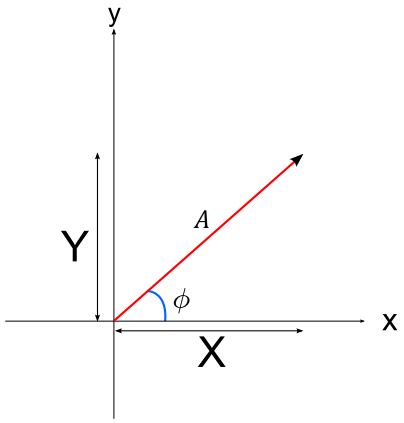

Figure 1.2: Shows a classical field depicted on a quadrature diagram with amplitude A and phase ϕ.

where the quadrature operators can now be described in terms of standard bosonic creation and annihilation operators $\hat{a}^\dagger$ and $\hat{a}$ as

$$\hat{X} = \frac{\hat{a} + \hat{a}^\dagger}{2}, \tag{1.7a}$$

$$\hat{Y} = \frac{\hat{a} - \hat{a}^\dagger}{2i}. \tag{1.7b}$$

In the harmonic oscillator picture, these operators act to raise or lower the energy of the oscillator by $\hbar\omega$. In the field picture, they introduce an additional photon to the field, such that for a number state $|n\rangle$, also known as a Fock state[61], their impact is

$$\hat{a}|n\rangle = \sqrt{n}|n-1\rangle, \tag{1.8a}$$

$$\hat{a}^\dagger|n\rangle = \sqrt{n+1}|n+1\rangle. \tag{1.8b}$$

They are also used to construct the number operator $\hat{n}$, used to determine the number

of excitations present in a number state,

$$\hat{n}|n\rangle = \hat{a}^\dagger \hat{a}|n\rangle = n|n\rangle. \tag{1.9}$$

These creation and annihilation operators follow the standard bosonic commutation relation $\left[\hat{a}, \hat{a}^\dagger\right] = \hat{a}\hat{a}^\dagger - \hat{a}^\dagger\hat{a} = 1$, leading in turn to a commutator between the quadrature operators

$$[\hat{X}, \hat{Y}] = \frac{i}{2}. \tag{1.10}$$

The existence of a commutation relation in turn gives rise to a minimum uncertainty in accordance with the Cauchy-Schwarz inequality, which states that if two variables have a commutator of the form $[\hat{A}, \hat{B}] = i\hat{C}$ then

$$\langle(\Delta\hat{A})^2\rangle\langle(\Delta\hat{B})^2\rangle \geq \frac{1}{4}|\langle\hat{C}\rangle|^2. \tag{1.11}$$

This gives the result that the variance of the two quadratures is limited according to

$$\langle(\Delta\hat{X})^2\rangle\langle(\Delta\hat{Y})^2\rangle \geq \frac{1}{16}. \tag{1.12}$$

where we define the variance of an operator $\langle(\Delta\hat{X})^2\rangle$, as

$$\langle(\Delta\hat{X})^2\rangle = \langle\hat{X}^2\rangle - \langle\hat{X}\rangle^2. \tag{1.13}$$

When the noise is minimised and spread evenly between the two quadratures such that

$$\Delta X = \Delta Y = \frac{1}{2}, \tag{1.14}$$

where

$$\Delta X = \sqrt{\langle (\Delta \hat{X})^2 \rangle}, \tag{1.15}$$

the state is a coherent state, $|\alpha\rangle$ [62]. The coherent state can be decomposed into a sum of number states

$$|\alpha\rangle = e^{-\frac{|\alpha|^2}{2}} \sum_{n=1}^{\infty} \frac{\alpha^n}{\sqrt{n!}} |n\rangle, \tag{1.16}$$

and can be shown on a phaser diagram as seen in figure 1.3. The coherent state represents the closest quantum mechanical analogue to a classical field and typically describes the output of a laser operating at the QNL. The minimum uncertainty on the position of a coherent state on a phasor diagram is equal to [63]

$$\mathcal{E}_0 = \sqrt{\frac{\hbar\omega}{2\epsilon_0 V}}. \tag{1.17}$$

Here $\mathcal{E}_0$ is the minimum area of this uncertainty region, regardless of the amplitude of the field. This uncertainty is represented in figure 1.3 as a 'fuzzball', showing explicitly the quantum mechanical limitation on the amplitude fluctuations of a classical field. The value $\mathcal{E}_0$ also forms the scalar at the front of equations 1.5 and 1.6, as it represents the energy of a single photon.

As the phase angle, ϕ, can effectively be selected to take any value with only a change in frame of the X/Y coordinate system, from here on in we will choose to work in a basis where the region of uncertainty lies centred on the X axis, with the result that uncertainty or measurement along the X axis corresponds to uncertainty in amplitude of the field, while variance in the Y axis corresponds to uncertainty in the phase of the field. As such references to the 'amplitude' or 'phase' quadrature refer also to the X and Y axis respectively.

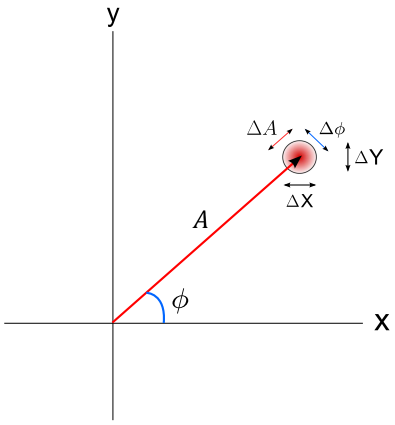

Figure 1.3: Shows a coherent state depicted on a quadrature diagram with amplitude A and phase ϕ. The region of uncertainty is the minimum allowed by quantum mechanics and has an area equal to $\mathcal{E}_0$. The width of $\Delta X/\Delta Y$ corresponds to a drop-off of 1/e of the 'fuzzball' intensity.

1.2.2 Squeezed Light

In figure 1.3, the uncertainty region is circular, corresponding to an equal degree of uncertainty in both the amplitude and the phase, and also in either the X or Y direction. An alternative to this condition is an unequal uncertainty distribution, where the variance of one quadrature is reduced at the expense of the other, e.g.

$$\langle(\Delta\hat{X})^2\rangle < \frac{1}{4}, \tag{1.18a}$$

$$\langle(\Delta\hat{Y})^2\rangle > \frac{1}{4}, \tag{1.18b}$$

or vice versa. Such states are known as squeezed states [64] [65] as on a similar phase diagram the region of uncertainty in their quadratures takes the form of an ellipse. Examples of this are also shown in figure 1.4 both for variance reduction in phase and in amplitude, though reductions of arbitrary quadrature angles are achievable. Squeezed states have long been a source of great interest in the field of quantum optics as, for certain obtainable forms of this ellipse, the result is a light field with

fluctuations in phase or amplitude below the QNL. An impressive and clear display of such states can be seen in the work by Breitenbach in 1997[66].

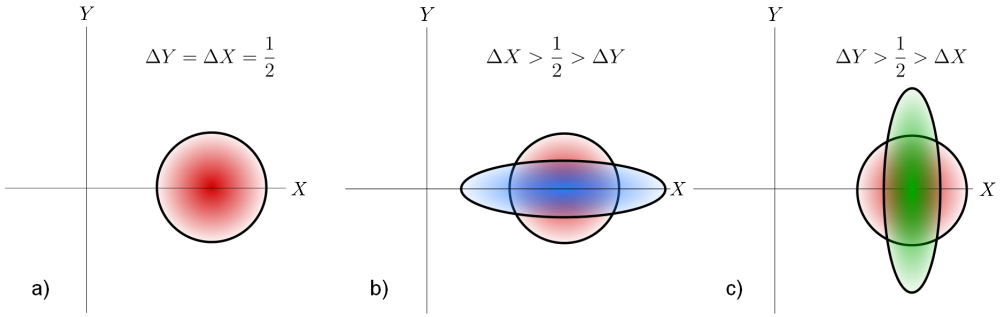

Figure 1.4: Shows a) a coherent state, b) a phase squeezed state and c) an amplitude squeezed state. Behind the squeezed states a reproduction of the coherent state is shown for comparison. The size of the uncertainties on the axis have been enlarged with respect to the distance from the origin for effect. The widths of the fuzzball are given as where the value drops to $\frac{1}{e}$ of the maximum central value.

In terms of the field, quadrature squeezed light takes the standard form with the squeezed quadrature multiplied by a factor of e^{-s} and the anti-squeezed quadrature multiplied by a factor of e^{s} where s is the 'squeeze factor'.

Squeezing is also applicable to vacuum states. A vacuum state is equivalent to a coherent state centred on the origin on a quadrature plot, where the expectation value of the amplitude is zero. But in this situation, equation 1.13 demonstrates that even when the expectation value of the field amplitude is equal to zero, the expected square of the amplitude is non-zero. The result is the vacuum state, $|0\rangle$ which has an energy corresponding to the ground-state energy of an electromagnetic field containing zero photons, as described in equation 1.17. This vacuum field can be seen in the Casimir effect/Casimir-Polder force [67]/[68] and is involved in a variety of phenomena including the Lamb shift in atoms [69] and the spontaneous emission of photons by excited electrons.

In terms of squeezing, the variance of this field along the X and Y axes can also be manipulated, and will be described in the same manner as before, i.e. as X/Y or

amplitude/phase quadratures. It should be noted that in real terms a description of the 'phase' or 'amplitude' of such a field is harder to define, though will become clearer in section 1.4.

1.3 Two-Mode Squeezed States

The experimental aim of this thesis is to produce a single squeezed light field as described in section 1.2.2. However, the emissions from the nonlinear process utilised in the experiment do not fit this description. Instead, this process produces entangled photon pairs. In this section a description of the entangled fields will be given as well as an explanation as to how these twin fields can be manipulated in order to produce the form of squeezing desired. In short this involves combining the two output fields in such a way that the correlations present between them at the start are effectively transformed into properties of the individual fields. How this is done will be explained shortly, but first, a brief description of the form of the entangled fields.

The concept of entanglement was first introduced in Einstein's seminal paper in 1935 [70] and describes a case where a pair of delocalised systems can no longer be considered using independent wave functions. Instead the non-local wave function governing both systems must be used.

To describe correlations across two delocalised modes we must first define the joint quadratures. Take two fields with angular frequency ω and quadrature depictions

$$\hat{E}_1(\mathbf{r},t) = 2\mathcal{E}_0[\hat{X}_1\cos(\omega t) + \hat{Y}_1\sin(\omega t)], \tag{1.19a}$$

$$\hat{E}_2(\mathbf{r},t) = 2\mathcal{E}_0[\hat{X}_2\cos(\omega t) + \hat{Y}_2\sin(\omega t)]. \tag{1.19b}$$

In the case of bright beams we treat the quadratures as a mean term with quantum

fluctuations, as shown in figure 1.3 with $E_X = \langle \hat{X} \rangle + \delta \hat{X}$. The joint quadratures $\hat{X}_-, \hat{X}_+, \hat{Y}_-$ and $\hat{Y}_+$ refer to combinations of the quadratures of each field where

$$\hat{X}_- = \frac{1}{\sqrt{2}}(\hat{X}_1 - \hat{X}_2), \tag{1.20a}$$

$$\hat{X}_+ = \frac{1}{\sqrt{2}}(\hat{X}_1 + \hat{X}_2), \tag{1.20b}$$

$$\hat{Y}_- = \frac{1}{\sqrt{2}}(\hat{Y}_1 - \hat{Y}_2), \tag{1.20c}$$

$$\hat{Y}_+ = \frac{1}{\sqrt{2}}(\hat{Y}_1 + \hat{Y}_2). \tag{1.20d}$$

These joint terms also share uncertainty relations,

$$[\hat{X}_\pm, \hat{Y}_\pm] = \frac{1}{2}[\hat{X}_1 \pm \hat{X}_2, \hat{Y}_1 \pm \hat{Y}_2] = \frac{1}{2}([\hat{X}_1, \hat{X}_2] + [\hat{Y}_1, \hat{Y}_2]) = \frac{i}{2}, \tag{1.21a}$$

$$[\hat{X}_\pm, \hat{Y}_\mp] = 0. \tag{1.21b}$$

The result of equation 1.21b means the two joint uncertainties described by equation 1.21a can be squeezed simultaneously.

In the experimental setup used the source of any field correlations is photon pair production from 4WM in ^{85}Rb. At the point of emission photons are simultaneously generated into two separate channels as a result of the nonlinear process. In the continuous wave regime with bright beams the resultant twin beams demonstrate entanglement as they share amplitude correlations such that even while the noise of each beam individually may be above the SNL, a balanced detection measurement (as will be described in section 1.4.1) will give a noise level below the shot noise expected for that given power/detector.

This can easily be seen in the joint quadrature picture. Due to the pair-wise nature of the photon production, an increase in the amplitude of E_1, i.e. the X_1 quadrature, will be correspondingly met with the same fluctuation in the X_2 quadrature, causing

a reduction in the variance of $\hat{X}_-$ and a corresponding increase to the variance of $\hat{Y}_-$. Similarly the process causes an amplification on the field modes, taking the noise on these modes above that of the shot noise[2] and thus causing an increase in the uncertainty of $\hat{X}_+$. Similarly the phase sum $\hat{Y}_+$ is a squeezed quantity, with a shift in the phase of one field being balanced by an opposite phase shift in the other. This also corresponds to the increase seen in the variance of the amplitude sum $\hat{X}_+$. Such cases, where squeezing is present across two spatially separated fields, are known as two mode squeezed states (TMSS).

The form of these joint quadratures is depicted in figure 1.5 showing a) the X and Y quadratures of the two emitted fields, featuring more noise than a coherent state (coherent state indicated by a dotted line) while b) shows the combinations of $\hat{X}_1$ with $\hat{X}_2$ as well as $\hat{Y}_1$ and $\hat{Y}_2$, showing the form of the correlations.

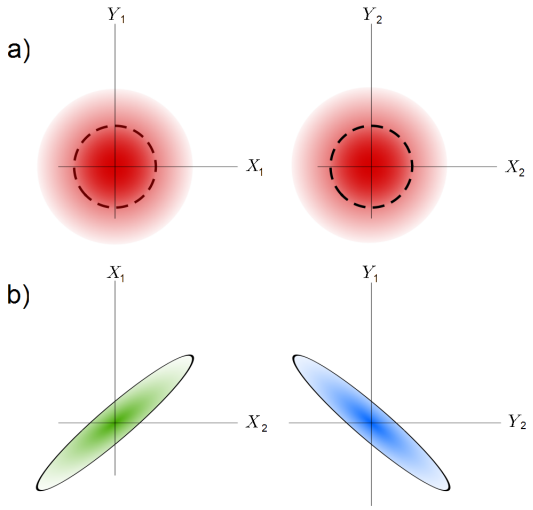

Figure 1.5: Shows a) the quadrature fluctuations across $\hat{E}_1$ and $\hat{E}_2$, each of which feature greater noise than a coherent state (coherent state noise indicated by the dashed line.) Also in b) shows the uncertainty fluctuations of the combined quadratures, indicating a reduction in $\hat{X}_-$ and $\hat{Y}_+$ as well as an increase in the uncertainty of $\hat{X}_+$ and $\hat{Y}_-$.

[2]The necessity of introducing noise when generating pair-states in this manner is described further in section 2.3.1

Such entangled/'two-mode squeezed' states will form a foundation of the present thesis, and also occur in the vacuum regime as a result of nonlinear optical processes as will be discussed in chapter 2.

1.4 Quantum Noise Measurement

In order to demonstrate squeezing, the noise on the light beam, i.e. the extent of its fluctuations, must be measured. The method of detection depends on the type of squeezing to be detected. Here we describe the two methods considered later in this thesis. The first describes the method used for quantifying amplitude correlations across a pair of twin beams, the second a method for detecting quadrature-squeezed vacuum.

Information regarding the intensity of a light field can be extracted using a photodiode. These are semiconductor devices that release an electron from the valence band into the conduction band upon detection of a photon. This photocurrent, i is proportional to the incident power of the beam and the efficiency of the process η.

$$i(t) = \frac{\eta e P(t)}{\hbar\omega}, \tag{1.22}$$

where e is the charge of an electron, P(t) is the incoming power of the beam and ω is the angular frequency of the field.

In both twin beam and vacuum state cases, in order to quantitatively analyse the noise on the electronic signal generated by the photodiodes, a spectrum analyser is used. This device analyses a signal (in this case the output from a balanced detector) in the frequency domain thus showing the noise characteristics of the signal. This can therefore be used to view the shot noise level given by an unsqueezed signal, but also any reduction in the noise below this level as a result of a squeezed light input.

1.4.1 Measuring Two-Mode Squeezing on Bright Beams

For detecting correlations across two bright beams, as seen in [71], a balanced detector is used. This consists of a pair of photodiodes and puts out a current proportional to the difference between the two generated photocurrents i_1 and i_2 such that

$$i_{out}(t) = i_1(t) - i_2(t), \tag{1.23}$$

$$= \frac{\eta_1 e P_1(t)}{\hbar\omega_1} - \frac{\eta_2 e P_2(t)}{\hbar\omega_2}. \tag{1.24}$$

If both inputs originate from the same source with equal power, and the photodiodes each have an equal level of efficiency, then the noise on the resulting current will be purely due to the quantum statistics of the beam, as any classical or technical noise on the beam will be present at both detectors and so cancelled out in the subtraction, a process known as common mode rejection.

A coherent laser beam has a Poissonian photon distribution

$$P(n) = \frac{\langle n\rangle^n e^{-\langle n\rangle}}{n!}, \tag{1.25}$$

where n is an integer, $P(n)$ is the probability of detecting n photons at a given time and $\langle n\rangle$ is the expectation value of n, equal to the variance in n, $(\Delta n)^2 = \langle n\rangle$.

However, in this thesis the fields being measured for amplitude correlations will not be coherent states. Additional classical noise may be present on these fields as a result of experimental factors such as technical noise from the laser, and as such to see noise reduction below the SNL, this excess noise will have to be removed from the detection process. This can be performed by taking a beam of intensity I_0 and impinging it onto a 50/50 beam-splitter. The result is two beams each with average intensity $I_1 = I_2 = I_0/2$ and with correlated classical noise fluctuations. Sending these onto a pair of photodiodes, both with detection efficiency η, each

detected photon will produce an electrical signal, resulting in a pair of photo-currents, i_1 and i_2, that each also feature a classically correlated distribution of electrons. In this manner the noise difference current $i_- = i_1 - i_2$ has removed all classical noise features present on the original field due to common mode rejection and the remaining noise level is due to the shot noise of the field. This shot noise is due to the fact that in the detection system, each photon passing through the beam splitter can only arrive at one detection port or the other, with an equal likelihood of each. If the detectors are placed equally far from the beam splitter ports then the noise visible on the detection is purely due to the shot noise, giving a variance proportional to the intensity

$$(\Delta I)^2 = \langle (I - \langle I \rangle)^2 \rangle. \tag{1.26}$$

A spectrum analyser is used to show the noise on the output of the balanced detector at various frequencies.

If instead twin fields featuring amplitude correlations are incident on the two detectors, this leads to increased correlations in the twin photocurrents. Correspondingly the output noise should be visibly below the shot noise for equivalent combined power. The extent of squeezing S is related to how far the measured noise $N_{sq}(i_1, i_2)$ drops below the equivalent shot noise $N_{shot}(i_1, i_2)$

$$S = \frac{N_{sq}}{N_{shot}}, \tag{1.27}$$

and is typically measured on a logarithmic scale in units of dB,

$$S_{db} = 10 \log_{10} \frac{N_{sq}}{N_{shot}}. \tag{1.28}$$

1.4.2 Measuring Quadrature-Squeezed vacuum

In order to characterise squeezed vacuum signals in which the squeezing is present across an arbitrary quadrature, a complete analysis of the field is required. The standard method of achieving this is to project the field onto a bright beam at the same frequency, designated the local oscillator (LO), on a beam-splitter. As will be shown, this process (known as homodyne detection[72]), has the result that phase-dependent vacuum quadrature fluctuations are transferred to the detectable bright field and can then be seen on a balanced detector, as before.

The LO can be described as a classical beam with quantum fluctuations, allowed to vary in phase so that now we are no longer restricting ourselves to the case where the field lies along the X axis of the phasor diagram

$$\hat{E}_{LO} = E_{LO}e^{i\phi} + \delta\hat{E}_{LO,X} + i\delta\hat{E}_{LO,Y}, \tag{1.29}$$

where the classical field $E_{LO}e^{i\phi} = \langle LO|\hat{E}_{LO}|LO\rangle$. The correspondence to equation 1.19 is that

$$\hat{E}_{LO,X} = 2\mathcal{E}_0\delta\hat{X}_{LO} \tag{1.30a}$$

$$\hat{E}_{LO,Y} = 2\mathcal{E}_0\delta\hat{Y}_{LO} \tag{1.30b}$$

The signal, as a vacuum field, can be treated purely quantum mechanically and taken to be on-axis such that

$$\hat{E}_S = \hat{E}_{S,X} + i\hat{E}_{S,Y}. \tag{1.31}$$

When combining these on a beam-splitter, the resulting fields at the output ports $\hat{E}_1$ and $\hat{E}_2$ are formed from the two input fields according to the beam-splitter equations

that form outputs

$$\hat{E}_1 = \frac{1}{\sqrt{2}}(\hat{E}_{LO} + \hat{E}_S), \tag{1.32a}$$

$$\hat{E}_2 = \frac{1}{\sqrt{2}}(\hat{E}_{LO} - \hat{E}_S). \tag{1.32b}$$

$\hat{E}_1$ and $\hat{E}_2$ can now be written in terms of their real and imaginary parts such that

$$\hat{E}_1 = \frac{1}{\sqrt{2}}((E_{LO}\cos\phi_{LO} + \delta\hat{E}_{LO,X} + \hat{E}_{S,X}) + i(E_{LO}\sin\phi_{LO} + \delta\hat{E}_{LO,Y} + \hat{E}_{S,Y})), \tag{1.33a}$$

$$\hat{E}_2 = \frac{1}{\sqrt{2}}((E_{LO}\cos\phi_{LO} + \delta\hat{E}_{LO,X} - \hat{E}_{S,X}) + i(E_{LO}\sin\phi_{LO} + \delta\hat{E}_{LO,Y} - \hat{E}_{S,Y})). \tag{1.33b}$$

Here the allowed variation of the $\cos\phi_{LO}$ term acts to project the LO field onto a selectable phase angle of the vacuum signal. If these two fields are sent onto the ports of a balanced detector, each photocurrent, i, will be proportional to $|E|^2$. The expectation values for the LO fluctuations with respect to E_{LO} are evidently 0, while for the signal the terms containing only $\hat{E}_{S,X}, \hat{E}_{S,Y}$ can be considered small under the condition that $|E_{LO}|^2 \gg |E_S|^2$ which is satisfied when the LO is a bright beam and the signal field is a vacuum field. As such, when taken to first order and neglecting all terms declared as small in comparison to E_{LO} the resulting difference current can be written as

$$i_- = i_1 - i_2 \propto \hat{E}_{S,X}(E_{LO}\cos\phi + \delta\hat{E}_{LO,X}) + \hat{E}_{S,Y}(E_{LO}\sin\phi + \delta\hat{E}_{LO,Y}), \tag{1.34}$$

$$= E_{LO}(\hat{E}_{S,X}\cos\phi + \hat{E}_{S,Y}\sin\phi) + \delta\hat{E}_{LO,X}\hat{E}_{S,X} + \delta\hat{E}_{LO,Y}\hat{E}_{S,Y}, \tag{1.35}$$

where the terms featuring $\delta\hat{E}_{LO}$ can be neglected, giving a final form for the output

current from the balanced detector

$$i_- \propto E_{LO}(\cos\phi\hat{E}_{S,X} + \sin\phi\hat{E}_{S,Y}). \tag{1.36}$$

This photocurrent is now proportional to the amplitude of the LO while totally removing the effect of any noise it may have had, meanwhile the signal field still has a large influence, however small its original amplitude. This is especially clear when we view the noise of the current output, which can be shown on a spectrum analyser to view the variance

$$(\Delta i_-)^2 \propto E_{LO}^2(\cos^2\phi\langle(\Delta\hat{E}_{S,X})^2\rangle + \sin^2\phi\langle(\Delta\hat{E}_{S,Y})^2\rangle), \tag{1.37}$$

with the result that the noise shown on the spectrum analyser is the noise on a selected quadrature of the vacuum signal at the homodyne input. The specific quadrature angle being viewed is defined by ϕ, the relative phase of the signal field and the LO.

For example, a relative phase of $\phi = 0, \pm n\pi$, where n is an integer, would show a result proportional to the variance of the X quadrature of the signal, $\Delta E_{S,X}$. Conversely a phase difference of $\phi = \frac{\pm(2n+1)\pi}{2}$ would effectively measure the noise on the Y quadrature, $\Delta E_{S,Y}$. In this manner, by scanning the relative phase of the two fields by, for example, using a piezo-electric transducer (piezo) on a mirror to scan the phase of the LO, a complete picture of the quadrature noise of the signal field can be obtained, thus showing any squeezing features. For a squeezed state, the measured noise would drop below the SNL at certain values of ϕ. The SNL itself can be seen for comparison by blocking the signal field. This has the result that the split LO mixes only with an un-squeezed vacuum state and the spectrum analyser displays the shot noise relating to the incident power of the LO.

Another more qualitative way of looking at homodyne detection, and one that

will serve as an aid in future chapters, is to think of the process from the point of view of measuring the correlation of sidebands. This is displayed in figure 1.6. As the spectrum analyser operates in the frequency domain, it in fact reads out the noise values corresponding to sidebands on the electrical signal from the balanced detector over a selectable frequency range. As the main bright light source comes from the LO and is subtracted, this corresponds to looking at the beat signal present in the field between frequencies to either side of the LO, making any correlations on these sidebands visible.

Take a frequency axis as shown in figure 1.6 and display classically all present fields at each frequency as lines extending from the centre by a length proportional to their amplitude and each rotating around the axis at a rate proportional to their position along it. This rotation corresponds to the rotating phase of each field. The detector samples the bright central LO combined with the fluctuations to either side, causing an overall variation in the length of the vector sum of the measured fields. Taking the LO as centred and stationary, the sidebands can be depicted as a term rotating in the clockwise direction at a frequency $f_{LO+\omega_{sq}}$ and a term rotating counter-clockwise at a frequency $f_{LO-\omega_{sq}}$. Here ω_{sq} is the frequency viewed on the spectrum analyser (typically in the MHz region) and is assumed to be very small with respect to f_{LO}. The amplitude variation at $\omega_{sq} = 0$ (DC) cannot be viewed as it in effect requires an integral over an infinite amount of time.

Depending on the relative phase of the LO and the twin oscillating terms, the effect on the vector sum will be drastically altered. The two extreme cases are either that the sidebands are aligned when in line with the LO, (case a) in figure 1.6), or anti-aligned (case b)). In the first case, when the amplitude terms are summed, the correlations of the sidebands cause the total sum to vary greatly. Meanwhile the phase variations will be reduced due to the counter-rotation of the bands. Conversely, in case b), the correlated amplitude fluctuations will cancel out, leaving a lower level

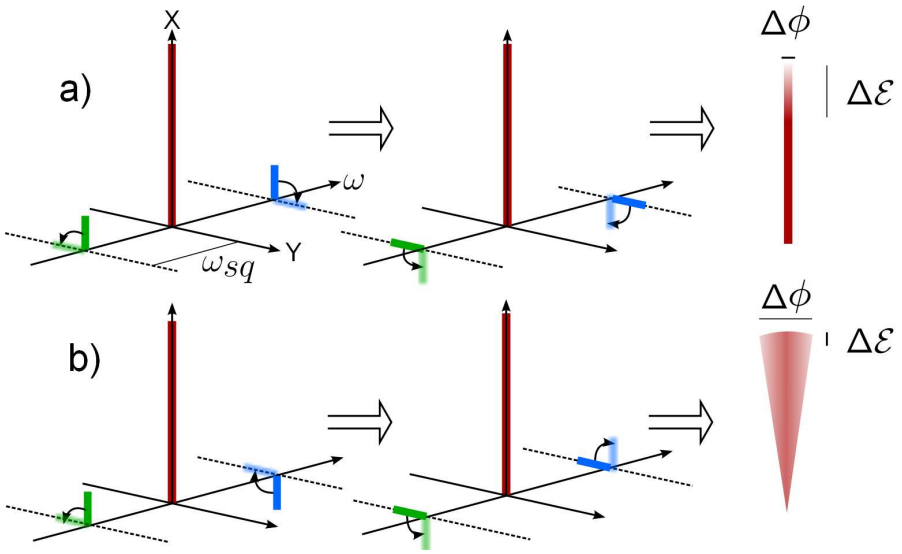

Figure 1.6: Shows a) a combination of signals in the sideband picture of homodyne detection that leads to large amplitude fluctuations and low phase fluctuations, b)the LO has been rotated by $\pi/2$ leading to the reverse situation in which phase fluctuations are greater while amplitude fluctuations are reduced.

of variation in the amplitude of the vector sum, and a lower reading on the spectrum analyser. Also in case b), the phase variance will be increased in a manner analogous to the amplitude variation in the previous picture.

This approach also reveals that in essence all squeezed states can be described in terms of a TMSS, with the case of squeezing on a single field still referring to correlations between two modes, here the paired sidebands at some distance from the central field.

1.4.3 Relationship between Direct and homodyne Detection

Noise measurement of a light field detected directly via a photodiode can be seen as analogous to a special kind of homodyne detection in which the LO and the signal are carried by the same field. If the field is again decomposed into a bright signal

with quantum fluctuations as in equation 1.29, then the intensity is given by

$$|E|^2 = E^*E = \langle (E + \delta E_X + i\delta E_Y)(E^* + \delta E_X - i\delta E_Y)\rangle, \tag{1.38}$$

$$\simeq |E|^2 + 2|E|\delta E_X, \tag{1.39}$$

when assuming $E \gg \delta E_X, \delta E_Y$. This gives the result that the intensity is proportional to the square of the amplitude and only includes the effect of the E_X quadrature. In this manner a photodiode is effectively a homodyne detector only capable of detecting a single ellipse angle/quadrature, due to the inability to change the relative phase between the bright part and the fluctuations as they form a single field.

1.5 Multi-Spatial-Mode Squeezing

So far throughout this document the propagating EM field has only been considered in terms of its varying amplitude along the axis of propagation, taken as the z axis. It is now necessary to introduce the transverse profile of the beam, corresponding to the x and y axes.

Looking at the field intensity across 3 dimensions

$$E = U(x, y, z)e^{-ikz}, \tag{1.40}$$

then assuming the varying intensity, U, changes much less along the propagation axis than the transverse axis, the paraxial wave equation can be obtained [73] that states

$$(\partial_x^2 + \partial_y^2)U - 2ik\partial_z U = 0. \tag{1.41}$$

This equation has an infinite number of solutions, giving an infinite potential number of forms for the transverse profile of the beam. The most fundamental of these is

that of the Gaussian beam with an intensity profile given by

$$U(x,z) = \sqrt{\frac{2}{\pi}}\frac{1}{w(z)}\exp(i\psi(z))\exp\left(\frac{-ikx^2}{2R_c(z)} - \frac{x^2}{w^2(z)}\right). \tag{1.42}$$

This gives a circular profile with an intensity varying in the radial direction in accordance with

$$I(r) = \frac{2P}{\pi w^2(z)} e^{\frac{-2r^2}{w^2(z)}}, \tag{1.43}$$

where P is the total input power of the beam and w is the spot size, given by the radius of the beam at which the intensity has dropped to $1/e^2$ its maximum value of $I(0)$. This intensity profile corresponds to a Gaussian distribution, hence the denotation of the beam as 'Gaussian'.

In the above equations $w(z)$ is the spot size at position z,

$$w(z) = w_0\sqrt{1 + \frac{z - z_0}{z_R}}, \tag{1.44}$$

with w_0 equalling the value of the beam waist, the minimum size of the spot. Also above, $\psi(z)$ is the Gouy phase, which corresponds to a longitudinal phase lag when compared to plane waves, seen more prevalently on higher order spatial modes,

$$\psi(z) = \arctan\frac{z}{z_R}, \tag{1.45}$$

and R_c is the radius of curvature of the spherical wavefront,

$$R_C(z) = z - z_0 + \frac{z_R}{z - z_0}. \tag{1.46}$$

The variance along the y axis follows the same form as equation 1.42 with $x \to y$.

The value z_R corresponds to the Rayleigh range, a factor that can be used to

characterise the value of z into the so-called 'near-field' ($z < z_R$) and 'far-field' ($z > z_R$) regimes. z_R is defined as

$$z_R = \frac{\pi w_0^2}{\lambda}, \tag{1.47}$$

and λ is the wavelength of the field. The near-field can be used to gain information about the spatial distribution of the field around the waist, while the same distribution in the far-field contains information about the momentum and wave-vectors of the field at the waist, governing its divergence.

There are an infinite number of higher order solutions to equation 1.41 classified by a pair of indices corresponding to the order of the x and y profile

$$U_{nm}(x, y, z) = U_n(x, z)U_m(y, z), \tag{1.48}$$

so the Gaussian beam would be designated TEM_{00} where TEM is an acronym for Transverse Electromagnetic Mode. The two most familiar complete sets of orthonormal solutions are the Hermite-Gauss (HG) modes and the Laguerre-Gauss (LG) modes.

HG modes are obtained by multiplying the Gaussian form by the Hermite polynomials and are described algebraically by

$$U_n(x, z) = \left(\frac{2}{\pi}\right)^{1/4} \left(\frac{\exp(i(2n+1)\psi(z))}{2^n n! w(z)}\right)^{1/2} H_n\left(\frac{\sqrt{2}x}{w(z)}\right) \exp\left(\frac{-ikx^2}{2R_c(z)} - \frac{x^2}{w^2(z)}\right). \tag{1.49}$$

Linear combinations of these higher order modes can be used to generate arbitrary transverse beam profiles. Again, the y profiles can be formed similarly with $n \to m, x \to y$. These HG modes describe intensity profiles pictured in figure 1.7 showing the effect of the first few orders of HG_{nm} in the x, y plane. These correspond to a

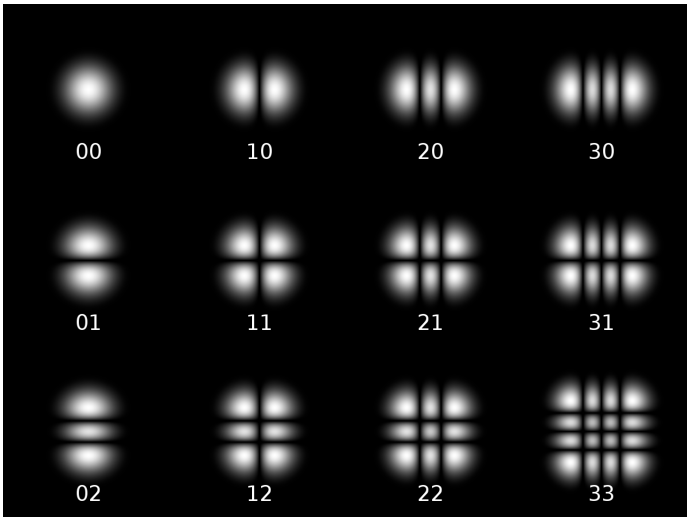

Figure 1.7: Shows a selection of HG modes of increasing order in both indices, up to HG_{33}.

breakdown of the beam profile into different regions separated by lines drawn along cartesian axes.

Conversely the LG modes are obtained by combining the Gaussian form with the Laguerre polynomials, and break down the field along cylindrical axes.

The effect of these higher order modes can be seen in regular single-spatial-mode squeezing experiments. For example, when a beam is created with reduced intensity fluctuations in a cavity coupled to the TEM_{00} mode the effect is to produce a reduction in the peak intensity variance. However, vacuum fluctuations in the higher order modes still cause fluctuations in the intensity profile. Figure 1.8 demonstrates how the TEM_{01} vacuum mode causes oscillations in the position of the central intensity peak as the maximum amplitude shifts around the centre, while the effect of the TEM_{02} mode causes a breathing motion, shifting the intensity from the centre to the outskirts.

In the phase picture these fluctuations also have an effect. On the TEM_{01} mode if the local position uncertainty is reduced, the transverse momentum uncertainty is

increased, corresponding to an uncertainty in the direction of the beam and the far-field position. In the TEM_{02} mode the uncertainty reduction corresponds to a more precise focal size and beam waist in the near field, with the conjugate uncertainty being in the overall divergence of the field, the variance of which increases. In reality all of these and a near infinite number of higher order vacuum modes all act on the squeezed beam causing variations in the transverse intensity profile at the quantum level. It is these fluctuations that we seek to reduce in the presented setup for quantum imaging.

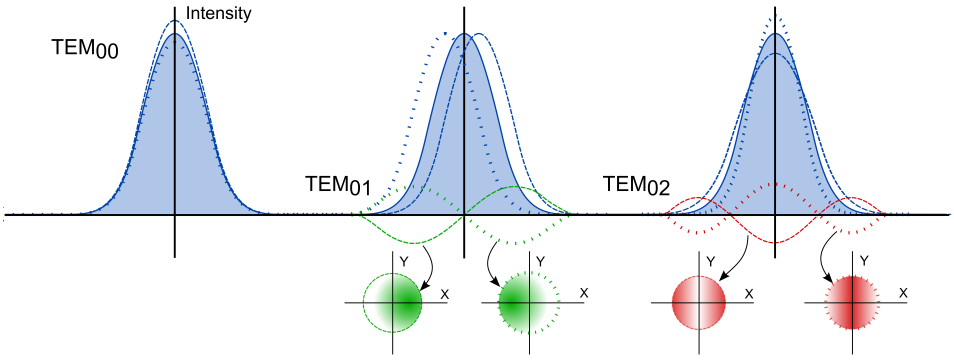

Figure 1.8: Shows the effect of vacuum fluctuations on the intensity profile of a Gaussian beam. Upper line shows an intensity distribution cross section across the profile, second line shows the intensity profile of the extremes of the vacuum fluctuations on higher order modes. The TEM_{00} mode is occupied by the bright field and features fluctuations across the entire intensity profile. Fluctuations on the TEM_{01} mode act to shift the distribution of the amplitude from left to right, causing noise on the central position of the Gaussian maximum. The TEM_{02} fluctuations act to shift intensity between the centre and the edge, causing a breathing effect on the profile. In practise all these and higher orders act simultaneously causing an overall roughing effect on the Gaussian intensity profile.

Methods usually used in the generation of squeezed light include 4WM in vapours or fibres, or photon pair production in crystals which all generally require the use of a cavity in order to produce high enough field strengths to generate the nonlinear response[3]. For these to be at their most effective, the laser must be locked into the

[3]more on nonlinear responses in section 2.1.

cavity. while this may serve to introduce squeezing, the squeezing is only detected when analysing the mode of the field that corresponds to that locked to the cavity. Selecting some arbitrary mode (or equivalently any subsection of the transverse profile of the field) will result in a swift reduction in the measured squeezing. The effect is similar to that of introducing a lossy medium into the beam, a process discussed further in section 5.3.2. In the case of multi-spatial mode (MSM) squeezed light the effects of loss are the same, while the negative impact of a modal mismatch are greatly reduced. The method described here generates gain of around $2-5$ after a single pass, meaning that no cavity is needed to see appreciable quantum effects. As such there is no preferred transverse mode for the squeezing to operate and in fact squeezing is generated across around a few hundred spatial modes[4] simultaneously.

[4]Further discussion on the number of modes affected can be found in section 5.2.

Chapter 2

Four-Wave Mixing as a Source of Two-Mode Squeezed Light

In this thesis the entangled fields are generated via a nonlinear optical process stimulated in a heated cell of ^{85}Rb. This chapter will detail the process that generates the fields, along with a discussion on the impact of certain experimental parameters on the effectiveness of the process.

2.1 A Brief Introduction to Nonlinear Optics

The polarisation of a material refers to the collective dipole moment per unit volume and how it varies in the presence of an oscillating electromagnetic (EM) field. Typically this response is purely linear and takes the form [60]

$$P(t) = \epsilon_0 \chi^{(1)} E(t), \tag{2.1}$$

where ϵ_0 is the relative permittivity of free space, $\chi^{(1)}$ is the linear susceptibility of the medium and E is the field strength of the applied EM field

$$E(t) = \mathcal{E}\sin(\omega t). \tag{2.2}$$

The polarisation serves as a driving source term in the wave equation governing the behaviour of electromagnetic fields

$$\nabla^2 E - \frac{1}{c^2}\frac{\partial^2}{\partial t^2}E = \frac{1}{\epsilon_0 c^2}\frac{\partial^2 P}{\partial t^2}. \tag{2.3}$$

However in certain materials, in the presence of powerful enough fields, the higher orders of the response of the polarisation to the applied field become relevant. When broken into a power series the polarisation behaviour of such a non-linear medium can be described as [74]

$$P(t) = P^{(1)} + P^{(2)} + P^{(3)} + \ldots = \epsilon_0[\chi^{(1)}E(t) + \chi^{(2)}E^2(t) + \chi^{(3)}E^3(t) + \ldots], \tag{2.4}$$

where $P^{(n)}$ refers to the n-th order of the polarisation and $\chi^{(n)}$ is the n-th order nonlinear optical susceptibility of the medium. If these higher order terms become large enough, the result is the generation of additional frequency components of the field, equating to the presence of supplementary monochromatic fields in addition to the one applied.

For example, in the case of a medium with strong $\chi^{(2)}$ nonlinearity driven by a single strong field E the second order polarisation component $P^{(2)}$ becomes

$$\begin{aligned} P^{(2)} &= \epsilon_0\chi^{(2)}E^2(t), \\ &= \epsilon_0\chi^{(2)}\mathcal{E}^2\sin^2(\omega t), \\ &= \frac{\epsilon_0\chi^{(2)}\mathcal{E}^2}{2}(1-\cos(2\omega t)). \end{aligned} \tag{2.5}$$

This clearly acts to generate a field oscillating at frequency 2ω in addition to the applied field of ω, which still acts to drive the first order of the polarisation response. The study of this process and many more, all based around combining different applied frequencies via nonlinear media, is known as nonlinear optics.

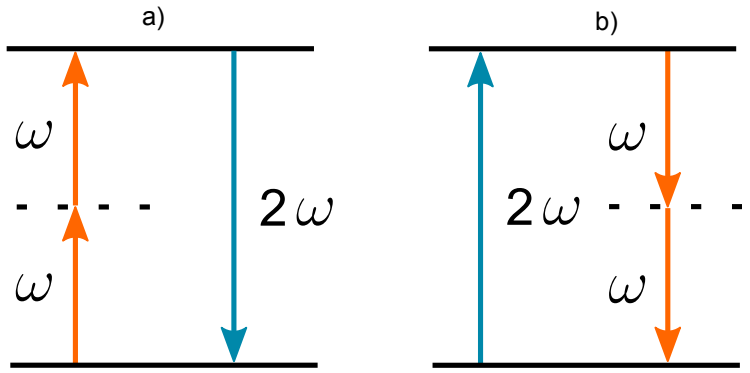

Figure 2.1: Shows a) the process of frequency doubling, in which two photons at frequency ω are absorbed and a single photon at frequency 2ω is emitted, and b) second harmonic generation, a form of parametric down conversion (PDC), which is essentially the reverse of this process. N.B. in PDC the pair of emitted photons need not be of the same frequency, it is only required they sum to 2ω.

By combining multiple input frequencies, an increasing range of combinations and couplings become available depending on the nature of the nonlinear medium. Processes are categorised according to the respective order of the nonlinearity they include, for example frequency doubling[75] or parametric down conversion[76] are two cases of 'second order' or '$\chi^{(2)}$' processes. These involve the mixing of two fields to produce a third at some sum/difference frequency, as shown in figure 2.1. Specifically, frequency doubling involves the absorption of two photons at frequency ω and the emission of a single photon at frequency 2ω and is used to generate light beams at frequencies that would otherwise be difficult to engineer. Parametric down conversion is instead the absorption of a photon with frequency ω and the emission of a pair of photons at frequencies ω_a, ω_b such that $\omega_a + \omega_b = 2\omega$ and has long been a primary source of photon pair-production. In each case clearly three fields are

involved. $\chi^{(3)}$ processes involve the mixing of four light fields and generally come under the umbrella term of four-wave mixing (4WM) for that reason. One 4WM process in particular forms the focus of this chapter.

2.2 Four-Wave Mixing in ^{85}Rb

^{85}Rb vapour is a $\chi^{(3)}$ medium, meaning the lowest order of nonlinear effects achievable involve the third order susceptibility. This is due to the inversion symmetry of the medium negating any possible $\chi^{(2)}$ effects as, in a system with inversion symmetry

$$\begin{aligned} -P(t) &= \epsilon_0 \chi^{(2)} [-E(t)]^2, \\ &= \epsilon_0 \chi^{(2)} [E(t)]^2, \\ &= P(t), \end{aligned} \tag{2.6}$$

which is only possible for $\chi^{(2)} = 0$. Similarly all other even order susceptibility terms also vanish for similar materials.

The D1 line in ^{85}Rb is shown in figure 2.2, modelled as a four-level system with a two hyperfine ground state levels and two hyperfine excited levels. In general the hyperfine structure of the excited state is not considered here, and it is treated as a single level.

Whilst squeezing has been obtained from both ^{85}Rb and ^{87}Rb[77], we will only consider the case of ^{85}Rb. As shown in fig. 2.3 the process involves a closed parametric double-lambda transition. Here the term parametric indicates that the final state is identical to the starting state, and the term double-lambda comes from the shape it traces out.

The transition is between the pair of labelled hyperfine ground states. A pump photon, frequency ω_0, is absorbed and causes a transition from the $^5S_{\frac{1}{2}}$ F = 3 state to the $^5S_{\frac{1}{2}}$ F = 2 state via the $^5P_{\frac{1}{2}}$ state. The F= 3 state is taken as the starting

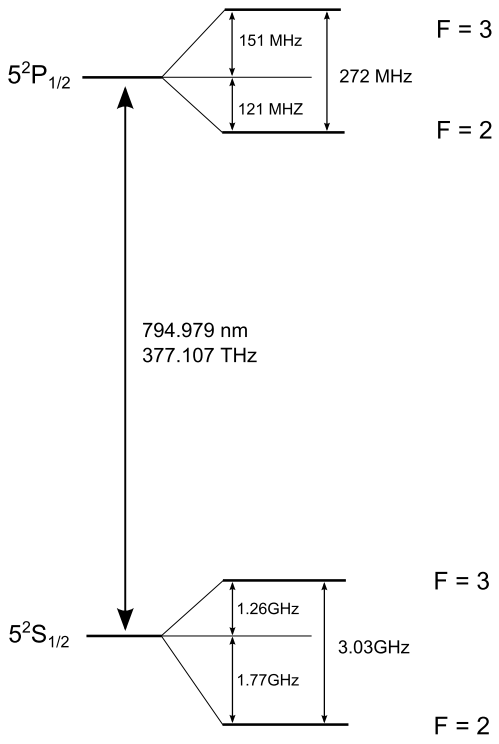

Figure 2.2: Shows the D1 line on ^{85}Rb, including energy spacings between both pairs of hyperfine levels and of the optical transition between the ground and excited state.

point of the transition as the transition coupling F= 2 to the excited state is closer to the resonance, resulting in optical pumping of the medium into the F= 3 state. The emitted photon, designated the conjugate, with frequency ω_c, is detuned from the pump by around 3 GHz, with the precise detuning related to the two-photon detuning δ. The second lambda transition is the reverse, resulting from another absorption of a photon at the pump frequency and the emission of a photon, designated the probe, at frequency ω_p such that $2\omega_0 = \omega_p + \omega_c$. The detuning from the P level for the more resonant pump transition is designated the single-photon detuning Δ_1 and is dependent on the precise frequency of the pump. The detuning of the second pump photon, Δ_2 is defined as $\Delta_2 = \Delta_1 + \omega_{HF}$ where ω_{HF} is the hyperfine splitting between the two F= 2, F= 3 ground states, $\omega_{HF} = 3036$ MHz [78].

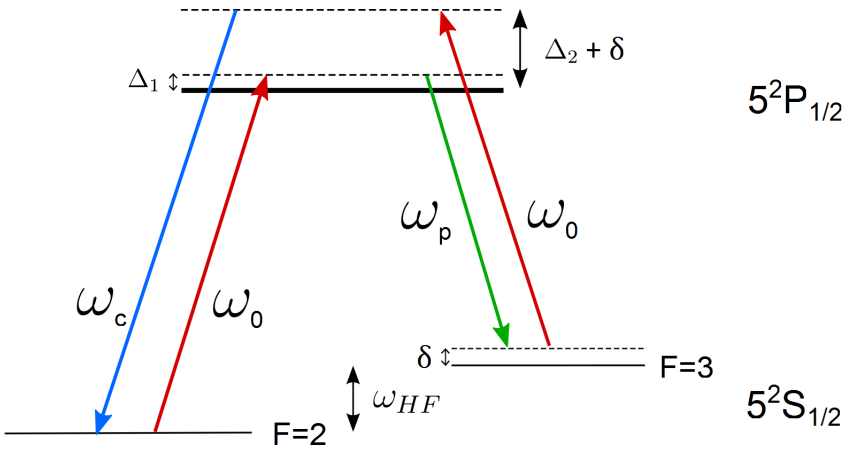

Figure 2.3: Shows the closed double Λ transition that forms the basis of the 4WM. Two pump photons (frequency ω_0) are absorbed while a probe photon (ω_p)and a conjugate photon (ω_c) are emitted. Δ_1 is the single photon detuning of the pump from the $^5S_{\frac{1}{2}}$ F = 2 $\rightarrow ^5P_{\frac{1}{2}}$ transition, δ is the two photon detuning of the probe from the $^5P_{\frac{1}{2}}$ $\rightarrow ^5S_{\frac{1}{2}}$ F = 3 transition. The system is closed such that $\omega_{HF} + \delta = \omega_0 - \omega_p = \omega_c - \omega_0$

The result of this is that when the vapour is injected with a bright pump beam at ω_0, pairs of photons are emitted at frequencies ω_p and ω_c in the forward direction with an angle relative to the pump of $\theta = 0 - 1^\circ$ to either side, as shown in figure

2.4. These emissions form the two-mode squeezed vacuum.

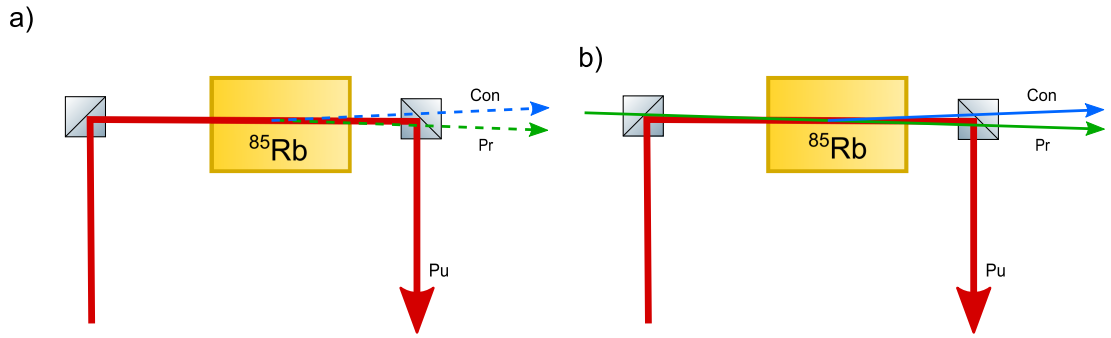

Figure 2.4: Shows a) how a cell of ^{85}Rb, when pumped, emits photon pairs in the forward direction at opposite directions to the pump. Note that in reality photon pairs are emitted in such a way within a cone-shaped region (spread extending to around 1° from the pump axis), but always in pairs and always in the forward direction. Also shows b) how the application of a seed beam at the pump frequency stimulates the process leading to the emission of twin beams designated the probe and conjugate. In this case the beams are bright and only visible in the specified direction.

If seeded with a weak input beam at frequency ω_p in addition to the bright ω_0 field, a bright conjugate field ω_c is produced such that the following phase-matching condition is satisfied

$$\Delta\mathbf{k} = 2\mathbf{k}_0 - \mathbf{k}_p - \mathbf{k}_c = 0, \tag{2.7}$$

where $\mathbf{k}_0$, $\mathbf{k}_p$ and $\mathbf{k}_c$ are the wave vectors of the pump, probe and conjugate fields respectively within the medium, the input probe experiences amplification and a secondary conjugate beam at frequency ω_c is also generated. This is shown in part b) of figure 2.4. As a result of the pairwise photon generation of these beams, they are entangled in the manner described in section 1.3 and feature highly correlated amplitude fluctuations.

This process of 4WM in Rb vapour was first observed experimentally in [51] to show, when seeded, a high level of squeezing (−3.5 dB, −8.1 dB when corrected for

losses) observable in the amplitude correlations on the bright emitted beams. The high level of nonlinear coupling between the fields means the achievable gain on a single pass is relatively high (around 3-5 in a typical squeezing arrangement). As such desirable levels of squeezing are obtainable[1] in the absence of a cavity.

This setup has been shown to generate correlated vacuum TMSS that demonstrate MSM entanglement[53]. The remainder of this chapter will detail some specific aspects of the generated twin states and the practice of maximising the effective squeezing measurable on the output fields.

2.3 A More Detailed Derivation

While the above serves as a simple introduction, a more rigorous analysis of the interactions involved will serve to provide more context for future chapters in which some of the finer details will become more relevant.

For a 4WM process described by the system in section 2.2 in which two photons of frequency ω_0 are absorbed and two emitted at $\omega_p, \omega_c = 2\omega_0 - \omega_p$, the third order polarisation is equal to[74]

$$P^{(3)}(t) = \sum_n P(\omega_n) e^{i\omega_n t}, \tag{2.8}$$

$$\tag{2.9}$$

where $n = 0, p, c$ corresponding to the pump, probe and conjugate fields respectively, giving

$$P(\omega_c = \omega_0 + \omega_0 - \omega_p) = 6\chi^{(3)}(\omega_n = \omega_0 + \omega_0 - \omega_p) E_0 E_0 E_p^*, \tag{2.10}$$

and other permutations.

[1] See section 2.3.1 for the link between gain seen and possible squeezing.

To now describe how this polarisation affects the behaviour of the fields in the medium, it is necessary to solve the wave equation 2.3 for the total field

$$E(t) = \sum_n E(\omega_n) e^{i\omega_n t}. \tag{2.11}$$

The form of solution used in this thesis differs from that obtained from the standard method presented in textbooks such as [74], however both will be discussed for comparison and completeness.

Typically the solution is found by first taking the polarisation and splitting it into a linear and nonlinear part

$$P(t) = P^{(1)} + P^{(NL)}, \tag{2.12}$$

then using the fact that the wave equation 2.3 can be reformed to depend only on the nonlinear part. To do this, the relative permittivity $\epsilon^{(1)} = (1 + \chi^{(1)}) = n^2$ (where n is the refractive index of the medium) is brought onto the left hand side (using equation 2.4)

$$\nabla^2 E - \frac{\epsilon^{(1)}}{c^2} \frac{\partial^2}{\partial t^2} E = \frac{1}{\epsilon_0 c^2} \frac{\partial^2 P^{(NL)}}{\partial t^2}. \tag{2.13}$$

The solution to equation 2.13, under the slowly varying envelope approximation (that assumes higher orders of the differentials to be negligible with respect to first order terms), takes the form for a slowly varying field amplitude A_n ($E_n = A_n e^{i(\omega_n t - k_n z)}$) and a frequency ω_n

$$\frac{d}{dz} A_n = \frac{i\omega_n}{2\epsilon_0 n_n c} P(\omega_n) e^{-ik_n z}, \tag{2.14}$$

where it should be mentioned explicitly that k_n refers to the k vector of the field *in*

the medium. However, as mentioned, this formalism is not appropriate here.

Instead, in this scenario, the two absorbed photons originate from a single strong pump field which is taken to be considerably stronger than either E_p, E_c. As a result, in this treatment [79] we neglect all terms of the form described in equation 2.10 that do not include the pump field twice. In addition, we include the pump at all orders of the susceptibility. Because of this its linear portion can no longer be treated separately and in fact the pump should be included at all orders of the polarisability.

For this reason we can no longer extricate the linear part from the wave equation and rely on a single static term for the refractive index. Instead the full polarisation for a double-lambda system as described in figure 2.3 is [80]

$$P(\omega_p) = \epsilon_0 \chi_p^{(D)}(\omega_p)\mathcal{E}_p e^{i\mathbf{k}_p.\mathbf{r}} + \epsilon_0 \chi_p^{(C)}(\omega_p)\mathcal{E}_c^* e^{i(2\mathbf{k}_0 - \mathbf{k}_c).\mathbf{r}}, \tag{2.15a}$$

$$P(\omega_c) = \epsilon_0 \chi_c^{(D)}(\omega_c)\mathcal{E}_c e^{i\mathbf{k}_c.\mathbf{r}} + \epsilon_0 \chi_c^{(C)}(\omega_c)\mathcal{E}_p^* e^{i(2\mathbf{k}_0 - \mathbf{k}_p).\mathbf{r}}, \tag{2.15b}$$

where $\chi_{p,c}$, $\mathcal{E}_{p,c}$, $\omega_{p,c}$ and $k_{p,c}$ are the overall susceptibility, the field amplitude, frequency and wave vector *in vacuum* for the probe and conjugate frequencies respectively. A more complete derivation of the form of the polarisation in terms of the relevant susceptibilities is in appendix A, and the form of the χs is given in equations 4.2a through 4.2d.

The term $\chi^{(D)}$ here refers to a 'direct' term that is the effective linear susceptibility for the respective frequency, and $\chi^{(C)}$ is a 'cross' term in that it is the susceptibility governing the cross-coupling 4WM process. In characterising the terms $\chi^{(D)}$ and $\chi^{(C)}$ in terms of their linearity, they are in fact both nonlinear in terms of their dependence on the pump field (now taken to all orders) yet linear when the presence of the pump is treated as a constant. This is valid under the assumption that the strength of the pump is such that depletion due to the process is negligible across the medium, as is the case in this setup.

The propagation of the slowly varying envelopes of the fields inside the medium can be expressed in terms of the polarisation as

$$\frac{\partial \mathcal{E}_p}{\partial z} = \frac{ik_p}{2\epsilon_0} P(\omega_p) e^{-i\mathbf{k}_p.\mathbf{r}}, \tag{2.16a}$$

$$\frac{\partial \mathcal{E}_c}{\partial z} = \frac{ik_c}{2\epsilon_0} P(\omega_c) e^{-i\mathbf{k}_c.\mathbf{r}}. \tag{2.16b}$$

By combining equations 2.15a and 2.15b with 2.16a and 2.16b the description of the propagation can be adjusted to

$$\frac{\partial \mathcal{E}_p}{\partial z} = \frac{ik_p}{2}(\chi_p^{(D)}(\omega_p)\mathcal{E}_p + \chi_p^{(C)}(\omega_p)\mathcal{E}_c^* e^{i\Delta k_z z}), \tag{2.17a}$$

$$\frac{\partial \mathcal{E}_c}{\partial z} = \frac{ik_c}{2}(\chi_c^{(D)}(\omega_c)\mathcal{E}_c + \chi_c^{(C)}(\omega_c)\mathcal{E}_p^* e^{i\Delta k_z z}). \tag{2.17b}$$

Here now $\Delta k_z = (2\mathbf{k}_0 - \mathbf{k}_p - \mathbf{k}_c)\hat{z}$ is the z-axis projection of the geometric phase mismatch, $\Delta\mathbf{k}$. The form of these χs will be discussed further in chapter 4.

2.3.1 Amplification and Squeezing

Now these descriptions have been formed for the propagation of the fields, it remains to be shown firstly that this form of propagation will result in gain and secondly that that in turn will generate TMSS correlations on the output fields. In order to see how these equations result in a gain on the probe and conjugate fields, we will first consider the situation of ideal 4WM, where there is no absorption in the material and only the gain process occurs. Next the effect of this gain will be linked to the generation of a TMSS at the output modes of the medium and finally the effects of loss will also be introduced.

Ideal Four Wave Mixing

In describing ideal 4WM, we set up the case in which the direct susceptibility terms $\chi_p^{(D)}, \chi_c^{(D)} = 0$, meaning zero absorption of the generated light fields occurs. Also we consider an undepleted pump field with no z dependence in the medium. Finally if the phase matching term is absorbed into the fields such that $\mathcal{E}' = \mathcal{E}e^{i\Delta k_z z}$, then the propagation equations can be rewritten

$$\frac{\partial \mathcal{E}'_p}{\partial z} = i\eta_p \mathcal{E}'^*_c, \tag{2.18a}$$

$$\frac{\partial \mathcal{E}'_c}{\partial z} = i\eta_c \mathcal{E}'^*_p, \tag{2.18b}$$

where

$$\eta_p = \frac{k_p}{2}\chi_{pc}(\omega_p), \tag{2.19}$$

$$\eta_c = \frac{k_c}{2}\chi_{cp}. \tag{2.20}$$

The solutions for these give the results

$$\mathcal{E}'_p(z) = \cosh(|\eta_p|z)\mathcal{E}'^*_p(0) + i\frac{\eta_p}{|\eta_p|}\sinh(|\eta_p|z)\mathcal{E}'^*_c(0), \tag{2.21a}$$

$$\mathcal{E}'_c(z) = -i\frac{\eta_c}{|\eta_p|}\sinh(|\eta_p|z)\mathcal{E}'_p(0) + \cosh(|\eta_p|z)\mathcal{E}'^*_c(0), \tag{2.21b}$$

Next we insert the experimental starting conditions. Specifically the case that we inject a seed field $\mathcal{E}'_s$ at the probe frequency while the input conjugate mode is vacuum. As such $\mathcal{E}'_p(0) = \mathcal{E}'_s$ and $\mathcal{E}'_c(0) = 0$. After travelling a distance L in the

medium the fields at the output can be described as

$$\mathcal{E}'_p(L) = \mathcal{E}'^*_s \cosh(|\eta_p|L), \tag{2.22a}$$

$$\mathcal{E}'_c(L) = -i\mathcal{E}'^*_s \frac{\eta_c}{|\eta_p^*|} \sinh(|\eta_p|L). \tag{2.22b}$$

As $\chi_{pc} = \chi^*_{cp}$ and therefore $\eta_p/k_p = \eta^*_c/k_c$, this gives the result for the output intensity $E_{p/c} = |\mathcal{E}_{p/c}|^2$ of the two fields as

$$E_p(L) = E_s \cosh^2(|\eta_p|L), \tag{2.23a}$$

$$E_c(L) = E_s \sinh^2(|\eta_p|L). \tag{2.23b}$$

In terms of an overall gain factor

$$G = \cosh^2(|\eta_p|L), \tag{2.24}$$

both of these can now be written as

$$E_p(L) = GE_s, \tag{2.25a}$$

$$E_c(L) = (G-1)E_s. \tag{2.25b}$$

Next we show the effect of this amplification on the quantum state of the field modes that leads to the generation of a TMSS.

The Effect of Gain on Quantum States

Any linear amplification of an electromagnetic field can be shown in the quantised picture to be equivalent to introducing an extra noise term as noiseless quantum amplification is known to be impossible [81]. This can be seen by considering the counter-example of a noiseless amplifier that takes an input state $\hat{a}$ and modifies it to

an amplified state $\hat{a}_{out} = \sqrt{G}\hat{a}_{in}$. When looking at the commutator of these states,

$$[\hat{a}_{out}, \hat{a}^{\dagger}_{out}] = G[\hat{a}_{in}, \hat{a}^{\dagger}_{in}] = G \neq 1, \tag{2.26}$$

which gives the incorrect result for the commutator of $\hat{a}$ with $\hat{a}^{\dagger}$ for the output state.

Instead the correct formulation is

$$\hat{a}_{out} = \sqrt{G}\hat{a}_{in} + \sqrt{(G-1)}\hat{b}^{\dagger}, \tag{2.27}$$

where $\hat{b}$ is the annihilation operator for a second field mode from which energy is transferred into the amplified field. In the case of amplification of the $\hat{a}$ field mode in the absence of any other fields, the mode $\hat{b}$ is the vacuum field. The variance on the output can now be defined as

$$\langle(\Delta\hat{a}_{out})^2\rangle = G\langle(\Delta\hat{a}_{in})^2\rangle + (G-1)\langle(\Delta\hat{b}_0)^2\rangle, \tag{2.28}$$

where $\langle(\Delta\hat{b}_0)\rangle = 1$ at the QNL and in cases where G $\gg$ 1 the signal to noise ratio (SNR) is increased by a factor of 2.

This process is referred to as phase-insensitive amplification as the resultant noise increase is added indiscriminately to all quadratures of the field, generating a larger 'fuzzball' on the output state.

Amplification that does not act to add equal noise onto all quadratures is also achievable without causing an unphysical commutator in the result. When the field on the input is described again as in equation 1.6, then the output can be written as

$$\hat{a}_{out} = \frac{1}{2}(\sqrt{\kappa}\hat{X} + \frac{i}{\sqrt{\kappa}}\hat{Y}), \tag{2.29}$$

where in the above case the amplitude quadrature is amplified while the phase

quadrature is de-amplified.

In this way it is clear that the process of phase-sensitive amplification acts to generate a squeezed state. The 4WM under consideration here however is a phase insensitive process that indeed adds noise to each field present in a uniform manner. It is only when looking at the number differences caused by the pairwise nature of the photon production that the two-mode squeezing becomes apparent.

If only the cross terms of the susceptibility, $\chi^{(C)}$ from equations 2.15a and 2.15b, are considered, as would be the case for ideal phase insensitive amplification, the two fields can be quantised in the following form with

$$E_p \rightarrow \hat{a}, \tag{2.30a}$$

$$E_c \rightarrow \hat{b}, \tag{2.30b}$$

and the effect of passing through the gain medium described by relating the input and output fields in accordance with equations 2.21 a and b, and the gain factor given in equation 2.24

$$\hat{a}_{out} = \sqrt{G}\hat{a}_{in} + \sqrt{G-1}\hat{b}^{\dagger}_{in}, \tag{2.31a}$$

$$\hat{b}^{\dagger}_{out} = \sqrt{G}\hat{b}^{\dagger}_{in} + \sqrt{G-1}\hat{a}_{in}. \tag{2.31b}$$

Given a coherent state $|\alpha\rangle$ for the seed input of the probe, $\hat{a}$, and vacuum state input $|0\rangle$ on the conjugate mode $\hat{b}$ then the resulting expectations for the photon number operator $\hat{n}$, as defined in equation 1.9, at the output gives the desired result

$$\langle \hat{n}_{p,out} \rangle = G|\alpha|^2, \tag{2.32a}$$

$$\langle \hat{n}_{c,out} \rangle = (G-1)|\alpha|^2. \tag{2.32b}$$

This result is congruent with the description in the previous section and corresponds

to a factor of G increase on the amplitude of the probe and a factor of $(G-1)$ on that of the conjugate, to take into account the initial seed power on the probe that is absent from the conjugate channel.

It can be shown [82] that when looking at intensity difference squeezing, the resultant squeezing across two emitted bright fields in the ideal case is written as

$$S(\hat{n}_-) = \frac{1}{2G-1}, \tag{2.33}$$

where the result has been normalised to the QNL, such that clearly in these terms a gain value $G = 1$ (corresponding to no apparent interaction with the medium) produces $\langle(\Delta\hat{n}_-)\rangle = 1$, the QNL. This shows that the greater the level of gain on the fields while passing through the medium, the greater the level of squeezing on the TMSS at the output. However, for a more complete treatment, the effects of losses and absorption must also be taken into account.

Introducing Losses

The direct susceptibility terms in the propagation equations, χ_{pp} and χ_{cc}, give a measure for the losses of the respective fields in the medium. As the probe field is closer to resonance than the conjugate field, χ_{pp} has a far greater effect than χ_{cc}. A more detailed analysis of this is included in chapter 4 while here an overview in the above terms will suffice.

The effect of losses in the medium can be effectively treated in the same manner as the introduction of a beam splitter with transmission $t < 1$. In order to model the simultaneous processes of gain and loss, the picture to hold in mind is that of an alternating sequence of gain regions and loss elements, with gain regions acting as described and lossy elements treated as introducing vacuum into the state while reducing the intensity. The probe field is treated as passing through this sequence

while the conjugate field can be seen as passing purely through the gain medium relatively unaffected by loss as it is far from resonance. The conjugate gain will still be reduced from the ideal case due to the losses incurred on E_p.

While a full analytical treatment of this process has been performed by [83], in chapter 4 we instead calculate the overall effect by utilising the forms of the susceptibilities directly and calculating the expected gains as a function of the relevant detunings. The result is essentially similar to that described in the ideal case, but with a more subtle derivation of the gain factor G.

2.3.2 Polarisation of the Light Field

In the experimental setup, the pump and twin fields are all emitted in the same general forwards direction, as shown in figure 2.4. In order to remove the pump cleanly, we desire it to have an orthogonal polarisation to that of the probe/conjugate. As the same method is used in the injecting of the probe, the orthogonality of probe and pump is assured[2]. It only remains to demonstrate why the generated conjugate must also be orthogonally polarised to the pump. This can be shown from the following logic.

For a given F state there exists a set of $2F + 1$ Zeeman sublevels corresponding to $m_F = -F, -F + 1, ..., 0, ..., F - 1, F$. These are neglected in the level diagram displayed in figure 2.3, which instead shows a simplified form. The coupling between any pair of these gives rise to an individual dipole moment and coupling strength while the parametric nature of the process requires that the final state of the system is identical to that of the original state. Figure 2.5, shows an example where the system starts in a state m_f. From here a pump photon (red) is absorbed with a circular polarisation (either σ_+ or σ_-) and a conjugate photon (blue) is emitted with

[2]Note that some minor polarisation adjustment may occur due to Zeeman rotation as a result of any present B field, however this factor is assumed to be negligible.

linear polarisation ($\pi_\perp = \frac{1}{\sqrt{2}}(\sigma_+ + \sigma_-)$), thus driving the system in to a superposition state of $m_f = \pm 1$. From here, the coherence defines that only the inverse process will serve to return the system to the original state. Thus the second absorbed/emitted pair must also be orthogonal, with the emitted probe photon (green) featuring the same polarisation as the conjugate.

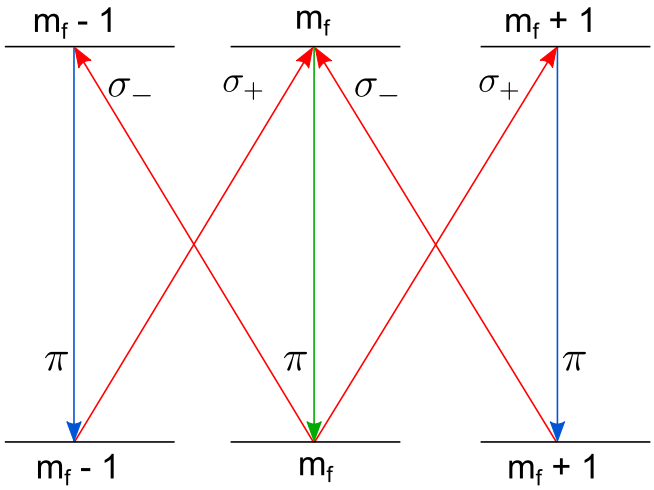

Figure 2.5: Shows an example of how for any given absorbed/emitted pair with orthogonal polarisation, the second process in the transition requires correlated polarisations in order to be parametric, as $\pi_\perp = \frac{1}{\sqrt{2}}(\sigma_+ + \sigma_-)$. Here red lines indicate pump photons, blue and green indicate probe and conjugate frequencies respectively, however these are effectively interchangeable.

As such, any given path for which the first absorbed and emitted photon are orthogonal enforces that the second pair also be orthogonal. In the experiment the pump photons come from the same S-polarised field, necessitating the emission of cross-polarised probe/conjugate pairs.

2.4 Parameter Optimisation

The gain from the 4WM process, G, is measured experimentally as

$$G = \frac{P_{p'}}{P_p}, \tag{2.34}$$

where $P_{p'}$ is the power on the output probe and P_p is the power of an input seed. The maximum level of intensity difference squeezing observable assuming zero losses is given in terms of the amount of gain experienced on a seed input by equation 2.33.

As the gain can be observed purely through a power measurement of the output probe beam it is a reasonable first approach to optimise the level of squeezing present by first optimising this gain[3].

The output gain is dependent on a number of parameters, including the temperature of the cell, the intensity of the pump, the detunings Δ_1 and δ (as defined in figure 2.3), and the input angle of the seed. Each of these parameters have essentially the same two effects. They all affect both the 4WM cross-coupling between the fields and the absorption of the probe, the specificities of which will now each be detailed individually.

2.4.1 Temperature

The temperature of the cell affects the atomic density as well as the Doppler broadening of the ^{85}Rb line widths due to the velocity spread of the atoms. The optimum temperature for our setup is 115 ± 5°C. Below this, the gain reduces along with the squeezing (as measured using the method discussed in section 5.2.6) while above this the increased Doppler broadening of the energy levels results in an increase in absorption on the probe channel with respect to the conjugate as the

[3]further optimisation may be required to maximise amplitude correlations or detection of squeezed vacuum, but maximising gain is always the first step.

probe transition is closer to resonance. This in turn drastically reduces the amplitude correlations. A check on the level of probe absorption due to temperature is to measure the power of the conjugate beam. For maximal correlations

$$P_c = P_{p'} - P_p, \tag{2.35}$$

where P_c, $P_{p'}$ and P_p are the powers of the conjugate, the emitted probe and the injected probe respectively. This is because every photon emitted into the conjugate field should have an analogue emitted into the probe field. If $P_{p'} - P_p < P_c$, this implies excess probe absorption[4] and the requirement of a reduction in temperature. If $P_{p'} - P_p > P_c$, then the 4WM coupling is not particularly efficient and a higher temperature may be desired.

Figure 2.6 shows how the output power of the probe and conjugate fields varies with the temperature of the cell. Note that the reading is taken from a thermistor and so a decrease in resistance corresponds to an increase in temperature. I.e. the left hand side of the figure corresponds to the higher temperature region. It clearly shows that as T is increased, the difference between probe and conjugate powers decreases while the gain on both continues to rise. After a certain point, the absorption increases to such an extent that the output fields are considerably weakened. In practice the value typically read on the temperature sensor is around $0.525\,\Omega$, which is below the point at which the relative intensity begins to decrease.

[4] Absorption of the probe is always stronger and thus more detrimental to the efficiency of the process than absorption of the conjugate as the probe is significantly closer to resonance.

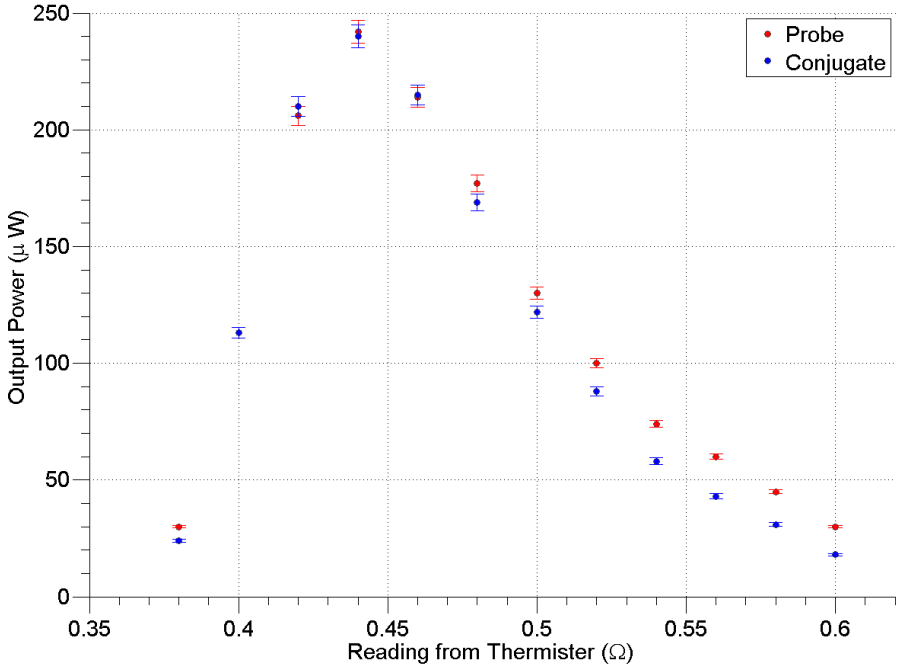

Figure 2.6: Shows how the output power of the probe and conjugate fields varies with the temperature of the Rb cell. Readings are taken from a thermistor positioned as shown in figure 3.4, meaning higher resistance values correspond to lower temperatures. For these readings δ was set to 0 MHz and the pump power was around 0.75 W. Errors correspond to 5 % of value and are from uncertainties in reading out from digital power meter.

2.4.2 Pump Power

A change in pump intensity changes the Rabi frequency (Ω) of the transitions coupled by ω_0 according to

$$\Omega_{i,j} = \frac{d_{i,j}E}{\hbar}, \tag{2.36}$$

where $d_{i,j}$ is the dipole moment between the states i, j, and E is the electric field coupling the transition. A plot of the probe and conjugate output powers with respect to a range of pump powers is shown in figure 2.7.

Up to a point, an increase in power tends to result in a gain increase but the maximum pump intensity achievable is limited due to available power coming from the source laser and the desire to have a large transverse spatial pump region in order to maximise the probe/pump overlap and increase the number of spatial modes across which the squeezing is produced[5]. For a $1/e^2$ pump waist of $\sim 1\,\text{mm}$ and power of $\sim 0.8\,\text{W}$ the resultant pump intensity of $\sim 260\,\text{mW}\,\text{mm}^{-2}$ is comparable with that used in previous experiments[52] but with a notably larger waist size. Diminishing returns are seen from continued power increase due to saturation effects and so it is not required to raise it above the value used.

2.4.3 Pump Detuning

The single-photon detuning Δ_1 is controlled by fixing the frequency of the pump[6]. When adjusting it in any situation where 4WM is being observed, the response of the gain has a clear maximum when the wavelength of the applied pump is set to around 794.974 nm. This can be seen as a peak in the observed probe/conjugate power on the output from the cell. After reaching this maximum and then locking

[5]See section 5.2 for further information on how the spatial squeezing bandwidth is related to the pump profile.

[6]Descriptions of how various parameters are adjusted in the experiment are given in chapter 3

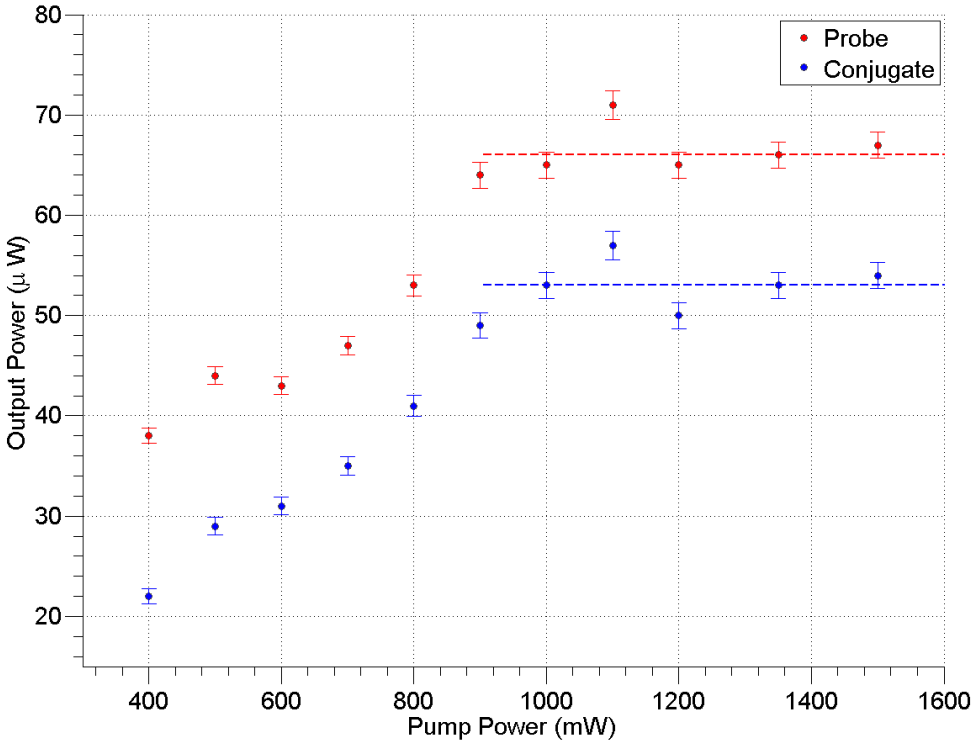

Figure 2.7: Shows how the output power of the probe and conjugate fields varies with the power of the applied pump field. The dashed lines indicate the levelling off of resulting output power as pump power is increased. For these readings δ was set to 0 MHz and the reading from the thermister was around 0.520 Ω. Errors correspond to 5 % of value and are from uncertainties in reading out from digital power meter.

the laser this factor becomes a fixed parameter with a value $\Delta_1 \approxeq 140\gamma$ where γ is the decay rate of the excited state, $\gamma = 2\pi \times 6\,\text{MHz}$.

2.4.4 Probe Detuning

The optimal operational value of δ that maximises squeezing effects is 0 MHz.

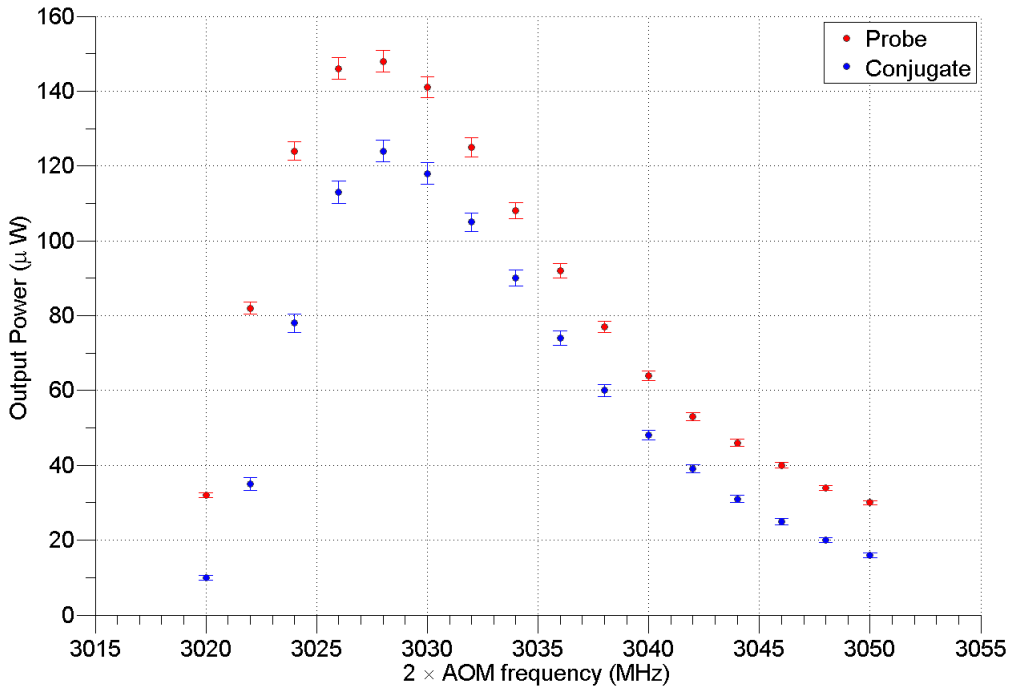

Figure 2.8: Shows how the output power of the probe and conjugate fields varies with the two-photon detuning δ. The recorded values correspond to the total frequency shift between the probe and pump fields caused by passing an element of the pump field through an AOM in a double-pass arrangement, as discussed further in chapter 3. For these readings the reading from the thermister was around 0.520 Ω and the pump power was around 0.75 W. $\delta = 0$ corresponds to a position on the chart equal to the separation between the two ground-state levels in ^{85}Rb, i.e. 3036 MHz. Errors correspond to 5 % of value and are from uncertainties in reading out from digital power meter.

Figure 2.8 shows the output powers of the probe and conjugate fields with respect to a range of values of δ.

Chapter 3

Experimental Generation of Four-Wave Mixing

This chapter will describe in detail the 4WM setup used to perform the experiments described in the following chapters, 4 and 5. Further considerations specific to each experiment will be detailed in the respective chapters, while the fundamentals described here underlie both.

Figure 3.1 shows the optical arrangement of the experiment, describing the formation of both a pump and probe field and directing these into a 12.5 mm glass cell of ^{85}Rb where 4WM takes place.

3.1 Generating the Four-Wave Mixing Beams

The pump beam used to drive the 4WM transition comes from a Titanium-Sapphire (Ti:Saph) laser from 'M Squared' capable of emitting approximately 3 W over a tunable wavelength between $720 - 900$nm. The frequency is selected via a laptop program while the laser itself is pumped by a 532 nm Coherent V12 laser operating at 11 W. This beam is tuned to around 794.974 nm by a three-level tuning mechanism

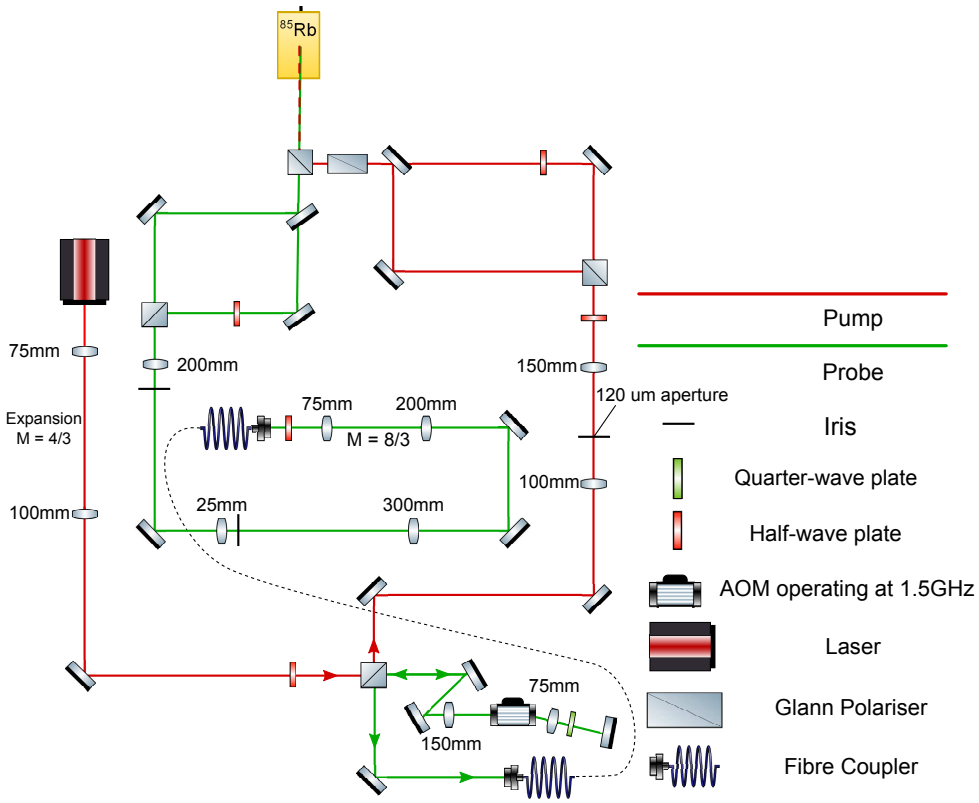

Figure 3.1: The experimental setup for achieving the 4WM is shown in detail. The laser emits a field (power $\sum 2.5\,\mathrm{W}$, wavelength $\lambda \sim 795\,\mathrm{nm}$) which takes the role of the pump field in the 4WM process. From this, a fraction ($\sim 40\,\mathrm{mW}$) is diverted through an AOM operating at around 1.5 GHz. A double-pass through this devices causes an overall frequency shift of around 3 GHz. The output from this double pass then passes through a fiber coupler that acts as a spatial mode cleaner, before also being directed into the ^{85}Rb cell. The shifted beam acts as the probe in the seeded 4WM process.

in which the internal birefringence filter (BRF) provides accuracy to around 0.25 nm, an etalon lock tunes to the nearest 0.002 nm and a two-stage cavity lock can be used for fine tuning beyond that level to pm precision. The Ti:Saph is in the form of an entirely self-contained and compact system as shown in figure 3.2, while the frequency is monitored on a wave meter.

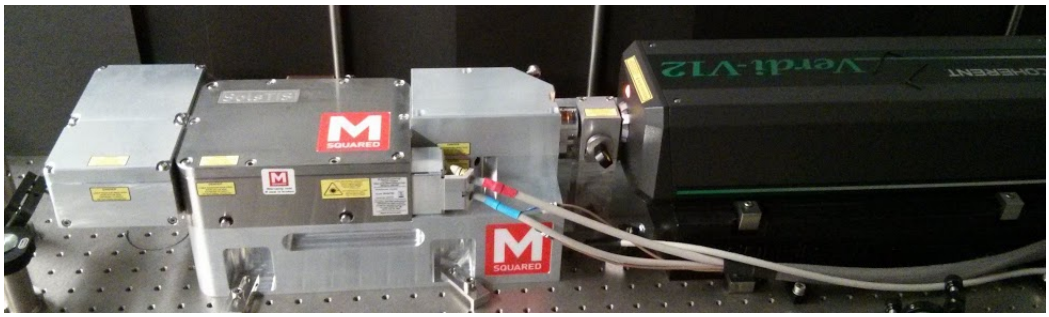

Figure 3.2: Shows the self-contained Titanium-Sapphire laser (on the left) mounted on a solid base plate and containing a BRF tuner, etalon lock and two-stage cavity lock all controlled via laptop. The laser is pumped by a Coherent V12 Verdi (on the right) operating at 532 nm.

A fraction of this pump beam (40 mW) is diverted and frequency shifted by ~ 3 GHz. This diverted fraction will form the probe beam used to seed the 4WM process. This frequency shift is achieved by sending the probe through an acousto-optical modulator (AOM) operating at around 1.5 GHz in a double-pass arrangement as shown in the bottom right of figure 3.1. This AOM consists of a piezo-electric device coupled to a crystal, in turn coupled to an absorber. The piezo applies a resonant acoustic signal to the crystal, generating a travelling phonon wave that scatters a portion of the applied light field in accordance with Bragg diffraction. The result is that the scattered portion emerges at an angle relative to the rest of the beam and with a frequency shift determined by the frequency of the acoustic signal,

f_{ac}.

$$f_{out} = f_{in} \pm n f_{ac}. \tag{3.1}$$

The sign of the shift and the order of diffraction, $n = 0, 1, 2, ...$, are governed by the angle of input with the optimum angle varying with frequency. Here we down-shift the frequency to the first order to form the probe used to seed the 4WM process.

The AOM is mounted onto a 3-axis prism mount to increase the ease of coupling. This allows for adjustment of the angle of the crystal relative to the incoming beam around three axes. The efficiency of the AOM is related not only to the coupling of the field into the device but also the operating frequency. For optimum performance, if the applied signal frequency to the AOM is shifted, then the input mirrors for both the single and double pass, as well as the angle of the AOM itself should all be adjusted.

During the double-pass through the AOM any noise on the amplitude of the acoustic signal will also be transferred to the emitted light field. As the twin beams emerging from the cell will be used to measure the extent of the squeezing produced, it is important that the noise on the input seed be as close to the SNL as possible. Noise measurements on the probe fraction of the Ti:Saph laser output showed it to be operating at the SNL for a typical power value of 40 mW, making it important to reduce the amplitude fluctuations on the RF signal to the AOM as much as possible.

The noise from the signal generator driving the AOM was found to be minimised when operated at its maximum output level of 20dBm. To decrease this further the output was then passed through three stages. Firstly a limiter with a maximum output of 12dBm, then an amplifier limited at 13dBm. The signal is then reduced by 15dBm before finally being passed to a table amplifier hooked up to the AOM. At each of these stages the input signal is greater than the output level of the device,

meaning the device is saturated. This saturation causes a waveform with a 'flat top' profile and minimal amplitude noise. A side-effect of this flat top signal is the generation of additional harmonics on the signal, but they are separated from the main frequency by a large enough amount as to no longer be resonant with the device. In addition any generated harmonics applied to the beam would result in an output field spatially separated from the one desired and easily removable. The noise measured on a beam after the frequency shift was seen to still be at approximately the shot noise level (for output powers of $300\,\mu W$).

To achieve the desired shift in beam frequency of around 3 GHz, it is necessary to send the beam through the AOM twice. This is done with a retro-reflection technique whereby the beam is passed through a $\frac{\lambda}{4}$ wave-plate then reflected back onto itself by a mirror, back through the wave-plate and back through the AOM. This setup is shown in the lower-right portion of figure 3.1. The emerging beam after the double-pass then has a total frequency shift of $2f_{ac}$ in addition to a polarisation rotation of $\frac{\pi}{2}$ allowing for separation from the incoming beam via a polarising beam splitter.

Due to the unusually high operating frequency of the AOM[1], its diffraction efficiency is fairly low ($\sim 10 - 12\%$). Typically after the double-pass the remaining power is of the order of a few hundred µW. This is then directed through a fibre in order to rectify the spatial profile of the beam which which would otherwise become distorted as a result of the AOM double-pass. The fibre itself operates with an efficiency of 40% (relatively low, a result of the spatial deformation of the field at this point), and directs the output towards the centre of the experiment, giving a typical operational probe beam power of $100\,\mu W$.

[1]Standard expectations of an AOM are to shift the frequency of a beam by the order of up to a few hundred MHz, and are often used more for the speed with which the shifted beam can be turned on/off. In fact the ability to obtain an AOM capable of reaching this kind of frequency was key in being able to exploit this particular 4WM system without necessitating the use of a second laser.

After the emission point of the fibre, an imaging system is used to re-size and collimate the probe field, while positioning the beam waist inside the cell. The size of the probe waist as measured inside the cell is approximately 0.5 mm. The imaging system is described in more detail in section 5.2.2.

The size and position of the pump beam waist is also controlled. A pair of lenses collimate it to around $w_0 = 1\,\text{mm}$ before the field is then directed to the ^{85}Rb cell. A 120 µm circular aperture is positioned at the confocal point of this telescope to spatially filter the profile of the pump beam. It acts to remove higher order spatial modes, as in the focal plane these are located towards the edges of the field profile.

Placed just in front of the entrance to the vacuum chamber is a polarising beam splitter. The bright pump beam and weak probe beam have orthogonal linear polarisations[2] such that the p-polarised probe is transmitted through the splitter while the s-polarised pump is reflected. Here the two beams are overlapped and sent into the cell as in figure 2.4. Prior to the splitter the bright pump passes through a Glan polariser also aligned to transmit s-polarised light in an attempt to reduce the amount of cross polarised pump light entering the cell region. The use of the polariser and beam-splitter in combination is both as a two-stage polarisation filter on the pump and also for ease of access experimentally as on the beam splitter, the fields can enter from orthogonal directions. At the exit of the cell is a second Glann polariser that directs the pump light away from the probe/conjugate beams. In practice around $40 - 60\,\mu\text{W}$ of pump light is liable to be transmitted even through these numerous polarisers, but this is typically blocked at a later point and not recorded by the various detectors, as can be tested by removing all other light sources.

The characteristics of the fields inside the cell are summarised in table 3.1.

[2]See section 2.3.2.

Pump	
Power	750 mW
Waist	1.8 mm
Frequency	794.974 nm

Probe	
Power	100 µW
Waist	0.8 mm
Detuning	3036 MHz

Table 3.1: Table displaying the power, beam waist and frequency of the applied pump/probe fields within the cell. Frequency for the probe is given in terms of the detuning applied by the AOM double-pass.

3.2 Housing the ^{85}Rb Cell

The centrepiece of the experiment is a 12.5 mm length glass cell of isotopically pure ^{85}Rb (Triad Technologies, purity guaranteed $> 98\%$). The arrangement inside the chamber is shown in figure 3.3. The cell features anti-reflection coatings on the outside of the face windows to reduce stray losses from the emitted twin beams at the interfaces. The cell is encased in a lens tube which is in turn wrapped in a coil of nichrome wire. This wire features a high resistivity (of order 1.1 Ω m) and when current is passed through it, a large amount of heat is emitted, increasing the temperature of the cell. Operationally the signal passed through the wire is at Also present are a thermo-electric cooler (TEC) and a thermistor, both connected to an external control unit. This control unit monitors and adjusts the current to the TEC, regulating the heat transfer to and from the cell in order to maintain a stable temperature, as recorded by the thermistor. When settled the resistance measured varies by less than 1 mΩ the smallest increment readable on the stabilisation unit. All of this is located inside a KF vacuum setup, shown in figure 3.4, pumped down by a roughing pump to around 1 mbar. The pressure inside the vacuum setup is not required to be as low as in a ultra-high vacuum (UHV) system as its purpose is

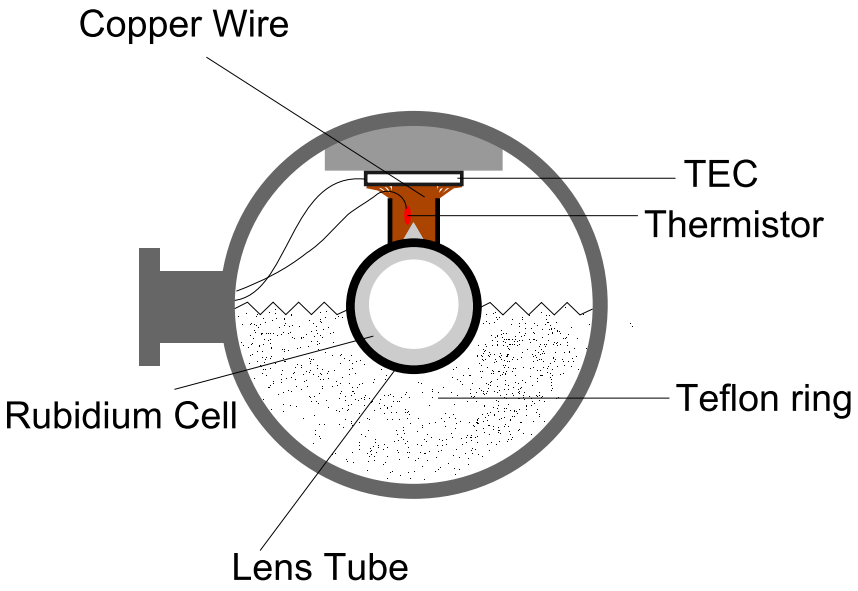

Figure 3.3: Within the chamber a lens tube is raised by a pair of Teflon rings so as to be coxial with the vacuum system. Heat is transferred to the body of the chamber via copper wire. This passes through a TEC used to maintain the temperature which is in turn monitored by a thermistor also located in the wire. Around the lens tube is wrapped nichrome wire (not shown), through which current is passed in order to heat the system.

merely to remove convection currents at the ends of the heated lens tube containing the cell. These air flow currents would otherwise cause fluctuations in the position of the laser beams at the output, making it impossible to accurately mode-match the beams on the output, an important requirement for the experiment covered in chapter 5. In practice the cell is pumped down with a roughing pump once every 3-4 months then maintained at this reduced pressure with a basic butterfly valve. Two large windows (open diameter 49 mm), also with an anti-reflection coating (specified to give $R < 0.2\%$ at 795 nm) are placed at the points of beam entry/exit in order to minimise losses through the chamber.

With this combination of aligned pump/probe and housed ^{85}Rb cell, bright twin beams or TMSS of vacuum can now be generated. The arrangement allows for a large degree of control over beam sizes, input angles, powers and frequency tunings as well

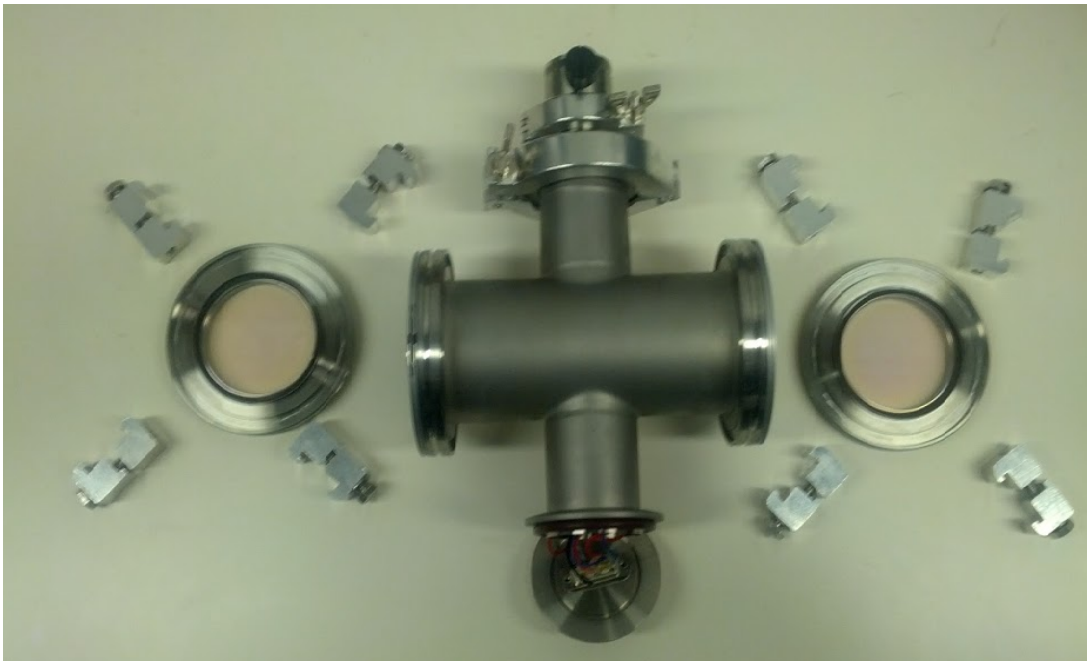

Figure 3.4: An exploded view of the vacuum chamber, showing the windows (open diameter 60mm), valve and electronic feed-through.

as over the cell temperature and internal pressure. The analysis and manipulation of these twin beams will form the crux of the experiments described in the coming chapters.

Chapter 4

Analysis of the Four-Wave Mixing Feature

This chapter will focus on the form of the susceptibilities described in section 2.3 that serve to characterise the ^{85}Rb in the presence of the coupling fields. Particular attention is given to the phase-matching condition (as defined in equation 2.7) and how the setup presented allows for the generation of strongly correlated signals and bright twin beams despite the proximity to an atomic resonance.

It will be shown that maximising the 4WM coupling strength via the phase-matching condition does not produce the squeezing effect desired due to the deleterious increase in probe absorption. Finally the optimum alternative setup for maximising the extent of measurable squeezing will be justified.

4.1 Motivation for the Analysis

In the case of 4WM in ^{85}Rb, the nonlinear effect is the result of a strong coupling between probe and conjugate transitions (as seen in figure 2.3) when in the presence of an applied pump field. The strength of the cross-coupling can be viewed in the

form of the gain experienced by an injected probe field that undergoes amplification in the 4WM system. In order to maximise the extent of this amplification, and therefore the gain, the probe field should be inserted in a manner that satisfies the phase matching condition which equates to a case where $\Delta\mathbf{k} = 0$.

When looking to generate strongly squeezed light, a high level of cross-coupling is desired as this is the source of the photon pairs that result in the amplitude correlations. At the same time the level of absorption on the probe field must be kept to a minimum as the absorption of photons at the probe frequency will clearly result in a reduction of correlated pairs being emitted and as such a reduction in the squeezing detected. The balance of these two factors, the level of cross-coupling and degree of absorption, is ultimately responsible for the level of squeezing produced by the system, and both are closely related to the susceptibility of the medium.

Theoretically, as assumed by Lukin [84], the optimum way to satisfy the phase-matching condition would be to generate an electromagnetically induced transparency (EIT) condition. EIT describes a state of an atomic system in a quantum superposition of two coupled states that allows for absorption-free transmission of light through an otherwise optically opaque medium. This permits the strong coupling strength associated with fields close to atomic resonances to behave as though unimpeded by absorption. The concept was first described theoretically in 1989 [85] then seen experimentally in 1990 [86].

The generation of EIT here would involve the situation in which both the probe and conjugate fields see the atomic medium as transparent. The requirement for EIT is a strong level of coherence between the two coupled transitions and this is achieved when δ, the detuning of the probe field from the two-photon resonance, (as described in section 2.2) is set to 0 and both probe and conjugate fields couple to the ground states perfectly. The successful formation of an EIT state would implicitly result in minimal absorption, while simultaneously providing strong coupling as the

fields would be almost resonant.

Experimentally, the generation of strong squeezing in a hot vapour experiment via EIT has proved difficult to obtain due to the degree of decoherence caused by the vapour. Decoherence, mediated by non-radiative processes that result in the transition of atoms between the two coupled states, causes a dephasing of the system. Over time it inevitably evolves from the idealised EIT 'Dark State' into a bright state, where the strong resonance of the coupling fields results in increasing levels of absorption as the coherence decreases. The rate of this ground state decoherence is categorised as γ_c, where a low γ_c means long lasting strong coherence while a high γ_c means swift decoherence. As will be shown, the effects of absorption are strong enough that anything less than almost perfect EIT fails to produce the desired effect. A breakdown of the atomic decoherence effects within ^{87}Rb and how they affect the generation of EIT can be found in [87].

The reason for the poor degree of EIT obtainable in atomic vapours is that a number of dephasing effects such as Doppler broadening of line widths, collision broadening, finite transit time across the beams and hyperfine splitting of the transition lines all take place. These combine to produce a large γ_c, with the result that ideal EIT is unobtainable and despite high gain levels, the absorption totally removes any chance of seeing squeezing below the shot noise.

However, the experimental arrangement used in this thesis still shows high levels of squeezing despite the absence of an EIT transparency window. In order to explain how this is achieved, the process must be analysed more closely. That analysis is the focus of this chapter.

4.2 Description of the Susceptibilities

Key to a full description of the atomic response is a formulation of the susceptibility that governs both the absorption and the cross-coupling strength. This susceptibility is related to the field detunings Δ_1, Δ_2 and δ, and the relative coupling strengths between the levels involved. These are all defined in figure 4.1, along with the numerical level designations.

To demonstrate the relationship it is convenient to first expand the susceptibility of the medium in the presence of the strong pump field into four parts, as established in section 2.3. These break down into two direct terms, referring to the behaviour of the probe field (in χ_{pp}) and the conjugate field (χ_{cc}) and two cross terms describing the cross-coupling effect between the probe and conjugate fields, χ_{pc} and $\chi_{cp} = \chi_{pc}^*$. The direct terms are effectively the linear susceptibilities corresponding to the complex refractive index and describe both the refractive index of the medium as experienced by the fields (in the real parts) and the level of absorption (in the imaginary parts) while the cross terms correspond to the strength of the cross-coupling responsible for the 4WM process.

These χs take the place of $\chi_p^{(D)}$, $\chi_p^{(C)}$, $\chi_c^{(D)}$ and $\chi_c^{(C)}$ in equations 2.15a and 2.15b, giving a description of the polarisation response of the medium to the present fields as

$$P(\omega_p) = \epsilon_0 \chi_{pp}(\omega_p) \mathcal{E}_p e^{i\mathbf{k}_p.\mathbf{r}} + \epsilon_0 \chi_{pc}(\omega_p) \mathcal{E}_c^* e^{i(2\mathbf{k}_0 - \mathbf{k}_c).\mathbf{r}}, \tag{4.1a}$$

$$P(\omega_c) = \epsilon_0 \chi_{cc}(\omega_c) \mathcal{E}_c e^{i\mathbf{k}_c.\mathbf{r}} + \epsilon_0 \chi_{cp}(\omega_c) \mathcal{E}_p^* e^{i(2\mathbf{k}_0 - \mathbf{k}_p).\mathbf{r}}. \tag{4.1b}$$

The derivation of the susceptibilities that are found in these polarisation equations

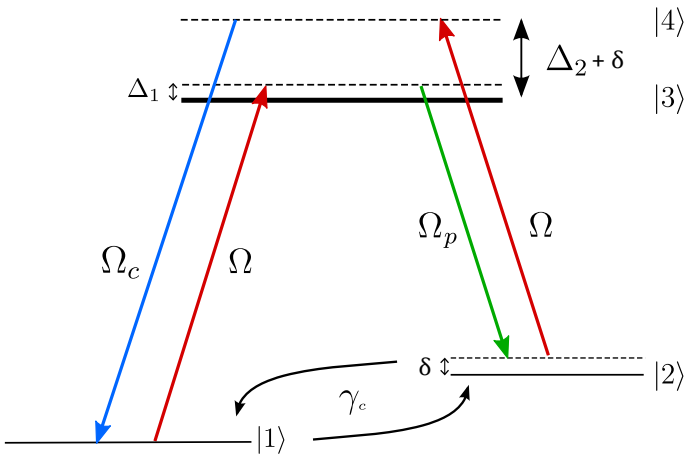

Figure 4.1: Shows the energy level diagram of ^{85}Rb with labels indicating the various states and Rabi frequencies used in the definitions of the four susceptibilities. Detunings are as described in figure 2.3

is detailed in appendix A. In full, they take the form [84]

$$\chi_{pp} = \frac{iN|d_{23}|^2\xi_{41}^*}{\epsilon_0\hbar D^*}\left[\frac{\xi_{21}^*}{\xi_{42}^*}\sigma_{22,44} + \frac{\xi_{43}^*}{\xi_{31}^*}\sigma_{11,33} - \left(\frac{\xi_{21}^* + \xi_{43}^*}{\xi_{41}^*} + \frac{\xi_{21}^*\xi_{43}^*}{|\Omega|^2/4}\right)\sigma_{22,33}\right], \tag{4.2a}$$

$$\chi_{cc} = \frac{iN|d_{14}|^2\xi_{32}^*}{\epsilon_0\hbar D}\left[\frac{\xi_{43}}{\xi_{42}^*}\sigma_{22,44} + \frac{\xi_{21}}{\xi_{31}^*}\sigma_{11,33} - \left(\frac{\xi_{21} + \xi_{43}}{\xi_{32}^*} + \frac{\xi_{21}\xi_{43}}{|\Omega|^2/4}\right)\sigma_{11,44}\right], \tag{4.2b}$$

$$\chi_{pc} = \frac{iNd_{14}d_{23}\xi_{41}^*\Omega^2}{\epsilon_0\hbar D^*|\Omega|^2}\left[\frac{\xi_{21}^*}{\xi_{31}}\sigma_{11,33} + \frac{\xi_{43}^*}{\xi_{42}}\sigma_{22,44} + \left(\frac{\xi_{21}^* + \xi_{43}^*}{\xi_{41}^*}\right)\sigma_{11,44}\right], \tag{4.2c}$$

$$\chi_{cp} = \chi_{pc}^* = \frac{iNd_{14}d_{23}\xi_{32}^*\Omega^2}{\epsilon_0\hbar D|\Omega|^2}\left[\frac{\xi_{43}}{\xi_{31}}\sigma_{11,33} + \frac{\xi_{21}}{\xi_{42}}\sigma_{22,44} + \left(\frac{\xi_{21} + \xi_{43}}{\xi_{32}^*}\right)\sigma_{22,44}\right], \tag{4.2d}$$

where N is the atomic number density of the medium, d_{ij} corresponds to the atomic dipole moment of the transition from j to i,

$$D = (\xi_{43} + \xi_{21})(\xi_{32}^* + \xi_{41}) + \frac{\xi_{32}^*\xi_{41}\xi_{43}\xi_{21}}{|\Omega|^2/4}, \tag{4.3}$$

and $\sigma_{ii,jj}$ are the population differences, governed by the complex decay rates, ξ_{ij}

and Rabi frequency of the pump field Ω

$$\sigma_{11,33} \equiv \sigma_{11} - \sigma_{33} \equiv \frac{|\xi_{31}|^2}{|\Omega|^2 + |\xi_{31}|^2 + |\xi_{42}|^2}, \tag{4.4a}$$

$$= \sigma_{11,44} \equiv \sigma_{11} - \sigma_{44} \equiv \frac{|\xi_{31}|^2}{|\Omega|^2 + |\xi_{31}|^2 + |\xi_{42}|^2}, \tag{4.4b}$$

$$\sigma_{22,33} \equiv \sigma_{22} - \sigma_{33} \equiv \frac{|\xi_{42}|^2}{|\Omega|^2 + |\xi_{31}|^2 + |\xi_{42}|^2}, \tag{4.4c}$$

$$= \sigma_{22,44} \equiv \sigma_{22} - \sigma_{44} \equiv \frac{|\xi_{42}|^2}{|\Omega|^2 + |\xi_{31}|^2 + |\xi_{42}|^2}. \tag{4.4d}$$

The complex decay rates are related to the field detunings, the ground state decoherence γ_c, and the natural decay rate from the excited states $|3\rangle, |4\rangle$, $\gamma = 2\pi \times 6\,\mathrm{MHz}$,

$$\xi_{43} = i(\Delta_2 - \Delta_1) - \gamma, \tag{4.5a}$$

$$\xi_{42} = i(\Delta_2 - \delta) - \frac{\gamma}{2}, \tag{4.5b}$$

$$\xi_{41} = i\Delta_2 - \frac{\gamma}{2}, \tag{4.5c}$$

$$\xi_{32} = i(\Delta_1 - \delta) - \frac{\gamma}{2}, \tag{4.5d}$$

$$\xi_{31} = i\Delta_1 - \frac{\gamma}{2}, \tag{4.5e}$$

$$\xi_{21} = i\delta - \gamma_c. \tag{4.5f}$$

These susceptibilities now describe in total the response of the medium for both probe and conjugate fields. Experimentally the susceptibility of the medium can be adjusted by setting the frequencies of the incident pump/probe fields or adjusting the cell temperature.

4.3 Mapping the Feature Theoretically

In this section, the form of the four component susceptibilities as well as the resultant gain predicted at the cell output will be displayed over a range of two-photon detuning δ. In order to produce these plots, first an experiment was performed (described in section 4.4). Using the results of this experiment and the equations given in both this section and section 4.2, optimum values were found for parameters not controlled directly in the experiment. With this we hope to optimise the value of δ both for the efficiency of 4WM and for the generation of squeezed output fields.

From the performed experimental fit displayed later in the chapter, values were optimised in the calculation of the susceptibilities for the following parameters. The value of the atomic number density N was set to $2.8 \times 10^{18}\,\mathrm{m}^{-3}$, the ground-state decoherence γ_c to 0.2γ, and the twin pump Rabi frequencies to the same value $\Omega = 2\pi \times 306\,\mathrm{MHz}$. In these calculations the various dipole transitions d_{ij} are also set as equal. Despite their different degeneracy, all d_{ij} are taken as $d = 1.4651 \times 10^{-29}\,\mathrm{C\,m}$, given in [78] as the effective dipole moment for the case of strong detuning and linearly polarised light. As a result it should be stated explicitly that this is not a thorough depiction of the medium, taking into account all Zeeman sub-levels and hyperfine couplings, but a reduced treatment of the four-level system that still serves to depict a lot of the physics at play.

4.3.1 Plotting the Susceptibilities

Figure 4.2 shows the four χ components plotted for $\delta = -10\gamma$ to $\delta_1 = 5\gamma$[1].

In these plots, the primary feature sitting at around $\delta = -5\gamma$ corresponds to the two-photon resonance. The resonance lies not at $\delta = 0$ due to the presence of a light shift induced by the strong pump field[88]. This shift corresponds to a change in

[1] As a single pump field is used to drive both transitions, Δ_2 is always equal to $\Delta_1 + \omega_{HF}$ as seen in figure 2.3.

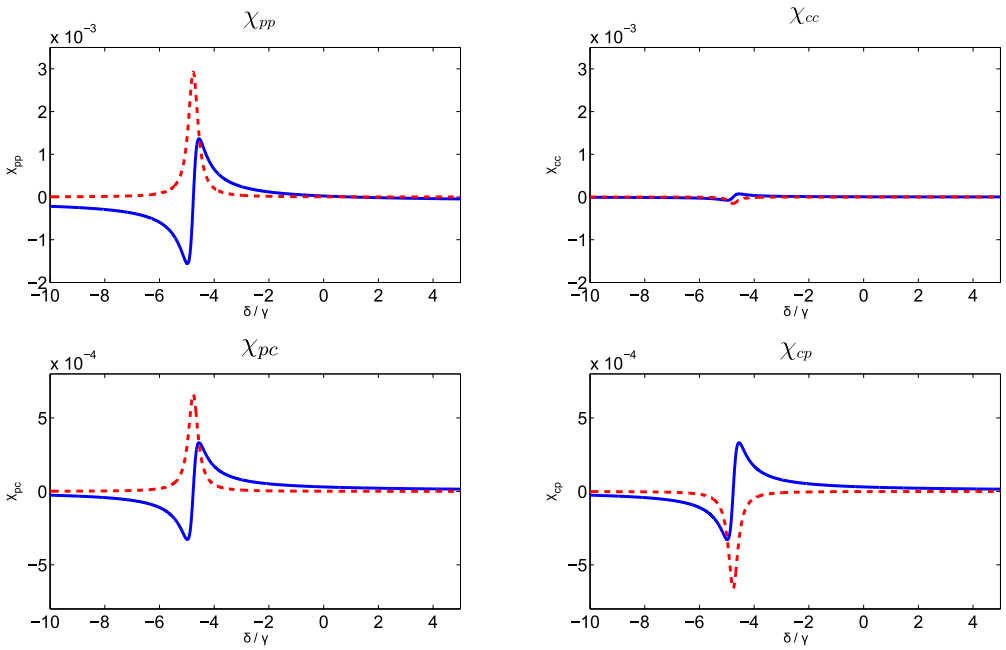

Figure 4.2: Shows the variation of the four component elements of the susceptibility (measured in arbitrary units) over a range of δ. The main feature shown to the left of $\delta = 0$ is the two-photon resonance. $\Re$ parts are shown in blue, $\Im$ parts in red.

the energy of the excited state equal to $E_{shift} = \Omega^2/4\Delta_1$. Given values of $\Omega = 60\gamma$ and $\Delta = 140\gamma$, the expected shift would be 6.4γ, similar to the value seen in figure 4.2 of 5γ. The plot demonstrates a large increase in absorption of the probe (seen in the peak in $\Im(\chi_{pp})$) at the same detuning value as the maximum value of the 4WM cross-coupling between the two fields (the peak in $\Im(\chi_{pc})$). The absorption on the probe decays faster than the gain peak on the cross couplings, leaving a region on either side of the resonance where competition between the two processes can result in a net gain for the probe. These regions set the parameter space for further investigation of the feature, as this net gain is required for the observation of squeezing. The larger single-photon resonance does not appear in the figure but can be seen if the range of the calculation is extended to $\delta = \Delta_1 \approx 140\gamma$, as seen in figure 4.3.

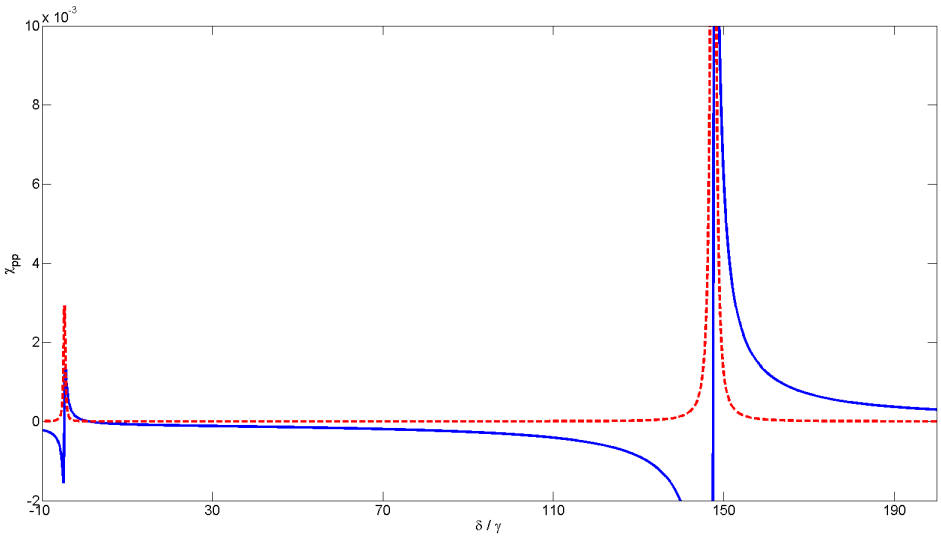

Figure 4.3: Shows the variation of χ_{pp} (measured in arbitrary units) over a wider range of δ, so as to include the single-photon resonance located at $\delta \approxeq 140\gamma$. $\Re$ parts are shown in blue, $\Im$ parts in red.

The highly off-resonant nature of the conjugate is displayed in the relatively low amplitude of the χ_{cc} plot. It also displays a small negative absorption feature, causing an amplification effect, although this can be taken as negligible with respect to the 4WM coupling.

The Effective Phase-Matching Condition

Recall from section 2.3 the propagation equations for the probe/conjugate fields

$$\frac{\partial \mathcal{E}_p}{\partial z} = \frac{ik_p}{2}(\chi_{pp}(\omega_p)\mathcal{E}_p + \chi_{pc}(\omega_p)\mathcal{E}_c^* e^{i\Delta k_z z}), \tag{4.6a}$$

$$\frac{\partial \mathcal{E}_c}{\partial z} = \frac{ik_c}{2}(\chi_{cc}(\omega_c)\mathcal{E}_c + \chi_{cp}(\omega_c)\mathcal{E}_p^* e^{i\Delta k_z z}), \tag{4.6b}$$

where the dependence is shown not only on the χ terms but also the effective phase mismatch Δk_z.

To investigate the effect of this phase mismatch Δk_z, a direct connection can be

formed between the magnitude of Δk_z and the relative input angles of the pump and probe fields.

In the calculations of χ, the refractive index n induced by the 4WM process is implicit. E.g. n_p, the induced index on the probe field caused by the cross-Kerr effect between the pump and probe fields is included in the polarisation equations and is governed by the form of χ_{pp}. Here, we extract it by making a modification to equation 2.7, in order to show the effect of adjusting the angle of input of the seed. The refractive index for each field should be considered individually, resulting in $n_p, n_0 and n_c$. However n_c, n_0 can be considered as negligible compared to n_p, n_c because it is further from resonance (see $\Re(\chi_{cc})$ in figure 4.2) and n_0 as comparatively the probe is orders of magnitude weaker than the pump. Re-introducing only n_p generates an 'effective phase matching condition', satisfied when

$$\Delta\mathbf{k} = 2\mathbf{k}_0 - n_p\mathbf{k}_p - \mathbf{k}_c = 0, \tag{4.7}$$

where $n_p = \sqrt{1 + \Re(\chi_{pp})}$.

The first part of figure 4.4 shows that in free space the condition that $\Delta k_z = 0$ is identical to the condition $\Delta\mathbf{k} = 0$ and is satisfied by a co-linear arrangement. At values of δ located around $\delta = 0$, $\Re(\chi_{pp}) \approx 0$, $n \approx 1$ and this free space picture is appropriate.

However, if δ is brought closer to the resonance, $\Re(\chi_{pp})$ increases. The second diagram in figure 4.4 shows that when $n \neq 1$, the co-linear picture no longer satisfies that $\Delta\mathbf{k} = 0$. In order to correct for this, and generate strong 4WM it is necessary to introduce an angle θ between the pump and the probe/conjugate, as shown in the final diagram of the same figure, with the equivalent result that Δk_z is no longer 0.

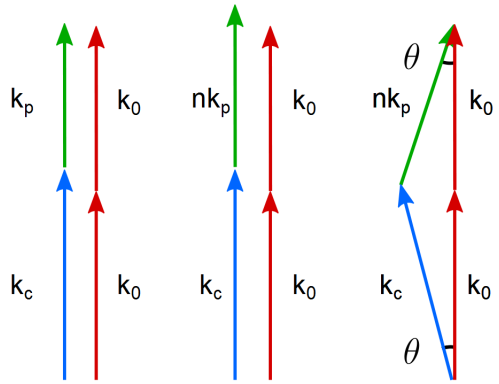

Figure 4.4: Shows the effect of the geometric phase matching condition. In the first case the wave vectors of the probe (green) and conjugate (blue) sum to equal the length of two wave vectors for the pump (red). This is the phase matching condition in free space. In the second and third case, the refractive index of the medium, n, changes the effective length of the probe vector resulting in a phase mismatch. The introduction of the angle θ corrects for this. In the third case we see that while $\Delta\mathbf{k} = 0$, $\Delta k_z \neq 0$

The correspondence between θ and Δk_z is

$$\Delta k_z = 2k_0 - n_p k_p \cos(\theta) - k_c \cos(-\theta), \tag{4.8}$$

where the value of θ is taken to be the same in both cases as the photon pairs are emitted in equal and opposite directions with respect to the pump[2].

By equating this Δk_z adjustment to a change in the input angle of the seed, this can now also be tested experimentally to see the effect of adjusting either $\Delta k_z/\theta$ or δ on the gain generated. For an adjustment made to δ towards the negative side of the susceptibility plots shown in figure 4.2, taking it below 0 and closer to the two-photon resonance, the correcting angle adjustment is made by an increase in θ.

Finally, the situation of $\Re(\chi_{pp}) < 1$, caused by a tuning of δ beyond the two-photon resonance, can never be manipulated so as to satisfy the phase-matching condition. That is to say a reduction in the length of the vector k_p from its length in

[2]Strictly speaking, as $\omega_p \neq \omega_c$, $\theta_p \neq \theta_c$ but in practice this discrepancy is negligible.

free space cannot be corrected for by any angle. As such only the region of the plot $\delta > -5\gamma$ is investigated.

By operating at a wider angle and bringing δ closer to the resonance both the 4WM coupling between the probe and conjugate fields, i.e. $|\Im(\chi_{pc})|$, and also the absorption on the probe field, $\Im(\chi_{pp})$ increase. The result is that these competing effects both affect the overall gain experienced by the probe.

Clearly, the condition that $2k_0 - k_p - k_c = 0$ is always enforced by the law of conservation of momentum.

Calculated Gain Plots

In order to investigate the region around the two-photon absorption more closely, where the competing effects occur most strongly, the process was emulated to display the results of adjusting various parameters. Firstly the solution for the propagation equations (2.16a) can be found [84] for the case where an input seed beam $\mathcal{E}_s$ is injected and there is no input conjugate field. The value for the field amplitudes of the probe/conjugate, $\mathcal{E}_p/\mathcal{E}_c$, after travelling a distance L in the 4WM medium are taken to be

$$\mathcal{E}_p(L) = \mathcal{E}_s e^{a-L}\left[\cosh(\xi L) + \frac{a_+}{\xi}\sinh(\xi L)\right], \tag{4.9a}$$

$$\mathcal{E}_c^*(L) = \mathcal{E}_s e^{a-L}\frac{a_{cp}}{\xi}\sinh(\xi L). \tag{4.9b}$$

All terms are condensed arrangements of the susceptibilities (described in equations 4.2a - 4.2d) and the wave vectors of the fields where

$$\xi = \sqrt{a_+^2 - a_{pc}a_{cp}}, \tag{4.10}$$

$$a_+ = \frac{a_{pp} + a_{cc} - i\Delta k_z}{2}, \tag{4.11}$$

$$a_- = \frac{a_{pp} - a_{cc} + i\Delta k_z}{2}, \tag{4.12}$$

and

$$a_{pi} = \frac{ik_p\chi_{pi}}{2}, \tag{4.13}$$

$$a_{ci} = \frac{ik_c\chi_{ci}^*}{2}. \tag{4.14}$$

Using these propagation equations, and the argument presented in the previous subsection for equating the phase mismatch to a non-0 input angle of the probe, the gain can be calculated for a range of θ (equating directly to a change in Δk_x) and δ.

The gain is displayed for both the probe and conjugate fields in terms of the ratio between output field power and input seed power, with the probe gain equal to

$$G_p = \frac{|\mathcal{E}_p(L)|^2}{\mathcal{E}_s^2} \tag{4.15}$$

and conjugate gain

$$G_c = \frac{|\mathcal{E}_c(L)|^2}{\mathcal{E}_s^2}. \tag{4.16}$$

The result of this is shown in figure 4.5.

In figure 4.5 the two-photon detuning is plotted against the input angle θ and the corresponding gain is shown for both the probe and conjugate fields. These show that as θ increases, along with Δk_z, the corresponding detuning required to maximise

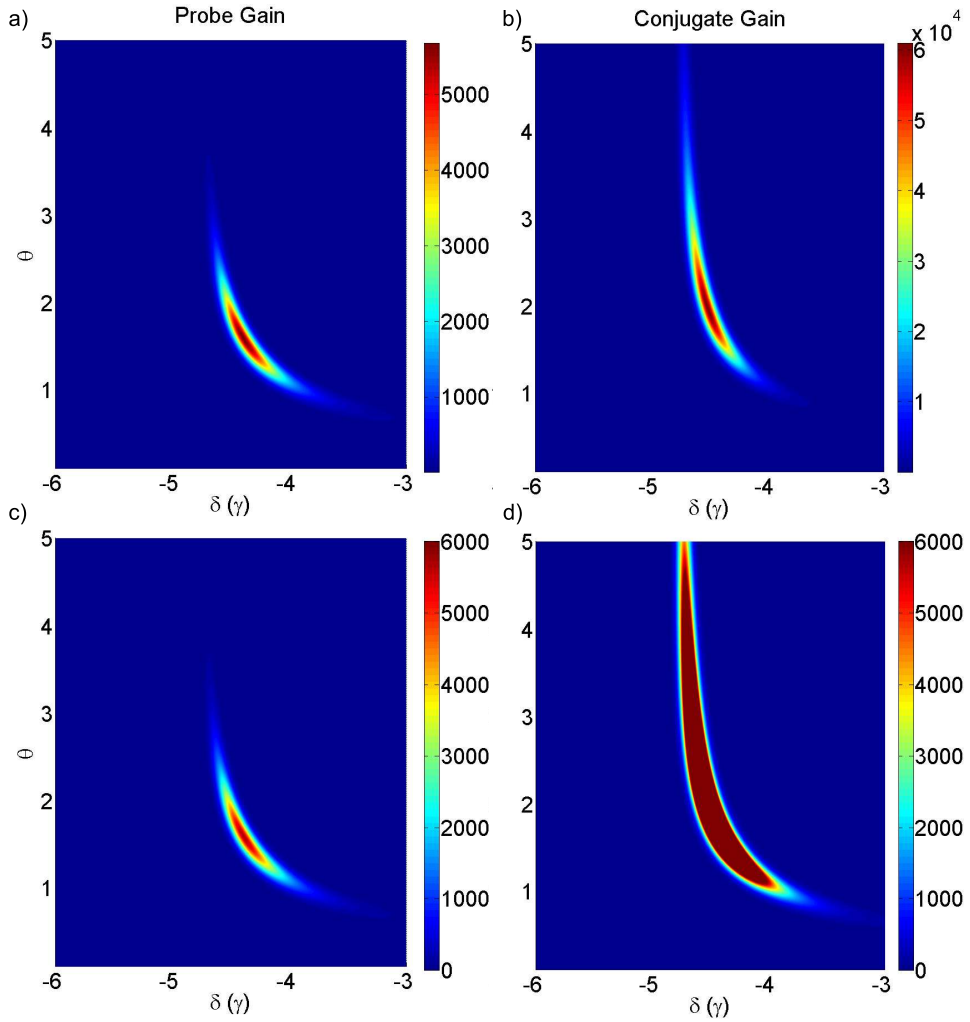

Figure 4.5: Shows the full theoretical gain feature over a range of δ and θ for both a) the probe and b) the conjugate. The colour bar indicates the expected gain at that location in the parameter space. c) and d) show the same image but re-scaled so the conjugate is shown over the same range of gain values as the probe.

the gain output moves towards the two-photon resonance. The gain feature curves asymptotically as it approaches the two-photon detuning at $\delta \approx -5\gamma$. The drop-off seen as the resonance is approached is the result of the high level of probe absorption, $\Im(\chi_{pp})$. At very low angles, essentially approximating the co-linear picture, very little gain is seen, if any, regardless of the detuning. This correlates with the fast drop-off seen in the cross terms of the susceptibility, where the 4WM interaction is relatively weak due to the distance from the resonance and drop in coherence.

The plot also shows a discrepancy between the behaviour of the probe and conjugate. The maximum gain on the conjugate is achieved at a value of δ closer to the resonance and correspondingly a higher input angle. Also the largest gain value for the conjugate is an order of magnitude greater than that of the probe. As such this can make the tail end of the conjugate spectrum harder to visualise. In the lower half of figure 4.5 the colour bar scales are set to the same level and so the lower end of the conjugate spectrum is more easily visible. In this formalisation, the cross-kerr effect on the probe field caused by the presence of the pump has been ignored, as has the pump's intensity profile. The effect of these assumptions is discussed further in section 4.4.3.

This difference between probe and conjugate gain values would appear to indicate that no squeezing should be visible as a result of this process. For amplitude correlations the power of each detected beam should be similar, such that the common mode rejection can be maximised and the quantum correlations seen. In a case where the conjugate is a factor of 10 brighter than the probe, nothing would be seen. To corroborate this picture, an experiment was performed across the accessible region of the parameter space, as described further in section 4.4.

To be precise, the act of adjusting δ has two effects. Firstly it changes the k-vector of the probe directly, by altering its frequency. Secondly it changes the effective refractive index of the medium as seen by the probe. The first effect can be

calculated simply from the relationship between k vector and frequency

$$k = \frac{2\pi}{\lambda} = \frac{\omega}{c}, \tag{4.17}$$

which even over a range of 10 γ results only in a fractional change in k of order 10^{-7}. In contrast, the second effect arises from the modification to k_0 to $n_0 k_0$ as a result of the refractive index of the medium. The highest value taken for $\Re(\chi_{pp})$ is around 10^{-3} giving a change to refractive index of ϵ where

$$n = \sqrt{1 + 10^{-3}} \approx 1 + \epsilon \tag{4.18}$$

$$\approx 1 + \frac{1}{2} \times 10^{-3} = 1 + 5 \times 10^{-4}\,, \tag{4.19}$$

giving

$$\epsilon = 5 \times 10^{-4} \tag{4.20}$$

As the change to k caused by the adjustment to refractive index is three orders of magnitude greater than that introduced directly, it is safe to neglect the other effect.

4.3.2 Fitted Parameters

The remainder of this section discusses the effects of the values of the fitted variables on the calculation results and reinforces the validity of their estimations.

Ground State Decoherence Rate

The ground state decoherence rate γ_c describes the dephasing between the ground states. Decreasing this value results in far higher levels of gain across the parameter space. Figure 4.6 shows $\Im(\chi_{pp})$, the absorption of the probe, plotted against δ for $\gamma_c = 0.2\gamma$ (blue, and the fitted real value), $\gamma_c = 0.02\gamma$ (red), and $\gamma_c = 0.002\gamma$ (green).

For a low enough decoherence rate a dip to the right of $\delta = 0$ is formed, displaying where the absorption visibly falls. This is the EIT window that starts to form in cases with low enough decoherence. As mentioned, this behaviour is not typically visible under experimental conditions, which are more accurately described by the blue line.

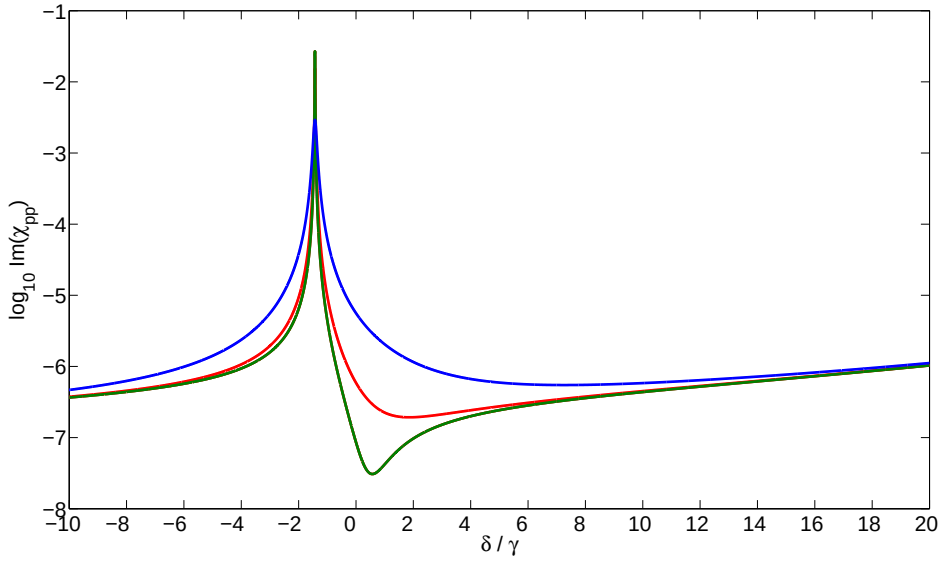

Figure 4.6: Shows the modelled absorption of the probe beam ($\Im(\chi_{pp})$) as δ changes for γ_c equal to 0.2γ (blue), 0.02γ (red) and 0.002γ (green). The increasing dip to the right of $\delta = 0$ is the transparency window relating to the EIT condition.

Rabi Frequency

The Rabi frequency for the pump Ω affects the overall gain levels achieved as well as the location of the 2-photon resonance. A higher value for Ω_0 increases the extent of the light shift, as described in section 4.3.1, placing the resonance further to the blue side of $\delta = 0$ and increases the gain seen in the procedure. This can be seeen in figure 4.7 which shows the location of the resonance for $\Omega = 40, 60, 80\gamma$.

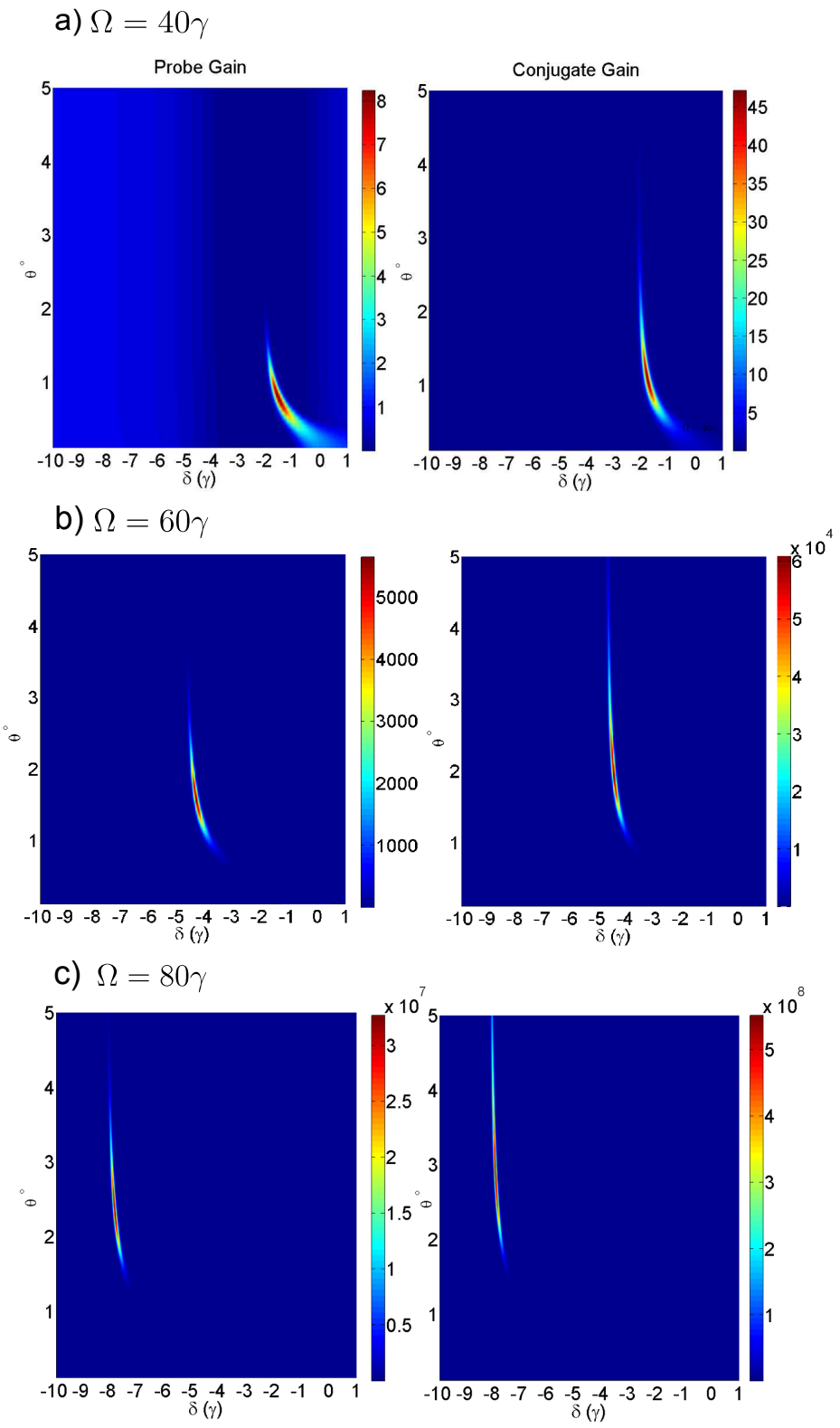

Figure 4.7: Shows the modelled gain of both the probe and conjugate over a range of values of δ and θ for three values of Ω. a) Shows the result for $\Omega = 40\gamma$, b) shows the results for $\Omega = 60\gamma$ and c) shows the results for $\Omega = 80\gamma$. In the final calculation, the value of $\Omega = 60$ was selected.

Refractive Index for the Pump

Another factor unconsidered by the theory is the refractive index shift of the pump. This causes an adjustment to the k vector and as such to the extent of the phase mismatch, adjusting it to the form

$$\Delta \mathbf{k}_z = 2n_0\mathbf{k}_0 - \mathbf{k}_p - \mathbf{k}_c. \tag{4.21}$$

This factor might not seem especially important due to the fact that in the presence of the strong pump, the majority of atoms reside in the $f = 3$ state (estimated at 95% after a time of 10×10^{-5} s[82]), due to the coupling of the $f = 2 \rightarrow f = 3$ transition being closer to resonance. Meanwhile the effect of the refractive index is greater on those in the $f = 2$ state for the same reason. That is to say that the refractive index of the medium as seen by the pump is in proportion to the percentage of the atomic population in the state that responds to it most strongly, but as a result of that strong response, the corresponding percentage is relatively low, giving a low overall effect.

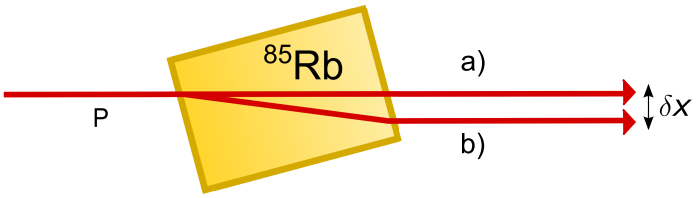

Figure 4.8: Shows the experimental setup for attempting to measure the refractive index, in which the cell is rotated with respect to the incoming beam by an amount ranging from $0 - 22°$. An off-resonant pump beam, designated a), experiences a shift in position from a resonant pump, designated b) that is detectable and can be related to the change in index. δx is the extent of the shift.

An attempt to measure the extent of n_0 was performed by angling the cell with respect to the pump. In this arrangement, any change in refractive index from an interaction with the medium due to the 4WM process can be seen by looking for a

change in position of the emitted beam when brought into resonance from the off resonant case. This is shown schematically in figure 4.8. Note the shift in trajectory away from the normal is as the expected value for n_0 should be < 1.

Using the equipment available, the maximum relative angle achievable between cell and the pump field was around 22° and maximum δx detectable on the beam profiler approximately 5 µm. This corresponds to a minimum measurable index, $n = 1 - \epsilon$ with an ϵ value of 5×10^{-4}. No visible shift in position was seen, lending credence to the belief that the shift is less than this value. Fitting the experimental data to the prediction gave an estimated value for ϵ of $\epsilon = 6.5 \times 10^{-6}$ and a calculation based on the population differences suggested a value $\epsilon = 1.6 \times 10^{-5}$, both of which fall safely below the experimentally derived upper limit.

4.4 Mapping the Feature Experimentally

This section describes the experiment performed in order to validate the results shown in figure 4.5. The results of the experiment also served to provide best-fit values for the simulation with respect to the experimental parameters achievable.

4.4.1 Experimental Setup

In order to verify the predicted behaviour of this system, an experiment was performed as demonstrated in figure 4.9 [3] in which a bright 750 mW pump beam, with a waist of 1 mm at 794.974 nm drives the 4WM process in a cell of heated ^{85}Rb, while a weak seed beam (waist = 0.5 mm, power = 120 µW) is shifted in frequency by a factor of δ ($\delta \sim 3$ GHz) using an AOM. This seed is then injected into the same ^{85}Rb cell at a small angle θ in order to generate the bright twin probe/conjugate beams.

The gains on the probe/conjugate (G_p/G_c) are measured by splitting the seed in

[3] The general arrangement to generate the 4WM is as described in chapter 3.

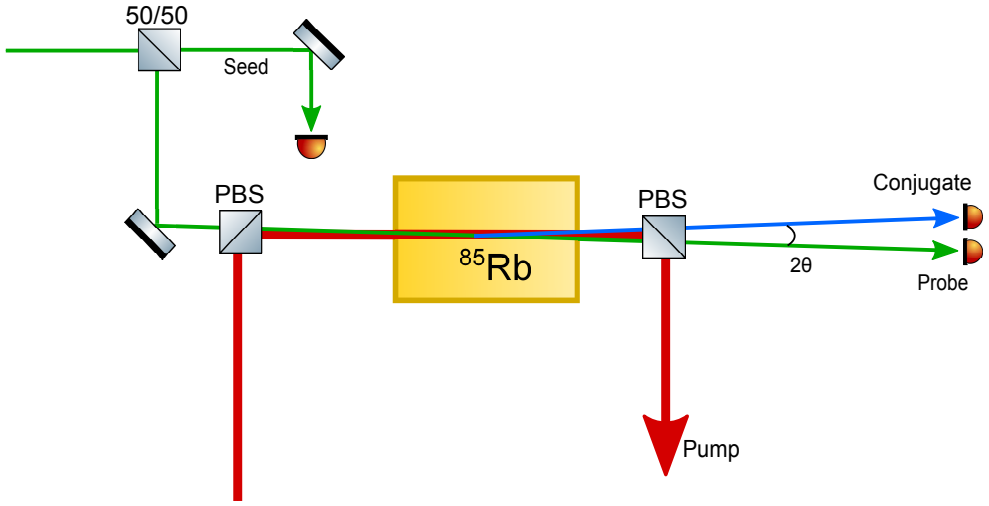

Figure 4.9: Shows the experimental setup for mapping the gain on the probe/conjugate beams as a function of the input angle θ and two-photon detuning δ. The angle is adjusted via a pair of mirrors on the input, one for lateral adjustment, one for angular, and the gains are measured as a function of the powers measured on the output probe and conjugate fields with respect to the input seed power.

half on a 50/50 beam splitter and measuring the power of the emitted pair (Pr'/Pc for the probe/conjugate) compared to the power being injected (Pr) such that

$$G_p = \frac{P_p}{P_{p'}}, \tag{4.22a}$$

$$G_c = \frac{P_p}{P_c}. \tag{4.22b}$$

The single-photon detuning Δ_1 is measured by referencing the frequency of the pump that produces the maximum gain to a separate Rb spectroscopy cell with the result that $\Delta_1 = 140\gamma$, and this is then held stable via a third cell used as a dichroic atomic vapour laser lock (DAVLL) as described in [89][90]. By adjusting the frequency of the AOM driver, δ is changed in units of 2 MHz while the angle between seed and pump is changed by adjusting a pair of input mirrors in the seed system. The powers are derived from individual calibrations of each diode converting

between input power and output voltage. Values for θ are found by measuring the distance between the centres of the probe/conjugate beams in the far field, d, and the distance from the centre of the cell to the point of measurement, D. From these values $2\theta = \tan^{-1} d/D$.

4.4.2 Field Overlap

When adjusting the input angle of the probe it is important to ensure that the overlap between the pump and the probe inside the cell is maintained across each run. Ideally the probe should rotate around a fixed point in the centre of the cell, with a 100 % overlap with the pump. Initially it was assumed that this could be achieved by finalising the adjustment with respect to maximising the output gain.

The change in angle was produced by two mirrors, and under the assumption that with an arbitrary lateral position selected by the first, the position of the second mirror that served to maximise the output gain would be that which optimised the internal overlap. However, this proved to be incorrect. When tested in this manner, it was found that results taken after initialising the setup at a higher value of δ were inconsistent with those achieved when δ took a lower value during the setup process.

The source of the error can be understood by considering that the plotted form of the χs always assumed a constant and well-defined pump power, thus a constant Rabi frequency and a constant light shift. In reality the pump has a Gaussian intensity distribution and in the weaker regions the light shift is reduced, bringing the position of the two-photon resonance closer towards $\delta = 0$. The behaviour should therefore emulate the calculation most accurately when the probe and pump intersect in the region of maximum pump intensity.

The shift in the location of the resonance when the probe intersects a weaker region of the pump has the effect that if the value of δ is greater, an interaction with a weaker pump field will actually generate a greater gain on the output. As such

maximising gain on the output while the $\delta \approx 0$ is likely to result in an off-centre overlap of the fields within the cell.

This effect could be seen experimentally when imaging the centre of the cell onto a beam profiler, where indeed when the maximum gain was seen for higher δ values, the field intersection was off-centre. As such, maintaining a centred probe beam position and consistent operational parameters was not achievable purely by monitoring the gain on the output. Instead the approach used was first to maximise the gain for some arbitrary angle of input at a relatively low δ, where the phase matching is met by a centred intersection in the medium. Between each run the vacuum chamber/cell was physically replaced with a marker that could reliably be placed in the same position corresponding to the centre of the cell. This marker would be placed in the path of the probe and allow for reliable realignment. In this manner the probe crossing could be kept at a central point in the pump, despite in some situations being capable of generating higher gain by operating in a weaker pump region.

4.4.3 Results and Analysis

These gains, when mapped, produced the results shown in 4.10. Both the calculation and the experiment demonstrate a notable change in the position of the gain peak with increasing angle, with the corresponding δ getting closer to the absorption feature and the peak intensity increasing. However in the experiment the value of θ at which the maximum achievable gain is reached is considerably lower, 0.6° instead of 1.5-2°.

This can be explained by noting again that the calculation neglects an additional consequence of the cross-Kerr effect. It assumes a constant Rabi frequency and intensity across the entire region of the interaction, and thus a constant refractive index. In reality, the Gaussian distribution of the pump power causes the extent of

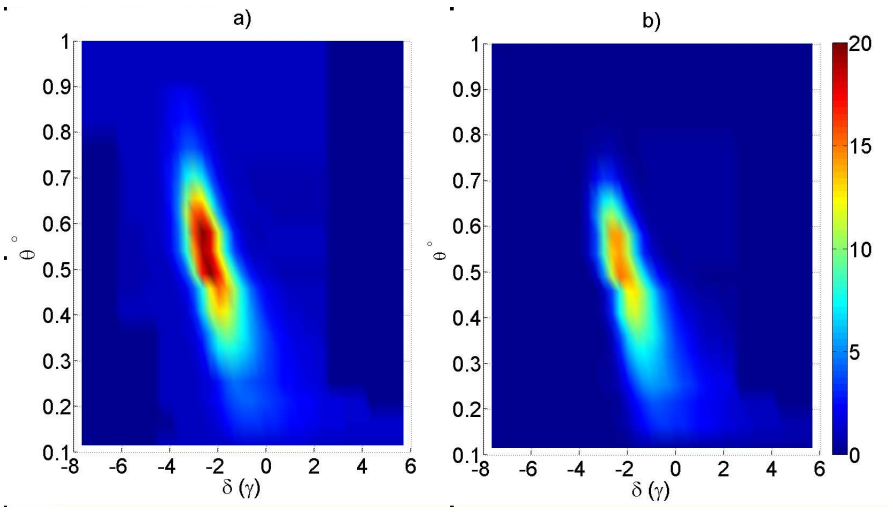

Figure 4.10: Shows the experimental results for the gain mapping. Each vertex is a data point, interpolation performed by Mat Lab. a) shows the conjugate, b) shows the probe. Data ranges and colour bar limits have both been significantly altered from calculated plots in previous section.

the cross-Kerr effect to vary across the medium. This is a caused not only by the shift in pump intensity but simultaneously a change induced in the light shift and another changing contribution to $\Re(\chi_{pp})$. The change in pump intensity results in a change in both the maximum value and centroid position of $\Im\chi_{pp}$ depending on where the probe is along the spatial profile of the pump field.

The probe therefore starts to encompass a range of k values along the cell resulting in a spatial spread that causes a visible blooming effect at the output. This becomes more intense as the angle is increased resulting in considerably less emission due to a large reduction in correct phase matching. The conjugate suffers less from this effect directly, but clearly suffers to some extent due to generally reduced conjugate gain. At large enough angles the extent of the blooming caused by this varying refractive index effect causes a spread in emission angle larger than the original angle of input.

A second reason for the discrepancy is the introduction of a residual Doppler effect. For two co-propagating beams any Doppler effect will approximately cancel

out however as the probe and pump beams have an angle between them, the atomic resonance will broaden in accordance with the velocity spread of the vapour. Assuming a temperature T = 120 °C, and given an atomic mass for ^{85}Rb m = 1.44×10^{-25} kg the average atomic speed can be calculated from

$$\begin{aligned} \left\langle \frac{1}{2} m v_x^2 \right\rangle &= \frac{1}{2} k_B T, \\ \sqrt{\langle v_x^2 \rangle} &= \sqrt{\frac{k_B T}{m}}, \\ \sqrt{\langle v_x^2 \rangle} &= 274\,\mathrm{m\,s^{-1}}, \end{aligned} \tag{4.23}$$

where k_B is Boltzmann's constant, $k_B = 1.4 \times 10^{-24}\,\mathrm{m^2\,kg\,s^{-2}\,K^{-1}}$. The standard Doppler frequency shift is defined as

$$\omega' = \omega \left(1 + \frac{v}{c}\right), \tag{4.24}$$

while the residual Doppler shift is the discrepancy between the broadening on the two frequencies. For an input angle of 1° (the maximum used in the experiment) the broadening is already around 12 MHz, which is greater than the expected width of the feature and goes some way towards explaining the large decrease in gain with respect to the prediction.

Both the lensing caused by the pump and the residual Doppler broadening are factors that cause a greater effect as θ increases, explaining why at larger angles the experimental data compares less favourably to the calculated plots. Figure 4.11 shows both the prediction and data up to $\theta = 0.6$ with a limitation on the calculated gain set just in excess of that achieved experimentally. At these low angles, where the experimental factors are largely unperturbed by factors not included in the simulation, it can be seen that the level of congruence is significantly greater.

It is here, in this low angle region, that the fitting was performed to generate

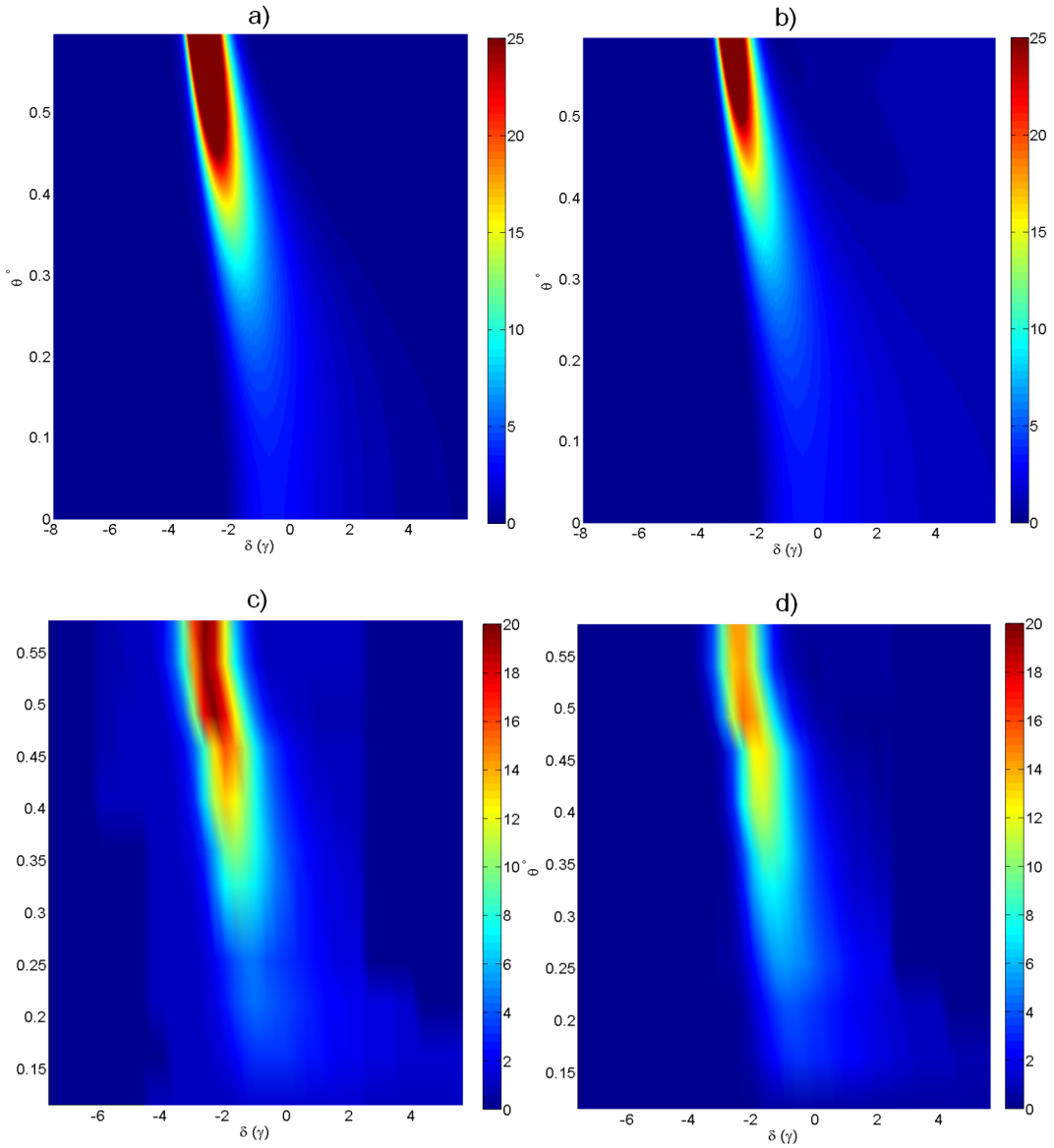

Figure 4.11: Shows both the calculated and experimental results for the gain mapping for θ ranging from 0 to 0.6 degrees. a) and b) show the calculated results for the probe and conjugate respectively while c) and d) are the experimental results for the same.

the parameter values of $N = 2.8 \times 10^{18}\,\mathrm{m}^{-3}$, $\gamma_c = 0.2\gamma$ and $\Omega = 2\pi \times 306\,\mathrm{MHz}$ used previously throughout this chapter.

4.5 Conclusion

The modelled form of the gain predicts an exceptionally high conjugate gain region for an input seed slightly detuned from the two-photon resonance, when adjusted geometrically to satisfy the phase-matching condition. However, this situation is clearly entirely unsuitable for obtaining good squeezing measurements, as evidenced by the enormous discrepancy between probe and conjugate output gain. In fact this setup of 'ideal' 4WM that maximises the efficiency of the process would clearly never satisfy the desired requirements for balanced output fields.

The experimental tests show limitations on the process as a result of unconsidered aspects such as the residual Doppler broadening of the lines and self-induced changes in refractive index. In reality, experiments performed utilising this nonlinear feature in the vapour have to operate within a narrow window of the gain parameter space with an input angle of $\sim 0.2 - 0.3^\circ$ and $\delta \approx 0$ in order to measure high levels of 4WM and gain on both channels.

In this arrangement the value of Δk_z is approximately 0 once more and the motivation for retaining an angle of injection is the small but important index of refraction of the pump. This causes conical propagation of the photon pairs and as such necessitates an angle when introducing a seed field. Operating in this scenario also presents additional advantages for the experimentalist. Requiring an input angle makes for simple separation of the beams at the output and operational gains of $4 - 5$, here at the very tail end of the feature, are well within operational parameters of standard equipment. Some low level of absorption on the probe can also be beneficial as a way to more equally balance the output powers of the beams that

would otherwise have a power difference equal to the power of the input seed.

Tests performed in this $\delta = 0$ region, with a setup almost identical to that described here, have shown that the feature can generate levels of amplitude correlation squeezing up to -8 dB and at frequencies as low as 2.5 kHz on a single pass through a 12.5 mm cell[91].

Now that the usage of this heated ^{85}Rb vapour as a valid squeezing source has been suitably explained, the next chapter will utilise the source to provide the multi-spatial mode squeezed light desired for the improvement of the imaging technique.

Chapter 5

Multi-Spatial-Mode Squeezing on a Single Beam

The majority of the work undertaken for this thesis was towards the generation of a source of MSM squeezed light as described in section 1.5 using the 4WM process described in section 2.2, with the goal being to produce a single beam of light with reduced amplitude fluctuations across many transverse spatial modes. This would be done by combining a bright beam with a source of MSM squeezed vacuum, using a 99/1 beam splitter, such that 1% of the power of the bright beam is combined with 99% of the squeezed vacuum.

This chapter will detail completely the methods and arrangements used to achieve this outcome, as well as describe the extent to which these goals have been attained. The gist of the process is that two-mode squeezed vacuum[1] is generated, the twin fields are combined, generating a single-mode squeezed state (SMSS) and the noise reduction is measured via homodyne detection. The multi-mode nature is investigated by using LOs with a range of transverse spatial modes.

Results are then given both for the amplitude correlations detected across gener-

[1]See section 1.3 for the definition of 'two-mode' squeezed, as used here.

ated twin beams from the 4WM cell and the homodyne detection of the SMSS as measured using LOs with a variety of spatial profiles.

5.1 Generating Multi-Spatial-Mode Squeezed Light

This section is concerned with the preparation of the single-mode MSM squeezed vacuum field to be interrogated in the homodyne detector. It details how the required states are prepared experimentally, and some of the finer details involved in successfully engineering the state.

5.1.1 Generating Vacuum Fields

The bulk of the apparatus is as described in chapter 3 and as previously used in chapter 4. The main difference this time is that when producing the vacuum fields, no seed beam is applied to the cell. Upon each iteration of the 4WM transition across the cell, a pair of probe and conjugate photons are emitted into the cone of emission centred on the pump. These emissions form the TMSS vacuum fields.

5.1.2 Combining Vacuum Fields

The goal however is not two-mode squeezed vacuum, where the correlations are spatially separated, but single-mode, with the single field showing reduced fluctuations. The transformation from one form to the other can be performed with a beam splitter, as follows.

If twin vacuum fields are combined on a 50/50 beam splitter (with $t = r = \frac{1}{\sqrt{2}}$) then the fields at the output ports $\hat{a}_3$ and $\hat{a}_4$ in terms of the input fields $\hat{a}_1$ and $\hat{a}_2$

are equal to

$$\hat{a}_3 = \frac{1}{\sqrt{2}}(\hat{a}_2 + \hat{a}_1), \tag{5.1a}$$

$$\hat{a}_4 = \frac{1}{\sqrt{2}}(\hat{a}_2 - \hat{a}_1). \tag{5.1b}$$

Note the similarity between the emitted fields and the joint quadratures of the two-mode system described in equation 1.20. The result, as depicted in figure 5.1 is that the two output fields are each single-mode quadrature-squeezed vacuum fields with the squeezed quadrature of $\hat{a}_3$ being the conjugate of the quadrature squeezed in $\hat{a}_4$.

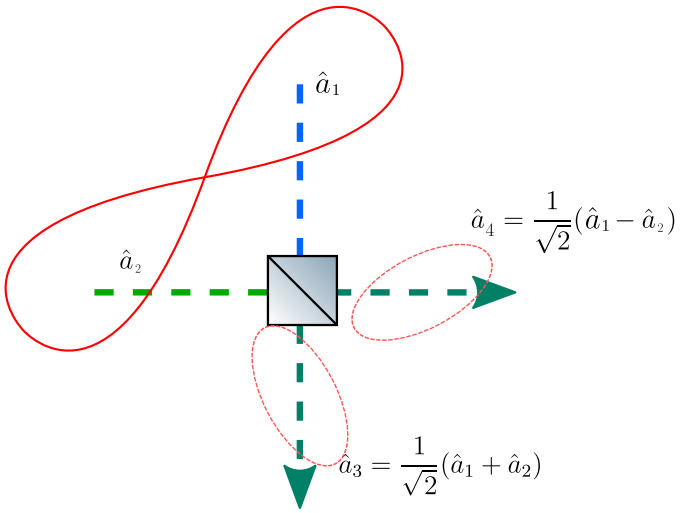

Figure 5.1: Shows the effect of combining twin vacuum fields on a beam splitter, resulting in emitted beams that are single-mode squeezed.

The phase of the pump and the length of the cell define precisely which quadratures are squeezed in terms of $\hat{X}$ and $\hat{Y}$, but the result is largely unimportant as all quadrature uncertainties of the selected field will be viewed during the detection. From here, one of the output fields can be ignored while the other, described using

the outputs from the beam splitter as

$$\hat{E}_S = \hat{a}_1 e^{-i(\omega_1 t + \phi_{S,1})} + \hat{a}_2 e^{-i(\omega_2 t + \phi_{S,2})}, \tag{5.2}$$

is taken as the SMSS field to be measured.

5.1.3 Bichromatic Homodyne Detection

In order to detect the level of squeezing present in the vacuum signal, homodyne detection is used, as covered in more detail in section 1.4.2. The key difference is that in this case the signal to be measured is contains two frequencies with the amplitude correlations occurring across the probe and conjugate frequency elements. The analogy can again be made to the frequency picture. Emerging from the cell are two fields, $\hat{a}_1$ and $\hat{a}_2$, each composed of a mixture of probe and conjugate photons such that every probe photon in $\hat{a}_1$ has a corresponding conjugate photon in $\hat{a}_2$ and vice versa. This results in a TMSS in which correlations are present between frequency components distanced from the central pump frequency by around 3 GHz. This situation is pictured in part a) of figure 5.2. The frequency correlations are enforced by the parametric nature of the transition and occur across a bandwidth of around 30 MHz, as seen in chapter 4. Combining $\hat{a}_1$ and $\hat{a}_2$ onto a beam splitter results in a pair of emitted fields $\hat{a}_3$ and $\hat{a}_4$. These feature self-contained correlations between their two frequency components, as shown in part b) of figure 5.2. $\hat{a}_3$ and $\hat{a}_4$ are each SMSS identical to the one demonstrated in figure 1.6 but with correlations spanning 6 GHz as opposed to just a few MHz as was the case previously.

The case of detecting correlations across two distinct frequencies is typically achieved by applying a bright LO with a frequency centred between the two components. This situation is again identical to that in fig. 1.6 and is shown here in fig 5.2 part c). Using a centred LO with a frequency of $\omega_{LO} = (\omega_+ + \omega_-)/2$ the variance on

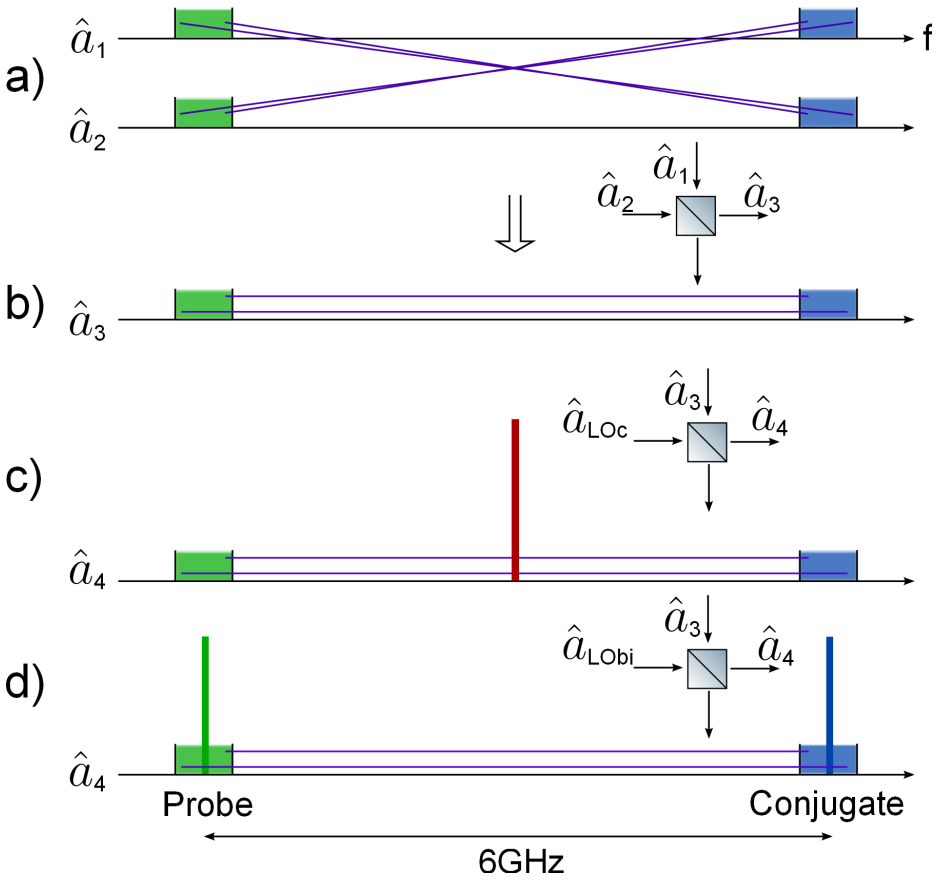

Figure 5.2: Shows the form of the frequency correlations. Frequency runs along the base axis, the coloured bins indicate the frequency ranges occupied by the emitted 4WM photons at the probe (green) and conjugate (blue) frequencies and the purple lines indicate correlations between different frequency elements. a) The correlations are present across the two output vacuum fields between the probe elements of field $\hat{a}_1$ and the conjugate photons in field $\hat{a}_2$ and vice versa. b) The frequency correlations in the emitted field $\hat{a}_3$, produced by combining fields $\hat{a}_1$ and $\hat{a}_2$ on a beam-splitter. Here the correlations are contained within a single field, however they still occur across the two frequency elements. The other beam splitter output would appear identical and is not pictured here. c) The system when measured with a centred LO features correlations detectable at a frequency of 3 GHz. The taller lines in c) and d) indicate bright LO fields. d) The same system measured with a bichromatic LO with each element centred on its respective frequency range and able to detect the correlations at a frequency of the order of MHz

the intensity when measured with a balanced detector as before is equal to

$$\langle(\Delta i_-)^2\rangle \propto 4E_{LO}^2(\cos^2\phi\Delta E_{S,X}^2 + \sin^2\phi\Delta E_{S,Y}^2). \tag{5.3}$$

The result, as expected, gives an output proportional to the noise on the squeezed field for a given quadrature angle ϕ and amplified by the strength of the LO. In practice however, detection with this setup would not achieve the desired results. The reason for this is that the squeezing information is centred at the beat frequency $\omega_{sq} = (\omega_+ - \omega_-)/2$. In this case ω_+ and ω_- are the probe and conjugate, and hence separated by 6 GHz, meaning $\omega_{sq} = 3$ GHz. This is outside the effective measurement range of the spectrum analyser, due to the response time of the photo-diodes. At frequencies above the order of 10 MHz the dominant noise term in our detectors is the electronic noise floor as described in section 5.2.5 which rises above the photonic SNL and makes the detection of any squeezing at this range impossible.

Methods for measuring squeezing correlated across separate frequencies more effectively have been theoretically proposed[92] and performed [93] before, but not without the use of cavities to separate the squeezed sidebands which here would not serve to maintain the MSM nature of the squeezing. The solution demonstrated here is the use of a two-colour (bichromatic) LO, which should serve to detect arbitrarily separated correlations without the need for spectral filtering, as predicted by Marino in 2007 [94].

Here the LO field is comprised of two frequencies and takes the form

$$E_{LO} = \mathcal{E}_1\cos(\omega_1 + \phi_{LO,1}) + \mathcal{E}_2\cos(\omega_2 + \phi_{LO,2}), \tag{5.4}$$

where ω_1 and ω_2 correspond to the two frequencies that are correlated in the squeezed vacuum signal. This is shown in the final image of fig 5.2 where the two frequencies of the bichromatic LO are selected to be centred within their respective component

of the vacuum field. In practice the source of the bichromatic LO is the same as the source of the signal. A second pump beam is injected into the ^{85}Rb cell, which in this case is seeded to produce a pair of beams at the desired probe/conjugate frequencies. These bright output fields are then also mixed on a beam splitter to generate a bright bichromatic field to be used as the LO in the bichromatic homodyne detection.

The optical setup for the experiment past the cell is shown in figure 5.3. After the cell, solid lines represent the path of both bright fields to form the LO and vacuum signal fields. Where they separate, the signal field is represented by a dashed line.

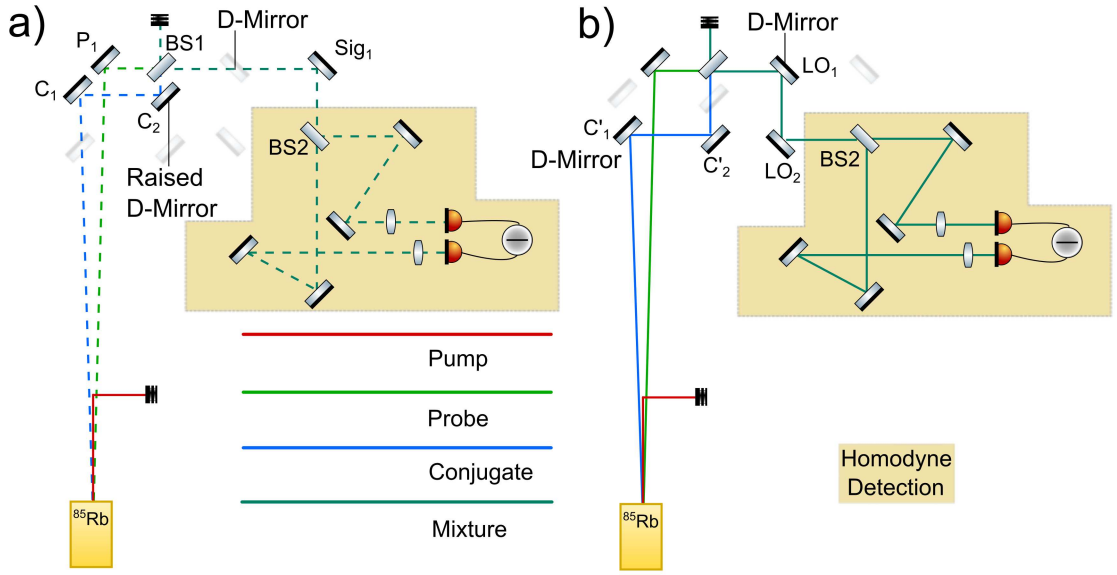

Figure 5.3: Shows the optical setup in place after the cell for recombining the various fields. a) shows the paths taken by the two components of the LO while b) shows the paths taken for the two elements of the signal field. Note that in reality the signal fields are both bichromatic from their point of origin, the different colours indicates pre/post combination. Both arrangements exist simultaneously on two vertical levels. The signal fields pass above the LO fields, which are picked off by the D-Mirrors

To form the homodyne detector the bichromatic LO and squeezed vacuum field are combined on a second 50/50 beam splitter. The two output fields can then be sent onto the balanced detector, as before, and the noise on the difference current

measured on the spectrum analyser.

The variance on the balanced photocurrent can be described as [94]

$$\langle (i_-)^2 \rangle \propto 4E_{LO} \left(\cos^2 \frac{\phi_{LO,1} - \phi_{s,1} + \phi_{LO,2} - \phi_{s,2}}{2} + \sin^2 \frac{\phi_{LO,1} - \phi_{s,1} + \phi_{LO,2} - \phi_{s,2}}{2} \right). \tag{5.5}$$

An assumed picture of this form of LO might suppose that in order to measure the maximum extent of the squeezing ellipse, it would be required that both the composite phases, $\phi_{LO,1}$ and $\phi_{LO,2}$ would simultaneously have to be manipulated to measure correctly the minimum uncertainty angle of their respective component of the squeezed vacuum signal. However here we see quite the opposite. In fact the adjustment of $\phi_{LO,1}$, $\phi_{LO,2}$, $\phi_{s,1}$ or $\phi_{s,2}$ [2] still produces a full picture of the squeezing ellipse. As such in the experimental setup, where the scanning is being done by a piezo-electric transducer modulating the position of a mirror, the selection of mirror is almost arbitrary. Applying the modulation to the LO pump field will serve to scan the phase of the emitted LO conjugate component, giving the full picture. Modulation of the signal pump will scan the phase of both vacuum signal components. In fact the sole field phase adjustment that does not scan the entirety of the feature is that of the applied LO seed field. This is because though it acts to rotate the phase angle of both the LO field outputs, they each rotate in reverse directions[3], carrying no net effect on the ellipse angle under interrogation. In practice the scanning is performed on the mirror directing the mixed signal into the homodyne detection beam splitter.

[2] As the vacuum fields contain components at each frequency at all points, the adjustment of phase $\phi_{s,1}$ or $\phi_{s,2}$ individually is an impossibility.

[3] For an intuitive explanation of this recall from section 1.3 that the phase sum is also a squeezed quantity in a two-mode squeezed state.

5.1.4 Mode-matching Vacuum Fields

As each vacuum field contains two frequency components, when they reach the beam splitter there will be a relative phase between the two probe fields and another between the two conjugates. The difference between these two phases has an important effect on the degree to which the state is successfully transformed from a TMSS to a SMSS.

To show the effect of this phase, we take the ideal case of an emitted TMSS with perfect squeezing $\langle \Delta \hat{X}_- \rangle = \langle \Delta \hat{Y}_+ \rangle = 0$. Described completely in terms of quadratures, fluctuations on the twin vacuum signal fields emitted from the cell can be written as

$$\hat{E}^a = (\hat{X}_p^a + i\hat{Y}_p^a) + e^{i\phi_1}(\hat{X}_c^a + i\hat{Y}_c^a), \tag{5.6a}$$

$$\hat{E}^b = (\hat{X}_p^b + i\hat{Y}_p^b) + e^{i\phi_1'}(\hat{X}_c^b + i\hat{Y}_c^b). \tag{5.6b}$$

Of interest is the quantity $\Delta\phi_1 = \phi_1 - \phi_1'$, the difference between the relative phase of the conjugate/probe components of E^a with that of E^b. This can be propagated in a simpler manner by setting $\phi_1 \to 0$ and $\phi_1' \to \phi_1$.

In the case of ideal squeezing the quadrature fluctuations on E^a and E^b are perfectly correlated such that

$$\Delta(\hat{X}_p^a - \hat{X}_c^b) = 0, \tag{5.7}$$

$$\Delta(\hat{Y}_p^a + \hat{Y}_c^b) = 0, \tag{5.8}$$

allowing for the conversions to be made

$$\hat{X}_p^a = \hat{X}_c^b, \tag{5.9a}$$

$$\hat{X}_p^b = \hat{X}_c^a, \tag{5.9b}$$

$$\hat{Y}_p^a = -\hat{Y}_c^b, \tag{5.9c}$$

$$\hat{Y}_p^b = -\hat{Y}_c^a, \tag{5.9d}$$

giving

$$\hat{E}^a = (\hat{X}_p^a + i\hat{Y}_p^a) + (\hat{X}_p^b - i\hat{Y}_p^b), \tag{5.10a}$$

$$\hat{E}^b = (\hat{X}_p^b + i\hat{Y}_p^b) + e^{i\phi_1}(\hat{X}_p^a - i\hat{Y}_p^a). \tag{5.10b}$$

When $\hat{E}^a$ and $\hat{E}^b$ are combined on a beam splitter two output fields are produced, as in figure 5.1, one of which, E^d can be ignored and the other $E^c = E^a + e^{i\phi_2}E^b$, written in full as

$$\begin{aligned}\hat{E}^c = &(\hat{X}_p^a + i\hat{Y}_p^a) + (\hat{X}_p^b - \hat{Y}_p^b) \\ &+ e^{i\phi_2}((\hat{X}_p^b + i\hat{Y}_p^b) + e^{i\phi_1}(\hat{X}_p^a - i\hat{Y}_p^a)).\end{aligned} \tag{5.11}$$

We also consider the idealised case where a centred LO at a single frequency successfully measures the maximum squeezing $\Re(E^{LO}e^{i\phi_3}E^c) = 0$. Mixing E^c with E^{LO} and including their relative phase ϕ_3 gives

$$\begin{aligned}E^{LO}e^{i\phi_3}\hat{E}^c = E^{LO}[&e^{i\phi_3}(\hat{X}_p^a + i\hat{Y}_p^a + \hat{X}_p^b - \hat{Y}_p^b) \\ &+ e^{i(\phi_2+\phi_3)}(\hat{X}_p^b + i\hat{Y}_p^b) + e^{i(\phi_1+\phi_2+\phi_3)}(\hat{X}_p^a - i\hat{Y}_p^a)].\end{aligned} \tag{5.12}$$

The phases can be relabelled such that

$$\phi_\alpha = \phi_3, \qquad \phi_\gamma = \phi_2 + \phi_3, \qquad \phi_\Omega = \phi_1 + \phi_2 + \phi_3, \tag{5.13}$$

and the form can be rewritten in terms of real and imaginary parts

$$\begin{aligned} E^{LO}[&\hat{X}_p^a(\cos\phi_\alpha + \cos\phi_\Omega + i(\sin\phi_\alpha + \sin\phi_\Omega)) \\ &+\hat{X}_p^b(\cos\phi_\alpha + \cos\phi_\gamma + i(\sin\phi_\alpha + \sin\phi_\gamma)) \\ &+\hat{Y}_p^a(\sin\phi_\Omega - \sin\phi_\alpha + i(\cos\phi_\alpha - \cos\phi_\Omega)) \\ &+\hat{Y}_p^a(\sin\phi_\alpha - \sin\phi_\gamma + i(\cos\phi_\gamma - \cos\phi_\alpha))]. \end{aligned} \tag{5.14}$$

The origin and combination of these phase terms is illustrated in figure 5.4.

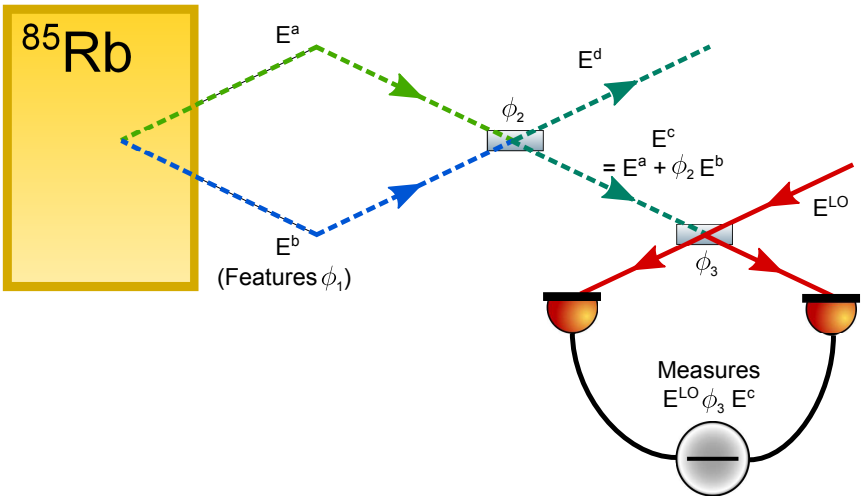

Figure 5.4: Shows the origin of the various phase terms included in the calculations presented in section 5.1.4. ϕ_1 covers the difference in phase between probe and conjugate elements within one output field with respect to the other. ϕ_2 is the phase introduced between E^a and E^b when mixed on the first beam splitter. ϕ_3 is the relative phase between E^{LO} and E^c when mixed on the second beam splitter.

The minimum amount of noise on the homodyne detection output is achieved when $\Delta(\hat{E}^{LO}\hat{E}^c = 0)$. The homodyne detector views only the real elements, so in

order for the real part of the above to be equal to zero, the following conditions must all be met

$$\begin{aligned} \cos\phi_\alpha &= -\cos\phi_\Omega, & \cos\phi_\alpha &= -\cos\phi_\gamma, \\ \sin\phi_\alpha &= \sin\phi_\Omega, & \sin\phi_\alpha &= \sin\phi_\gamma. \end{aligned} \tag{5.15}$$

This is only true when

$$\phi_\alpha = \pi - \phi_\Omega = \pi - \phi_\gamma. \tag{5.16}$$

Returning the phases to the original form,

$$\phi_3 = \pi - (\phi_1 + \phi_2 + \phi_3) = \pi - (\phi_2 + \phi_3), \tag{5.17}$$

thus for ideal squeezing transmission it is required that $\phi_1 = 0$, i.e. $\Delta\phi_1 = 0$, that is to say that the probe/conjugate elements of each vacuum field should have an identical relative phase at the point where they are combined. This appears to also define a strict phase requirement that $2\phi_3 + \phi_2 = \pi$ in order to view squeezing, however this is actually only the phase condition required to show the maximum squeezing. In reality squeezing will be seen at this and surrounding phases with the condition only satisfied completely at the point where the noise signal is at a minima.

To ensure that $\phi_1 = 0$ experimentally, we turn to interferometry. In an interferometer with a single frequency, the fields interfere at a beam splitter and the extent of mode-matching can be optimised by measuring the maximum and minimum output powers from one port when the relative phase is cycled from $0 - 2\pi$. This contrast can be calculated as

$$C = \frac{I_{max} - I_{min}}{I_{max} + I_{min}}. \tag{5.18}$$

$\Delta\phi_1 = 0$ is satisfied when the contrast from the mixing of the bichromatic fields is a maximum. If two frequencies are present in the fields, the output splitting of each colour is independent as there is no cross-interference. To maximise the total contrast it is necessary to find a path length setup which corresponds to the two frequencies arriving at the interferometer with the same relative phase, i.e. when $\Delta\phi_1 = 0$.

The length scale for ϕ_1 is related to the length of the beat between the two elements of the signal. The difference in frequency between the two field components is 6 GHz, giving a time scale for the beat of 1.67×10^{-10} s which corresponds to a spacing of 5 cm. The phase ϕ_1 cycles over this distance and so this is the scale on which the path lengths must be equalised.

In order to measure the contrast experimentally, bright bichromatic fields must be introduced that stand in for the vacuum field. The optical setup to achieve this is shown in figure 5.5.

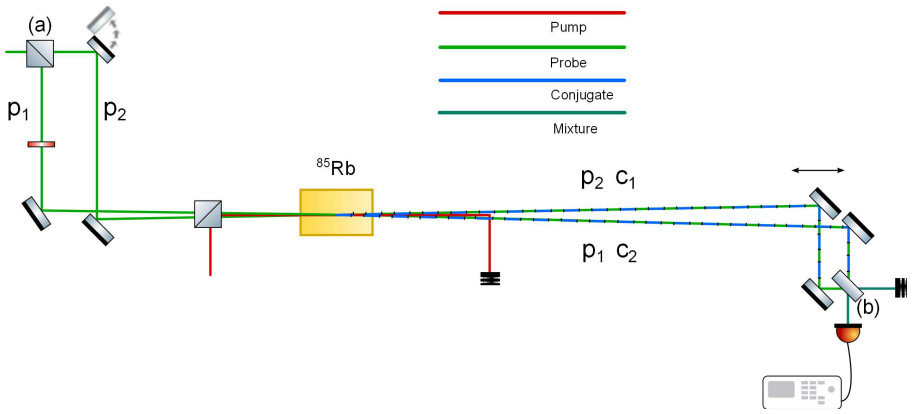

Figure 5.5: Shows the optical setup in place before and after the cell for generating a white light interferometer. The form of the interferometer is equivalent to a Mach-Zehnder arrangement between points (a) and (b), except that two frequencies are present at (b). By maximising the contrast via adjusting the position of the labelled mirror and the input direction of the newly introduced probe, correct mode matching of both frequencies at the beam splitter can be ensured as well as a minimisation of $\Delta\phi_1$.

Two seed beams are injected into the ^{85}Rb. The position of the first is selected so as to maximise the amplitude correlations on the output probe/conjugate pair, p_1 and c_1. The second is then manipulated such that by eye the emitted probe p_2 overlaps the original conjugate c_1 and vice versa. Then the pump is removed and mirrors at the output are adjusted to mode-match the two un-amplified, single-frequency fields p_1 and p_2 onto the beam splitter. Finally the pump is reintroduced, generating the conjugate fields and the overall contrast can be detected. To optimise, either the position of the labelled mirror or the input angle of p_2 can be adjusted before repeating the process of mode-matching the probes in isolation then introducing the conjugates and detecting the contrast.

In practice, by adjusting these two factors in tandem a point could be reached showing contrast of 98% or more for both frequencies simultaneously. Now when the two input probes were removed, the vacuum fields could be known to be mode-matched effectively on the beam splitter whilst simultaneously fulfilling the requirement that $\Delta\phi_1 = 0$.

5.1.5 Seed-Pump Overlap

A final requirement for optimising the measurement of squeezing on the output signal is a repetition of a consideration from section 4.4.2. There it was described how the maximum overlap in the centre of the cell was not necessarily achieved when the gain on the seed field during a pass through the cell was maximised. Subtleties inherent in the phase matching condition mean that at $\delta = 0$, the optimum input position in terms of gain can sometimes be achieved when the probe/pump intersection point is not centred on the pump axis but rather slightly off-axis, where the pump intensity is weaker.

In the case of trying to measure for MSM squeezing the same process occurs. Due to the optimal parameters to perform these experiments including being at a

detuning of $\delta = 0$, when imaging from the centre of the cell in a gain-optimised arrangement it could occasionally be seen that the spatial overlap was poor. This poor overlap gives the response that the conjugate essentially travels further through the gain medium than the probe, or vice versa, giving them different profiles both in the near and far-field regimes. By monitoring the central overlap prior to any analysis it could be ensured that a good overlap was present, thus negating this problem.

5.2 Characterising the Multi-Spatial-Mode Squeezed Light

In order to prove the MSM nature of the squeezed signal, tests have been performed with a shaped LO beam. As the LO selects the mode of vacuum to be measured, then performing the measurement using a number of LOs interrogating a variety of spatial modes is a true test of the multi-mode nature of the squeezing in the signal field.

The spatial bandwidth of the squeezing is a measure of the number of separate modes that the squeezing operates on, given by the equation

$$b_s = \frac{w_0^2}{L_{coh}^2}, \tag{5.19}$$

where w_0 is the beam waist of the pump (1 mm) and L_{coh} is a transverse coherence length for a squeezed mode. This can be seen as describing essentially how many individual modes with an area equal to some coherence length L_{coh}^2 can fit into the beam waist of the pump field, similar to fitting straws of radius L_{coh} into a tube of radius w_0.

The coherence length itself is equal to the beam waist corresponding to a Rayleigh

range (defined in equation 1.47 as $\frac{\pi w_0^2}{\lambda/n_p}$) equal to the length of the gain region L_c, such that

$$L_{coh} = \sqrt{\frac{\lambda L_c}{\pi n_p}}. \tag{5.20}$$

Here λ is the wavelength of the pump (794.974 nm), L_c is the length of the interaction medium (12.5 mm) and n_p is the refractive index of the medium as experienced by the pump (~ 1, as seen in chapter 4). For our parameters $b_s = 316$.

In order to investigate this value experimentally, a method is used similar to [53] in which the LO of the homodyne detector is shaped using an opaque mask. As it is the LO that selects the mode of squeezed vacuum that is being measured, then shaping this LO means changing the mode that it interrogates.

The correlations between the $\hat{a}_1$ and $\hat{a}_2$ can be categorised and detected in two regimes, corresponding to the near-field and the far-field descriptions defined in section 1.5. The source photons are emitted in pairs, each pair from a specific location across the transverse beam profile and with opposite k vectors with respect to the pump field, as shown in part a) of figure 5.6. Analysis of near-field correlations equates to viewing the equal source position of each pair while far-field analysis correlates the momenta.

In the following discussion, it will be assumed that the near-field profile of the fields is in the shape of an R, while the far-field profile we will give the form of an L[4], as shown in figure 5.6 part b).

[4]As we are dealing with spatial manipulation of the transverse profile of the field we select these two forms as neither features an axis of symmetry, not to suggest that in reality one is the propagated far-field form of the other.

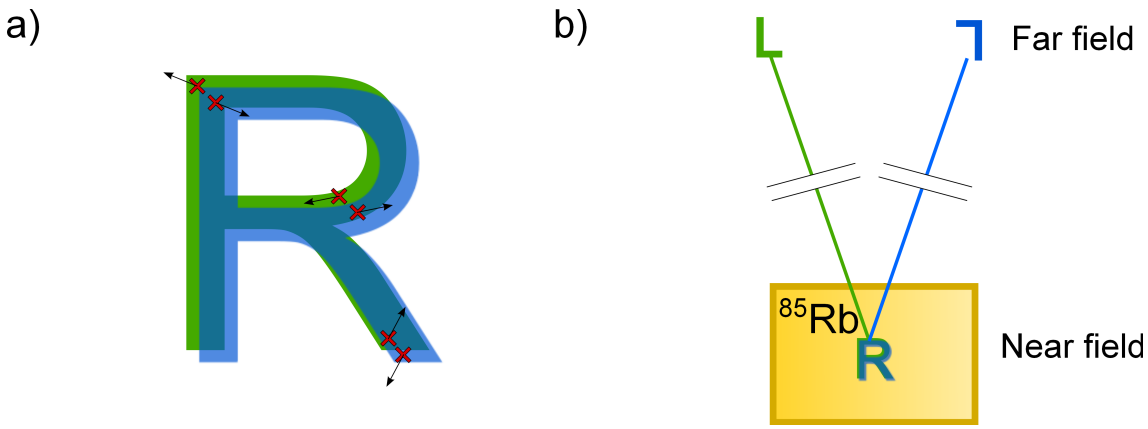

Figure 5.6: Shows a) The near-field position correlations of the emitted photon pairs along with the anti-correlated momenta. In b), shows the form of the transverse image profile in both the near and far-field pictures. The choice of image shape as a letter is arbitrary.

5.2.1 Near/Far-Field Correlation Detection

The near-field refers to the transverse profile of the signal field in the cell at the point the photon pairs are produced. The homodyne setup described in figure 5.3 operates in the near-field regime and serves to analyse a selection of the transverse signal profile defined by the form of the LO.

Conversely the correlations in momenta cause the far-field form of $\hat{a}_2$ to take an inverted form of the $\hat{a}_1$, as depicted in figure 5.6. In order to maintain that the far-field correlations are still co-propagating after combining the fields on the beam splitter it is necessary to invert the profile of one field both horizontally and vertically. Provided the paths taken by the two output fields to the beam splitter are essentially symmetrical then the horizontal profile matching will be dealt with automatically, i.e. the symmetry of the system ensures R/L maps to Я/Л. The consequence then is that in analysing the far-field form of the signal, to maintain the desired correlations one signal field output must be vertically inverted prior to BS1 in figure 5.3. If this is performed then the LO now serves to effectively detect the momentum correlations

within the cell. Again, shaping the LO allows for momentum correlations across arbitrary regions of the signal to be analysed.

5.2.2 Forming an Appropriate Local Oscillator

The shaping of the LO is performed by masking the input probe field such that a region of the field is blocked while the rest is transmitted. In order to simplify the masking process the field is enlarged before being masked so larger, less intricate masks can be used. The first and most primitive form of such a process is simply to position a razor in the path of the beam, giving the profile a hard straight edge. Shaped masks were also created, at first from paper and later utilising a 3D printer to create arbitrary masks out of plastic.

When using LOs featuring different transverse spatial profiles it is important to be able to view these profiles clearly. At the point of masking, the beam profile has a clearly defined form making the mode easy to view. However, as it propagates the effects of diffraction will deform this image, giving the field a different profile in the far-field to that in the near-field. Another issue is that the twin fields that form the LO are produced inside the ^{85}Rb cell, which due to the susceptibility has a lensing effect on the probe field. This has the result that unless the probe beam has a waist and a clearly defined profile inside the cell, the far-field propagation of the probe/conjugate frequencies will not be the same.

The solution to these issues is to recreate the field profile at the masking point inside the cell. If the clearly defined form of the LO imprinted by the mask is replicated at the point of conjugate generation then the near-field description of both fields will be identical while the far-field will be simple to characterise. To perform this, an imaging setup was introduced, designed in order to meet the following requirements:

- The transverse profile of the LO inside the cell is an image of its profile at the point where the mask is applied.
- The LO beam is collimated, with the beam waist located inside the cell.
- The size of the LO beam waist is around half that of the pump, in order to effect a comparably large gain region and generate strong amplification/conjugate generation.
- At the point of masking, the beam waist is large, thus simplifying the masking of the field.

The final imaging system is shown in figure 5.7, The first pair of lenses act on the beam emitted from a fibre[5], enlarging it and simplifying the masking process. This enlarged field (beam diameter $\sim 5\,\text{mm}$) then runs through a system of three lenses that, combined, reduce the beam waist by a factor of 5, collimate the field and place the location of the waist along with the image of the mask at a point inside the ^{85}Rb cell, some 60 cm away from the final lens.

The effectiveness of this system can be seen in figure 5.8 in which pictures of a masked beam are shown that display an image shortly after the masking position, and the resized image in the centre of the cell. It is this system that was utilised in the results given in section 5.3.

5.2.3 Imaging the Form of the Local Oscillator

Now the shaped LO has been created, we also wish to view the profile of the LO in the form that analyses the signal field, i.e. after the two frequencies have been combined. The choice of whether to view the near or far-field correlations in the signal will effect the manner in which the LO should be imaged.

[5]The fibre is used in order to clean the mode of the beam after the double-pass through the AOM, as described in chapter 3.

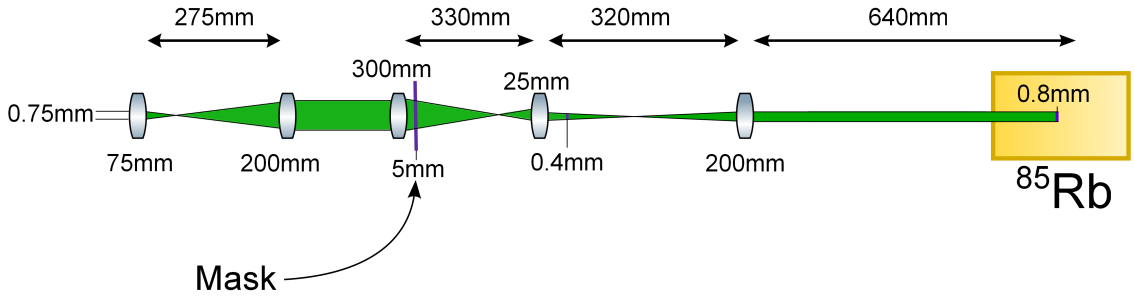

Figure 5.7: The top row shows the various lenses used to resize the probe input and ensure the mask position is geometrically imaged into the centre of the rubidium cell. Distances under lenses indicate focal lengths, while above is indicated the distance between lenses. Second row shows approximate form of beam including intended beam waist sizes at the location of object/image points. Not to scale.

Near-Field Imaging

In the near-field picture, we define the LO mode in terms of its transverse profile inside the cell. To view this we need only image this point onto a beam profiler later in the experiment. Experimentally this is performed using a $4f$ system whereby a lens of focal length f is placed at a distance of $2f$ from the cell, then the output is viewed at a distance of $2f$ from the lens. The lens should be placed past the point where the two composite bichromatic elements of the LO are recombined, as shown in the near-field imaging portion of figure 5.9.

This is the method used when taking the profiles shown in section 5.3.

Far-field Imaging

Viewing the far-field form of the LO is performed by placing the beam profiler at the focal point of a lens positioned after the two composite LO fields are mixed. The lens translates light incident at different angles into light at different positions in the focal plane, thus forming the far-field image of the LO.

However, in the far-field, as described, in order to capture the correlated portions

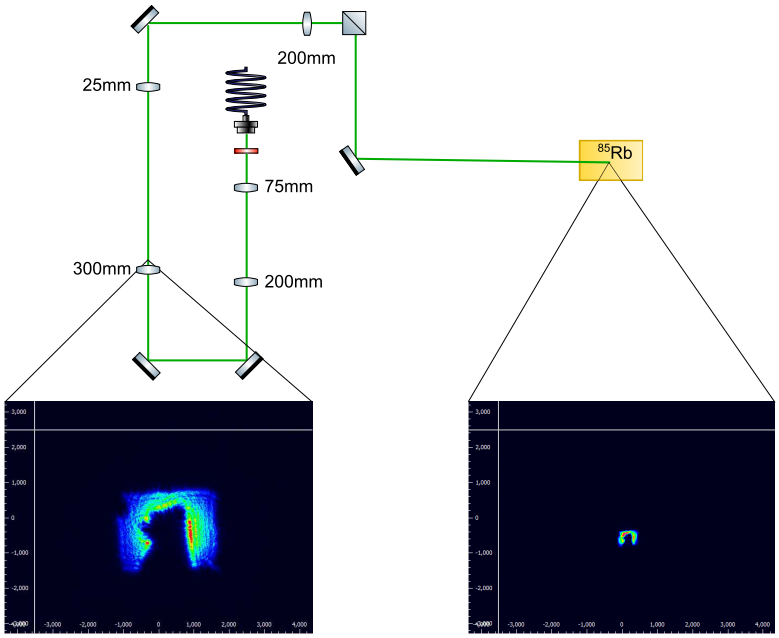

Figure 5.8: Shows the path taken for the probe beam from the fibre into the cell, including the imaging system. On the left is an image taken immediately after the location of the mask. On the right is an image taken in the location of the cell, showing the replication of the masked field at a reduced size. There is a slight alteration in the intensity distribution which may have been caused by minor movement of the mask in between measurements, however the spatial profile remains the same.

of the signal field, one part of the LO will also have to be inverted both horizontally and vertically. Note that again the horizontal mode-matching is automatic for a symmetric optical system.

Figure 5.10 shows the case where the signal and LO both have one of their output paths flipped vertically before being combined, resulting in an optimum final overlap and correct detection of correlations.

Experimentally, a vertical reversal can be achieved using three mirrors, however in this case the reversal is to be effected on two fields while maintaining their relative position to each other. I.e. after the reversal the flipped signal field should remain above the flipped LO field. To perform this operation a five-mirror apparatus was

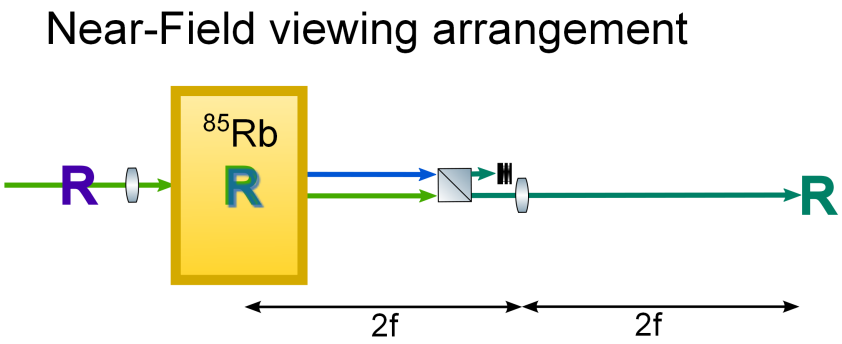

Figure 5.9: Shows the setup for imaging the near-field form of the LO. The profile seen on the detection apparatus is the same as that formed in the cell. This form views the correlations in terms of the position of the photons at the source.

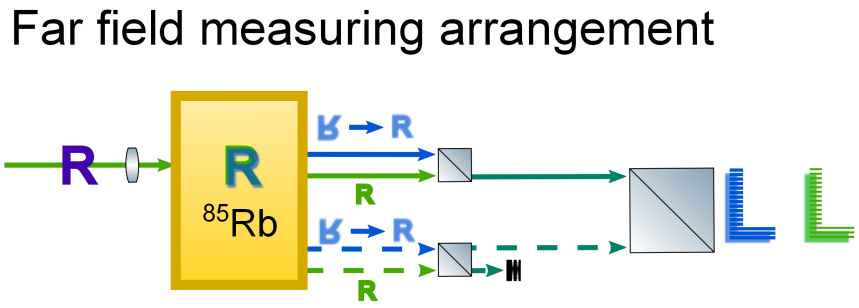

Figure 5.10: Shows the case where one LO output *and* the corresponding signal field are flipped, giving appropriate measurement and a well defined far-field LO.

created, where the conjugate side of both the LO and signal each pass through a three-mirror vertical system but with the entry/exit mirrors acting on the LO having a different angle to those flipping the signal. In this manner each beam is vertically inverted whilst maintaining their spatial relation to each other. This setup is shown in figure 5.11. Alignment of this proved to be exceedingly difficult and to compensate additional mirrors were positioned on the far side to realign each beam after the vertical reversal.

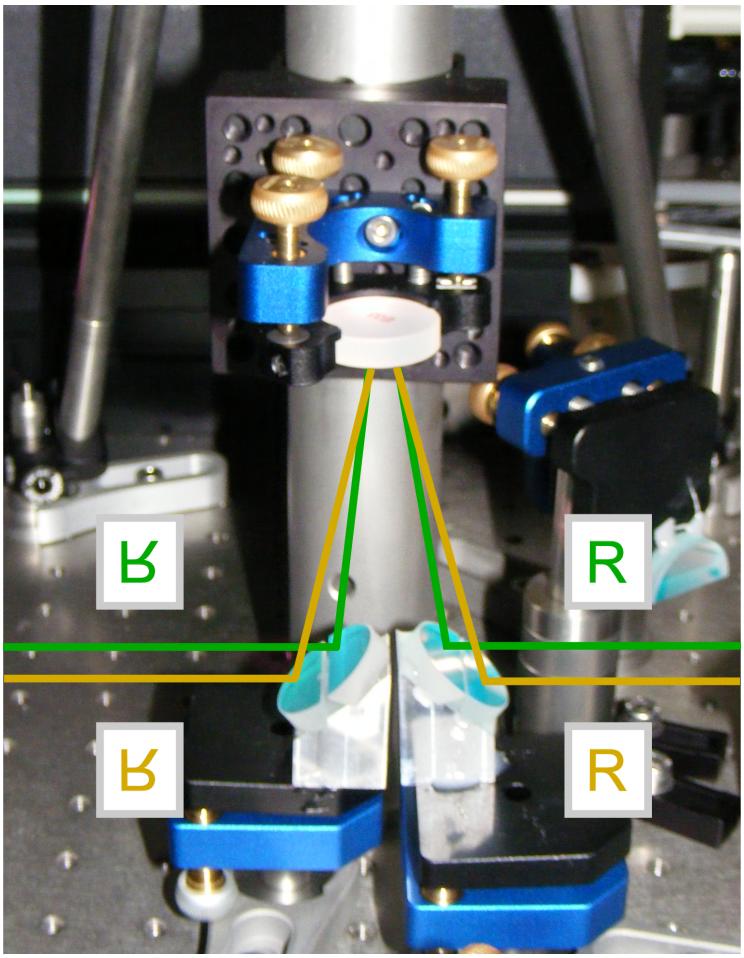

Figure 5.11: Apparatus used to reverse the vertical orientation of one pair of LO/signal beams for alignment with the other pair in the far-field. Use of colour only indicates two beam paths, while in practice one will be a bright beam and the other path will carry squeezed vacuum signal.

Results including this apparatus generally demonstrated squeezing, but not to the extent desired[1]. This is likely due to the fact that measurements utilising this setup were performed prior to the considerations of the zeroing of $\Delta\phi_1$ and the central overlap of the probe and pump fields. Due to time constraints, this apparatus was never re-introduced into the setup and as such, the near field analysis method was utilised for the majority of the results.

Summary

Both the near and far-field arrangements were used successfully to view squeezing on Gaussian signal field modes, to differing extents. So long as both the signal and the LO have the same operations performed on each, the final combination will demonstrate the squeezing effect. The sole requirement is that any spatial manipulation performed on the LO (be it the probe or conjugate part) should be matched by also performing the same operations on the corresponding part of the signal.

The conclusion here supports the case that the squeezing is genuinely multi-mode even before the inclusion of a complex imaging analysis as essentially the choice of whether to measure in the near or far-field is not detrimental to the presence of the effect, so long as the the way the measurement is implemented is carefully considered.

5.2.4 Experimental Procedure Chart

The complete procedure for obtaining a squeezing measurement through all of the above considerations is complex. For aiding understanding, it is presented in the form of a flow chart in figure 5.12.

[1]Whilst initial scans showed low levels of squeezing of around -1dB, the target set for really showing the potential of the process was -3dB.

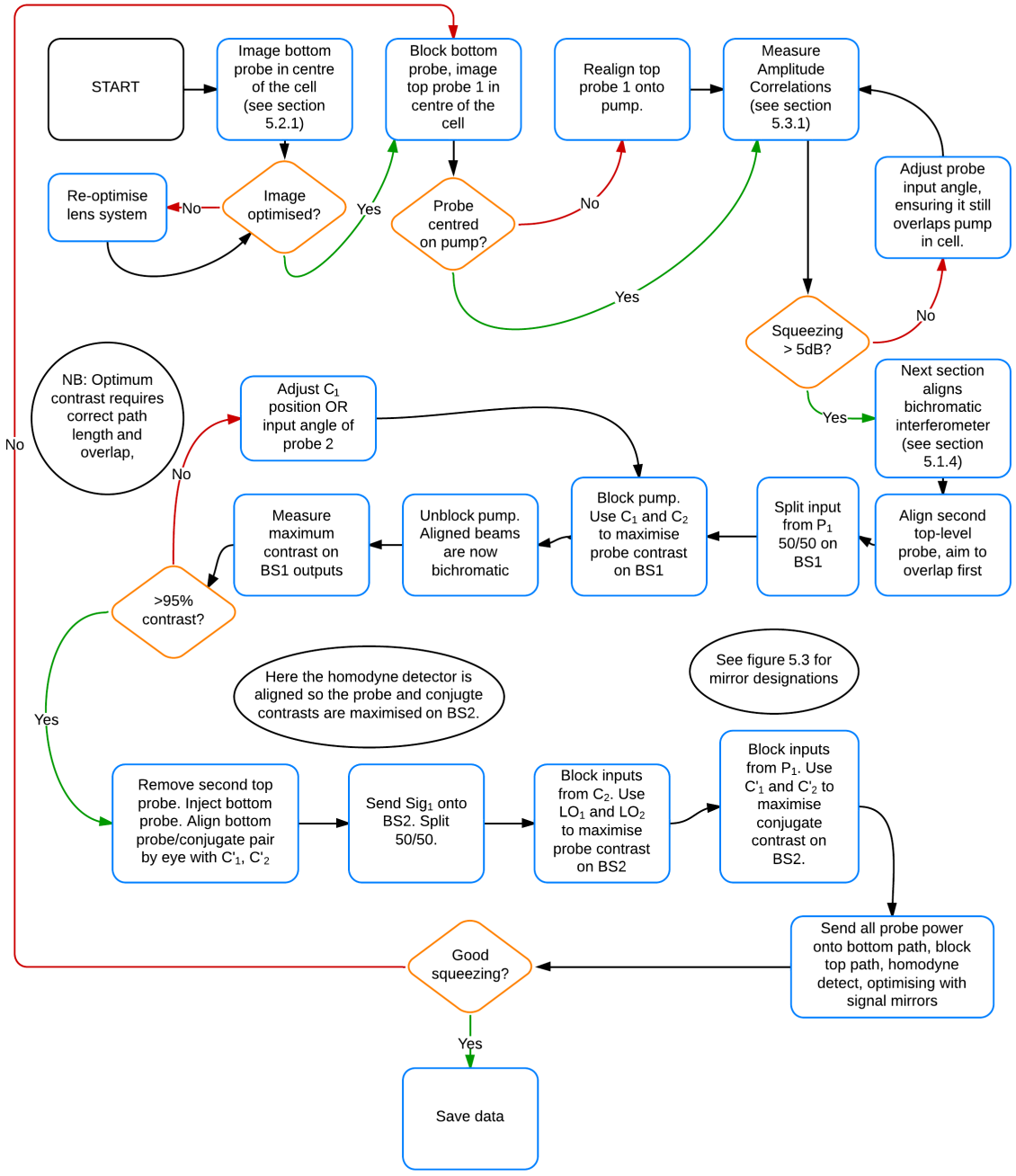

Figure 5.12: Flow chart describing the order of experimental procedure to measure the multi-mode squeezed signal. Notation corresponds to labelling of components in figure 5.3.

5.2.5 Photodetectors

Both methods of squeezed light detection described in chapter 1, the direct detection of amplitude correlations across two fields and the homodyne detection of quadrature squeezing, require the use of a balanced detector. While the essential design of such a detector is relatively standard, the specifics of the design play a large part in characteristics of the resulting device, such as the noise floor, the level of gain or the saturation intensity. This means a detector that performs well at measuring amplitude correlations on bright twin beams might not be best suited for homodyne detection.

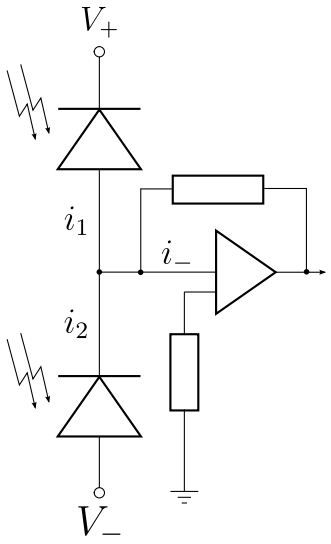

Figure 5.13: Shows the basic circuit that forms a balanced detector. The detector used was built according to a custom design by another member of the group.

The general diagram for a balanced detector is shown in figure 5.13. The basic principle is that the output signal i_- is the difference between the two input signals i_1 and i_2, which are each proportional to the intensity of light on the respective photodiode. This output signal is amplified before being sent on to the measurement apparatus. Selection of this amplifier affects both the minimum detectable difference signal and also the saturation level of the detector, governed by that of the amplifier,

and reached when the difference signal becomes too large.

In the absence of any light incident on either diode, some output noise will still be present. This is the technical noise and sets a limit on the minimal noise level readable by the detector. In this thesis, no special effort is made to minimise this, as because it is uncorrelated to the input photonic noise, it can be subtracted from the output results.

5.2.6 Amplitude Correlation Measurement

In order to be able to generate high levels of squeezing in the vacuum signal, it is required that at the output from the cell the twin fields share strong amplitude correlations. The extent of these correlations is relatively simple to measure, in accordance with the method described in section 1.4.1, and sets an upper limit of the level of squeezing expected from the later homodyne detection. The homodyned level will be reduced from this upper limit as a result of losses from the system, categorised further on in section 5.3.2.

Described in this subsection is the apparatus, method and results found from this ancillary experiment, performed regularly to ensure the level of correlations was maintained on a daily basis in the lab.

The setup for measuring the amplitude correlations is shown in figure 5.14. The cell is seeded and the emitted beams are sent onto the two photodiodes of a balanced detector. The output of the balanced detector is read out using both a spectrum analyser that measures the noise on the output current and an oscilloscope that can be used to see the voltage. This voltage can then be equated to the incident power on the diodes. The frequency at which the squeezing is detected on the spectrum analyser is 2.25 MHz, with the analyser in zero-span mode, meaning the noise is only shown at this frequency as it varies with time. 2.25 MHz is selected so as to be distant from a noise peak generated by the source laser at 1 MHz. Taking measurements

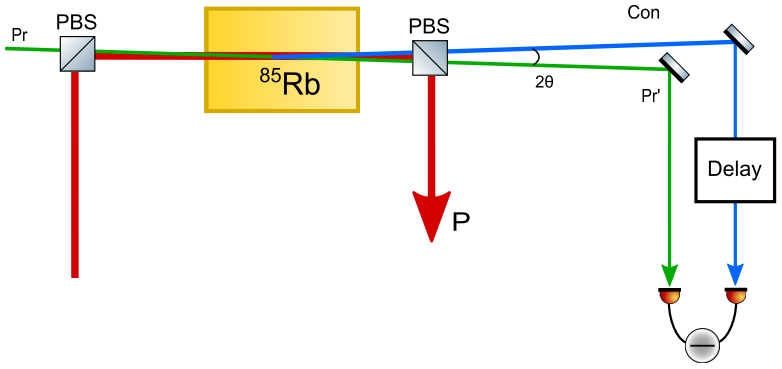

Figure 5.14: Shows the set-up used to measure the amplitude correlations between the probe and conjugate. The delay on the emitted conjugate line is to compensate for the slower propagation of the probe light within the cell.

across a wider span it can be shown that the squeezing remains at the same level up to this frequency and beyond. The precise bandwidth of the squeezing is controlled by the relative path lengths of the probe and the conjugate. Inside the cell the probe experiences a slow light effect due to the change in refractive index caused by the applied pump, as discussed in chapter 4. This causes a delay in the transit time for the probe field that the conjugate does not experience as it is further detuned from the resonance and so is affected less by the pump field. To counter for this, the path from the cell to the detector on the conjugate path is extended with respect to that of the probe by around 1.5 m, corresponding to a delay of around 5 ns. During the experiment, results were taken at $\approx 1 - 2.5$MHz and once squeezing was optimised at that location no further tuning of the delay line was made.

The noise on the signal must then be compared to the equivalent shot noise, i.e. the noise that would be detected if a beam with power

$$P = P_p + P_c \tag{5.21}$$

were split evenly onto the same balanced detector. Here P_p, P_c are the power of the

probe and conjugate beam. The shot noise measured on a beam with a certain power will differ depending on the specifics of the detector used, as described in section 5.2.5. For this reason the detector used was first calibrated to allow the deduction of shot noise for any given applied power. Figure 5.15 shows a basic arrangement by which a field's intensity can be split evenly into two paths which are then sent onto the ports of the balanced detector, generating an output with fluctuations at the SNL. The balance is found by rotating the wave plate until the signal is as close to zero as the scope is capable of measuring. By adjusting the input power of the field (maintaining an even split at the beam splitter) and measuring the output noise, the result is a linear fit that can then be used as a calibration for the detector in finding the expected shot noise for any given input power. An example fit is shown in figure 5.16.

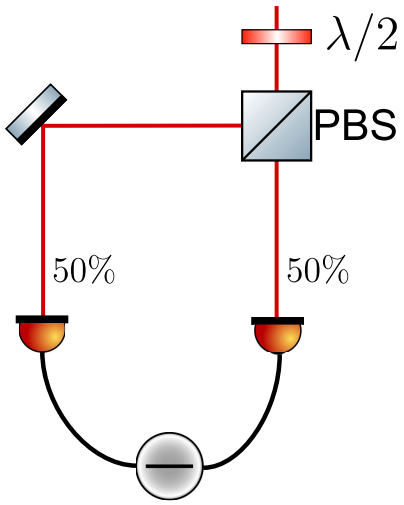

Figure 5.15: Shows the setup used to calibrate the balanced detector. By changing the input power and ensuring an even balance across the photodiodes using the $\lambda/2$ plate the shot noise can be found for a range of powers. These results can then be used to generate a calibration equation.

In a measurement of the amplitude squeezing, first the noise level on the spectrum analyser is recorded when both the probe and conjugate are incident on the detector.

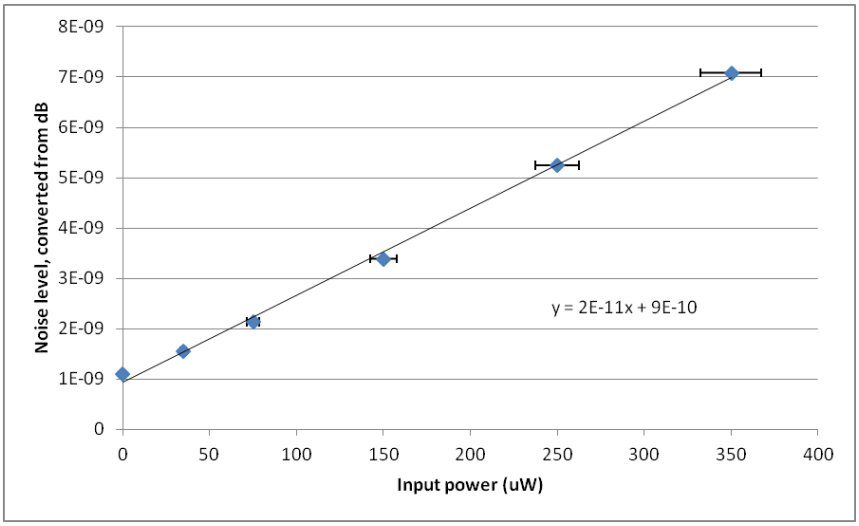

Figure 5.16: Shows the resulting linear fit used to then calculate the shot noise level for arbitrary input power levels that can then be compared to the correlations found from the twin beams to give a final squeezing measurement. Errors correspond to 5 % of value and are from uncertainties in reading out from digital power meter.

This is the reduced signal to be compared to the SNL. Next the total input power is found from the scope by first blocking the probe input and reading the conjugate power and then vice versa. From this total input power and the calibration performed previously, the SNL is found and the squeezing calculated based on these two noise levels. All data recording and calculations are performed by a program written in Octave.

Amplitude correlation squeezing of the order of $5-6$dB is regularly viewable in this arrangement with the present setup. On each run of the experiment, measurements of the amplitude correlations are taken and optimised by adjusting the probe input angle, making sure to maintain a good probe-pump overlap inside the cell. When strong correlations are seen, the further alignment can begin, as described in section 5.1.4.

5.3 Homodyne Detection Results

This section will describe the main results obtained from this experiment, those found through homodyne detection utilising first an LO with a Gaussian profile and then one with an adjusted form.

In all homodyne detection scans the spectrum analyser was configured as follows:

- Resolution Bandwidth = 30 kHz
- Video Bandwidth = 30 Hz
- span = zero span
- Sweep time = 2 s
- Frequency = 1 MHz

The scale of the noise detection is typically 2 dB per division for the Gaussian results in section 5.3.1 and 1 dB per division in sections 5.3.3 and 5.3.4.

5.3.1 Squeezing on a Gaussian Mode

The first experimental results for the homodyne detection of quadrature squeezing were obtained for an unblocked Gaussian LO. The plot is shown in figure 5.17.

The data has been renormalised so the grey line positioned at 0 dB is the shot noise of the LO, N_{shot}. This can be obtained by blocking the signal input to the beam splitter and taking the reading. The oscillating signal in blue is the noise on the quadrature ellipse of the squeezed state, $N_{squeezed}$, with the measured angle of the ellipse changing when the relative phase of the LO and the signal is modulated. This relative phase was adjusted by modulating a piezoelectric transducer on a mirror mount used to direct the LO into the homodyne detector. Problems with the performance of this piezo caused by the placement of the unit and amplitude of

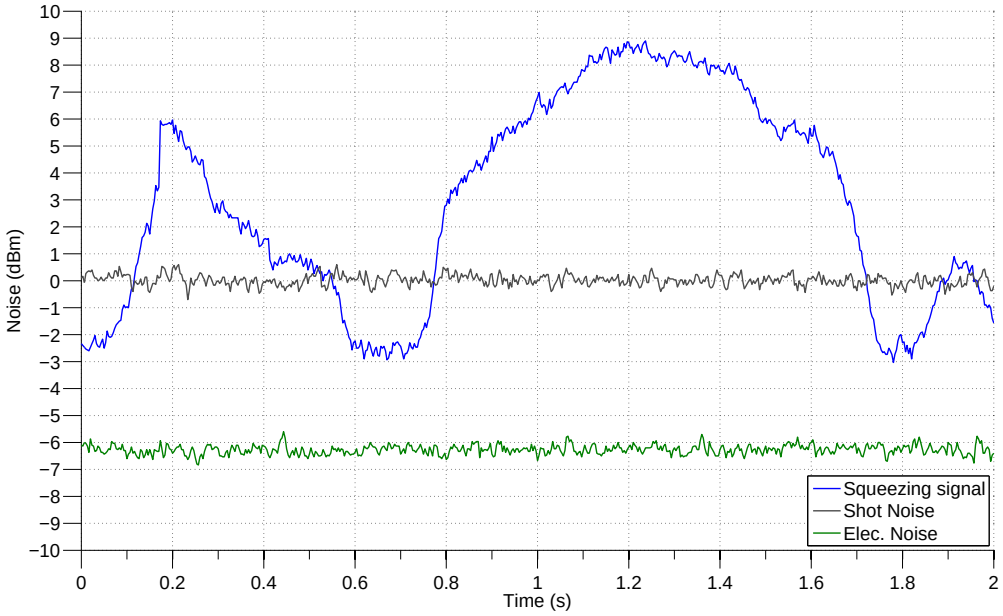

Figure 5.17: Shows the squeezing result when measuring the signal field with a bright Gaussian LO. The three traces correspond to the shot-noise level (in grey), the level detected by the homodyne method (blue) and the electronic noise floor (green). The relative phase of the LO and signal fields was modulated by a piezo. While the scan is clearly not linear, it still displays the minimum noise value seen by the trace, indicating a phase scan of greater than π.

the driving signal resulted in the erratic features of the trace, which at its lowest measures approximately -2.6 dB and at its peak 8.8 dB. The frequency of the driving signal was 1.7 Hertz.

The third line at -6.3 dB is the electronic noise floor, N_{tech}, the technical noise described in section 5.2.5. As mentioned however, this noise in uncorrelated to the photonic noise terms and can simply be subtracted. The level of squeezing is the ratio $N_{shot}/N_{squeeze}$. Taking the technical noise into account, the result is then

$$Sq = \frac{N_{shot} - N_{tech}}{N_{squeeze} - N_{tech}}. \tag{5.22}$$

When converted to dB and after removing the technical noise, the final level of

squeezing shown in figure 5.17 is −4.2dB below the shot noise. The anti-squeezing seen is around 8.6dB, considerably more than the squeezing displayed. In theory these values should be identical as they both come from the same squeeze factor, however this is only true at the source. During the propagation of the fields extra noise terms are introduced such as losses and mismatches on beam splitters that serve to reduce the measurable squeezing while leaving the anti-squeezing unaffected. As such in all the results presented the degree of squeezing is reduced from that of the anti-squeezing.

Experimental results were also achieved for an applied Gaussian LO, this time using an alternative detector with a higher gain amplifier. This increased gain reduces the visual effect of the technical noise as, while N_{tech} for this detector is higher than previously, N_{shot} and $N_{squeeze}$ are both increased still further, with $N_{shot} - N_{tech} \approx 12$ dB. This reduced visual effect makes the optimisation more effective as it allows for smaller differences to be seen more clearly. The smoothness of the scan was also improved by increasing the effectiveness of the transducer being used to scan the phase. This was achieved by doubling the amplitude of the applied drive signal and inserting a second transducer, combining to increase the extent of the scan to over 3π (as seen in figure 5.18 and others) and reduce the adverse environmental drift effects seen on the data in figure 5.17. The results of these scans are shown in figure 5.18 and clearly demonstrate a smoother scan of the relevant signal that is no longer effectively reduced by the proximity to the technical noise floor.

The extent of the squeezing seen in 5.18 is reduced from that seen in 5.17, however it still serves to demonstrate the effectiveness of the later setup combined with the alternate detector.

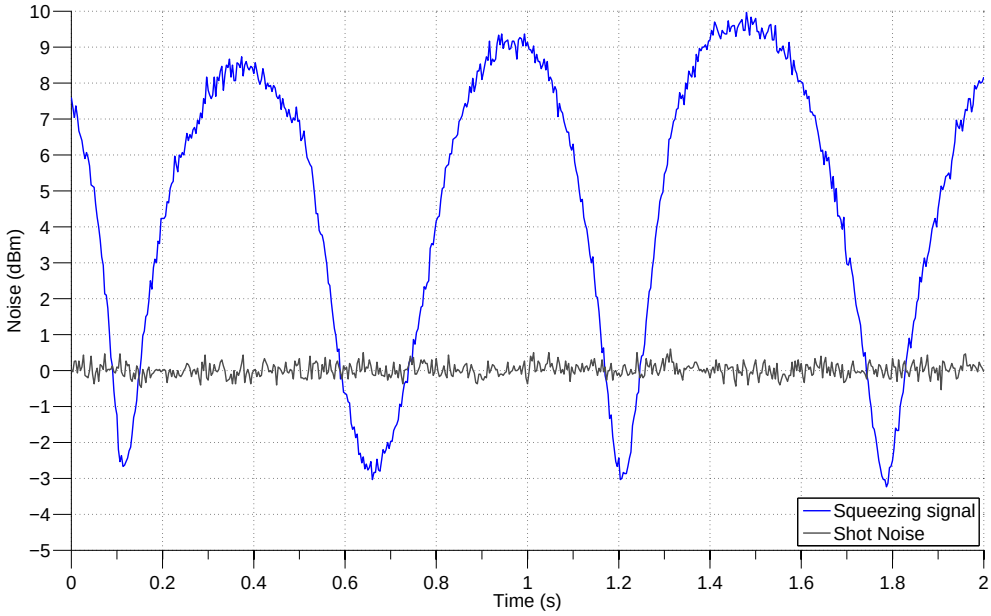

Figure 5.18: Shows a second squeezing spectrum, this time produced using a different detector designed such that the electronic noise floor is significantly below the expected shot noise level. This means less compression is present on the results. Also here a smoother squeezing profile is generated due to the usage of an improved method of scanning the phase. The separation between consecutive minima corresponds to a phase difference of π.

5.3.2 The Effect of Losses

From the point where the photon pairs are emitted through to the point of detection it is vital that losses be minimised. This is because as described in section 2.3 the effect of losses is akin to that of mixing with an un-squeezed vacuum field on a beam splitter. In the case of the TMSS this will cause a reduction in correlations and in the SMSS will increase the quadrature noise on the field. The losses from a single reflection on the mirrors used are given from the product catalogue as 0.1%. Passing out through the vacuum chamber window also causes a loss of 0.5%.

At the point where the signal fields are mixed on the first beam splitter the degree of misalignment is also damaging to the output squeezing level. As described in

section 5.1.4, the optimal contrast is achieved when the two fields are perfectly mode-matched. In the case of co-aligning two bright beams, the effect of a mismatch is to inject some amount of vacuum into the final state. Here the two signal inputs equate to noisy vacuum fields and the extent of misalignment equates to injecting some of this noise in an uncorrelated manner. When the two-mode state is correctly aligned the correlations transfer to the output fields, while if misaligned, the output is mixed with uncorrelated photons from a field carrying more noise across all quadratures than a coherent state[6]. Figure 5.19 shows how the contrast affects the contents of the field measured by the LO. Phase mis-match, either from non-optimised alignment or a non-zero value of ϕ_1 will cause the introduction of the surrounding vacuum field.

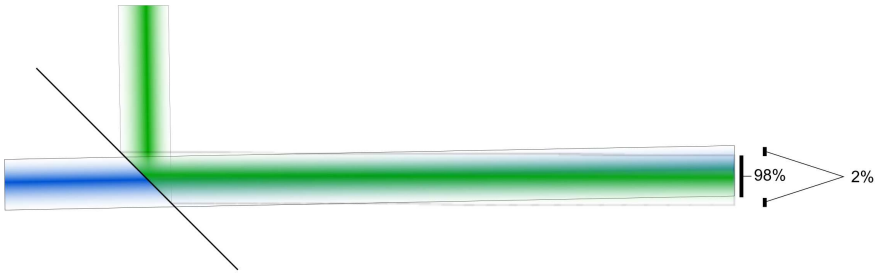

Figure 5.19: Shows two fields combining on a beam splitter. Only one output is shown and the degree of mismatch is not accurate to the percentages given. The result is 98% correlated signal while the other 2% introduces a highly damaging level of noise due to the anti-squeezing on the other quadrature. The adjustment on the overlap is made via mirrors prior to the splitter, which has a defined position that splits an input field 50/50.

On the homodyne detection plots 5.17 and 5.18, the anti-squeezing level is visible as well as the squeezing level. In the case of ideal squeezing and no losses, the level of anti-squeezing and level of squeezing should be the same, however clearly this is not the case in the results shown. This is primarily due to the effects of loss after the fields are emitted from the cell. At the point the TMSS signal fields combine on

[6]Recall from sections 1.3 and 2.3.1 how the twin beams that form a two-mode squeezed state are individually noisy.

the beam splitter, any misalignment will inject not a minimum uncertainty vacuum state, but the anti-squeezed vacuum field. As such the alignment at this stage is crucial in maximising the squeezing measured by the LO.

Figure 5.20 shows the effect of this mismatch. Taking the anti-squeezing measured by the LO (and thus the squeezing at the source) to be 10 dB, the figure shows how the level of squeezing on the output from this beam splitter varies with the achieved level of contrast. Here we see that even for 98% contrast on the beam splitter, the squeezing on the result has fallen to nearly half its original value. When the contrast is reduced to 90%, the output field actually demonstrates noise above the shot noise despite originating as a TMSS. If the squeezing at the source is given by $S_i = 10\text{dB}$, then the correctly overlapped percentage α features fluctuations at 10% of the shot noise, while this is combined with the remainder $\beta = 1 - \alpha$ that carries 10 times the shot noise. Adding these noise terms the output features a level of squeezing

$$S_o = \alpha S_i + \beta b S_i, \tag{5.23}$$

which is displayed in figure 5.20 in with the squeezing once more represented in dB. Here we see that even for 98% contrast on the beam splitter, the squeezing on the result has fallen to nearly half its original value. When the contrast is reduced to 90%, the output field actually demonstrates noise above the shot noise despite originating as a TMSS.

In reality these figures are unrealistically optimistic as they do not include unavoidable losses due to absorption in the vapour and the presence of windows and mirrors in aligning the fields. They represent an ideal scenario and demonstrate an upper bound to the measurements achievable. This effect could be mitigated with correct alignment of the LO however. If there is a 98% mismatch between the two signal components then if the probe element of the bichromatic LO is perfectly

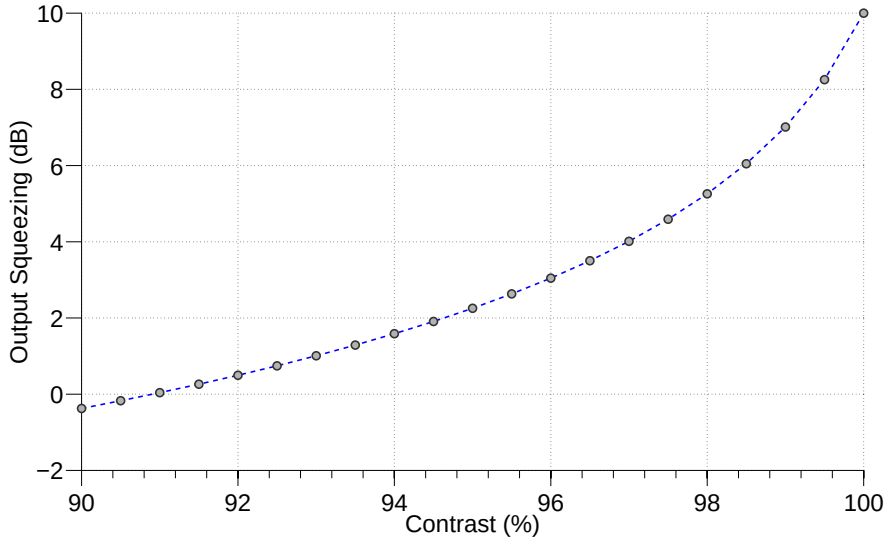

Figure 5.20: Assuming a source with 10 dB of squeezing/anti-squeezing at the source and no other losses, shows the squeezing after mixing the fields in relation to the contrast achieved. The swiftness of the decline when contrast $\neq$ 100% highlights the importance of correct mode-matching.

aligned with the probe frequency elements of the signal then the conjugate element of the LO is only interrogating 98% of the correlated conjugate signal photons. Conversely if the conjugate frequency component of the LO is perfectly aligned then the opposite is the case. Optimal would be the situation where each LO interrogates 99 % of its respective signal element, which can reduce the mismatch by a half.

A second interesting result from this calculation is shown in figure 5.21 that takes a contrast level of 97% and plots the output squeezing level as a function of the (anti)squeezing produced in the cell. Here we see that up to around 7dB they each rise, though the output is always reduced from the original as expected. However, above a source squeezing level around 7.5 dB the extent of the effect of the anti-squeezing mixed in by the 97% contrast level is actively detrimental to the measurable squeezing on the result.

At a Source Squeezing level of 9.5 dB as shown in the results above it the squeezing

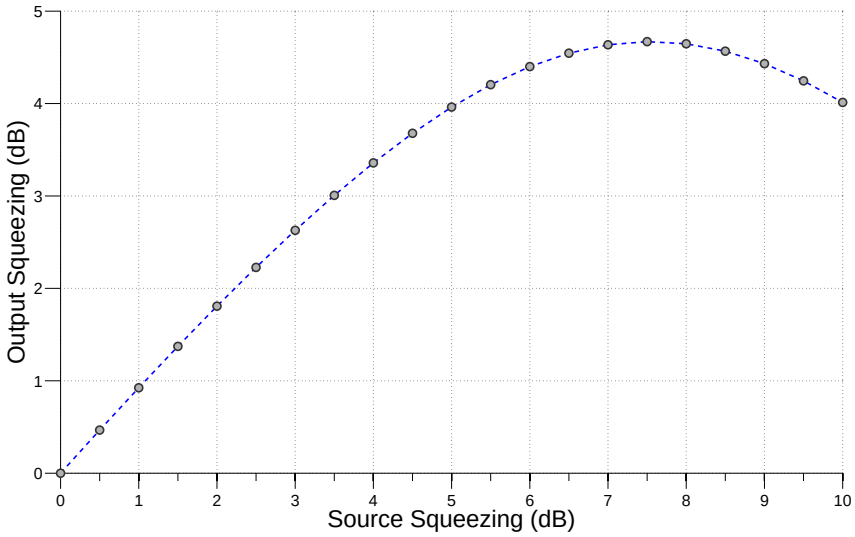

Figure 5.21: For an assumed contrast of 97%, shows the relationship between squeezing in the TMSS and squeezing in the SMSS. The turning point indicates that with contrast $\neq 100\%$ it is in some cases preferable to reduce the degree of 4WM in the cell.

measured would be improved by reducing the efficiency of the 4WM process e.g. by increasing the detuning δ or reducing the temperature of the cell. Similar calculations show a minimum contrast of $\sim 93.3\%$ is required to ever witness squeezing of > 3dB.

5.3.3 Multi-Spatial-Mode Analysis

The first attempt towards characterising the multi-mode nature of the squeezing effect was to position a razor across the path of the LO in the mask position as defined in section 5.2.3.

To check how the squeezing changes in the presence of higher order modes, an iris is placed prior to the cell near a focal point of the LO seed. By adjusting the transmission through the iris at the focal point the higher order spatial modes can be arbitrarily excluded in a process called spatial filtering. For a mostly closed iris, the LO is approximately Gaussian in form despite the presence of the razor, whilst when

fully opened the maximal sharpness is achieved. This contrast is shown in figure 5.22 in which the X profile of the beam as recorded by the beam profiler is displayed, along with explicitly showing the $1/e^2$ values for the blocked side in comparison to the unblocked side. The imaging was performed in the manner described in 5.2.3 in the near-field description.

These profiles attempt to recreate the sharp form of the LO in the cell. The reason for the decrease in sharpness even in the situation of a fully opened spatial filter is due to unavoidable losses of some higher order frequencies as the LO passes through the optical setup. These can be caused by the positioning of either mirrors or imaging lenses not being ideal for forming the 4f setup desired. By adjusting the spatially filtering iris and measuring the corresponding level of squeezing achieved, the hope should be that the inclusion of higher order modes has a lesser effect on the final results than blocking half the field would be expected to produce. The iris also causes some level of diffraction when closed further, resulting in the slightly broader beam shown.

Three sets of results were taken, with the iris in different stages of closing. Firstly, for an open iris, featuring the first profile shown in figure 5.22. With the iris fully open, the presence of the sharp feature caused by the razor is clearly visible. For this plot the $1/e^2$ value on the unblocked (left-hand) side is 38 µm, while for the blocked (right-hand) side the $1/e^2$ distance value is 79 µm. The homodyne results are shown in figure 5.23.

The second row of figure 5.22 shows the case where the spatial filter is partially closed. The $1/e^2$ values for the blocked and unblocked sides are 47 and 81µm respectively. This adjustment demonstrates both the effect of beginning to remove higher order frequencies from the profile and also the broadening in the overall profile caused by diffraction through the iris. The homodyne results are also shown in figure 5.23.

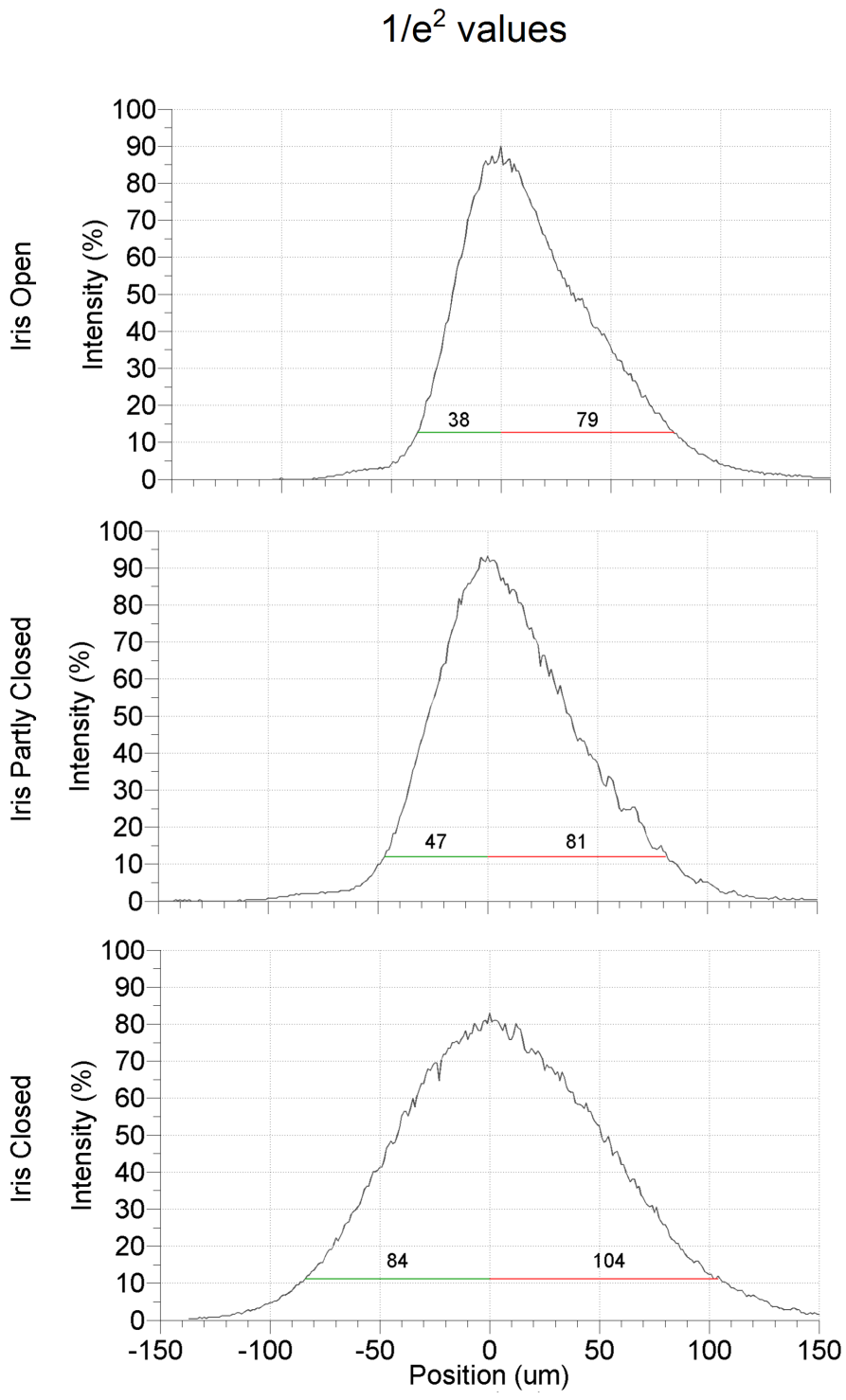

Figure 5.22: Shows the X-profiles of the LO beam used to interrogate the signal when the beam is half-blocked by a razor. An iris placed at the point shown in figure 5.7 serves as a spatial filter to optionally remove higher order spatial modes. The top row corresponds to this iris being fully opened, the middle to a partly closed iris and the final to the case when the spatial filter is closed and the vast majority of higher order frequencies have been removed. The $1/e^2$ values for both the blocked and unblocked sides are given explicitly.

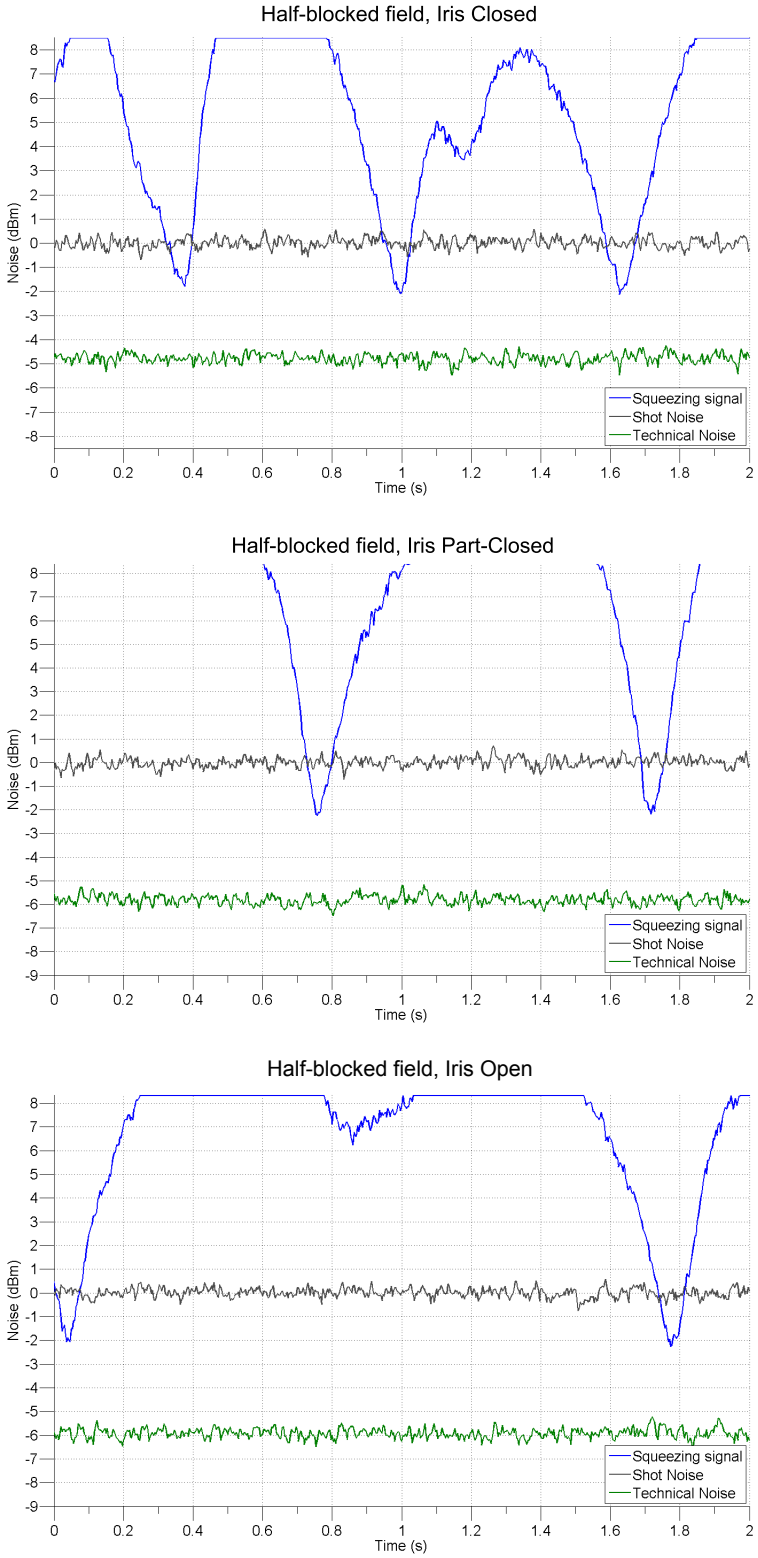

Figure 5.23: Shows the Homodyne results when the spatial filter is closed, partly closed or opened. In each case the gray line is the shot noise (measured by blocking the LO and normalised to 0dB) the green line is the electronic noise floor f the detector and the blue curves are the squeezing signal measured when modulating the relative phase of the LO and signal fields.

Finally the case of a closed iris is shown in the bottom row of figure 5.22. The $1/e^2$ values are 84 and 104µm, and at this stage almost all visible effects of the higher order of frequencies have been removed.

In all cases the intensity in figure 5.22 is described in arbitrary units. This actual intensity is not relevant as the squeezing is always measured with respect to the shot noise, which is also measured separately in each case. Also the removal of technical noise is always performed, so any effect it may have in the homodyne plots can be taken into account. The maximum anti-squeezing level in these cases is unfortunately not visible as the scale was adjusted to 1dB per division to aid in the fine-tuning of the alignment in order to maximise the squeezing measured.

The precise value of squeezing on display in each case is difficult to pinpoint as the minimum noise level is only displayed intermittently. What is clear is that in all cases the noise falls below the QNL by a minimum of 1.5dB. Taking the visible squeezing level to be at this 1.5dB minimum in each case and then subtracting the technical noise the resulting values are:

- Iris open = 2.16 dB
- Iris part closed = 2.07 dB
- Iris closed = 2.49dB

The presence of > 2 dB squeezing in each case is a strong indication of the MSM nature of the correlations in the signal. While there is no perfect trend between the degree of higher order modes present in the LO and the squeezing result, this serves as a preliminary test of the desired features.

5.3.4 Squeezing on Arbitrary Shapes

To further test the squeezing, a more complex mask was formed quickly, again as proof of principle that obscure combinations of spatial modes would also demonstrate

squeezing from the same emitted signal fields. The mask used in this case was etched from paper and again two cases were tested, with and without a spatial filter. The mask used is shown in figure 5.24.

Figure 5.24: Shows the form of the mask used to select an essentially arbitrary spatial mode, not selected to conform to any particular symmetries or base modes.

Figure 5.25 shows the LO profile both with the spatial filter wide open (LHS) and again with the iris closed (RHS) the scale on the image is around 1500 Px (1 Px = 6.75 µm)on the beam profiler in both cases.

Figures 5.26 and 5.27 show the homodyne detection results for the open and closed iris arrangement respectively. As in section 5.3.3 the readings are taken at 1dB per division, meaning the full extent of the anti-squeezing can not be seen. The main visible difference is some of the light is blocked by the iris when mostly closed in this scenario, bringing the noise viewed closer to the technical noise of the detector.

Here, assuming the squeezing visible on the traces to be at 1 dB in both cases and subtracting the technical noise the results in terms of squeezing for each case are:

- Iris open = 1.67 dB
- Iris closed = 2.31 dB

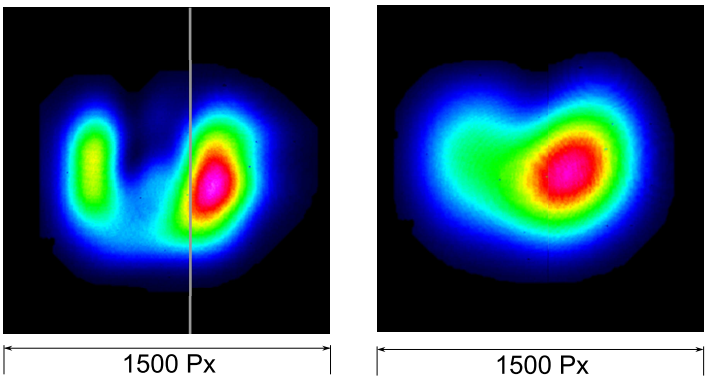

Figure 5.25: Shows the profile of the LO when masked with an arbitrary shape. The left hand side features no spatial filtering, while on the right hand side the higher frequencies have been removed. The line passing over the LHS image is the curser of the beam profiler. The presence of the pump here causes lensing and amplification effects that result in a reduction in sharpness between the images taken here and those seen in figure 5.8.

While demonstrating less squeezing than in the previous case, again the existence of sub-QNL noise is a good indication that the correlations are being carried on relatively arbitrary selectable transverse profiles of the signal.

5.4 Directions for Further Analysis

The plan for a more comprehensive analysis of the MSM nature of the squeezing involved the use of 3D printed masks featuring slots of varying widths in order to characterise at what point the correlations are no longer detectable, however this has not yet been achieved. Instead other options for defining the nature of this form of squeezing as well as hopefully implementing some applications are described in this section.

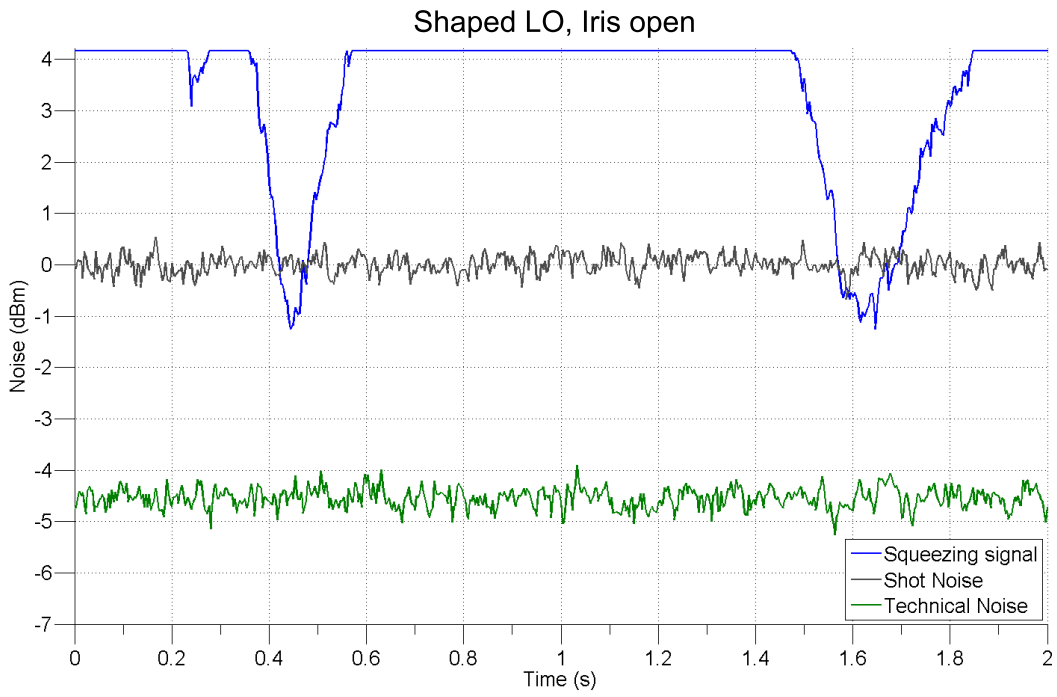

Figure 5.26: Shows the homodyne reading for the shaped LO with the iris opened.

5.4.1 Spatial Squeezing

Having demonstrated the MSM nature of the squeezed vacuum signal in a preliminary fashion via homodyne detection with a shaped LO, the next stage is to transfer the reduced noise levels of the vacuum onto a bright beam that can then be used for a range of purposes from imaging to the carriage of quantum information.

For detecting sub-shot noise fluctuations it is important that the bright field the signal field is combined with should itself feature low amplitude fluctuations, and should ideally represent a coherent state. In the case of the homodyne detection scheme, classical noise on the LO does not present a problem to the squeezing detection as any classical noise on the field is cancelled out on the two photodiodes due to common mode rejection. In this case however, we intend to detect the fluctuations on only a single field and so no such rejection occurs. In fact the method used to generate the LO fields will amplify any noise present at the seed input,

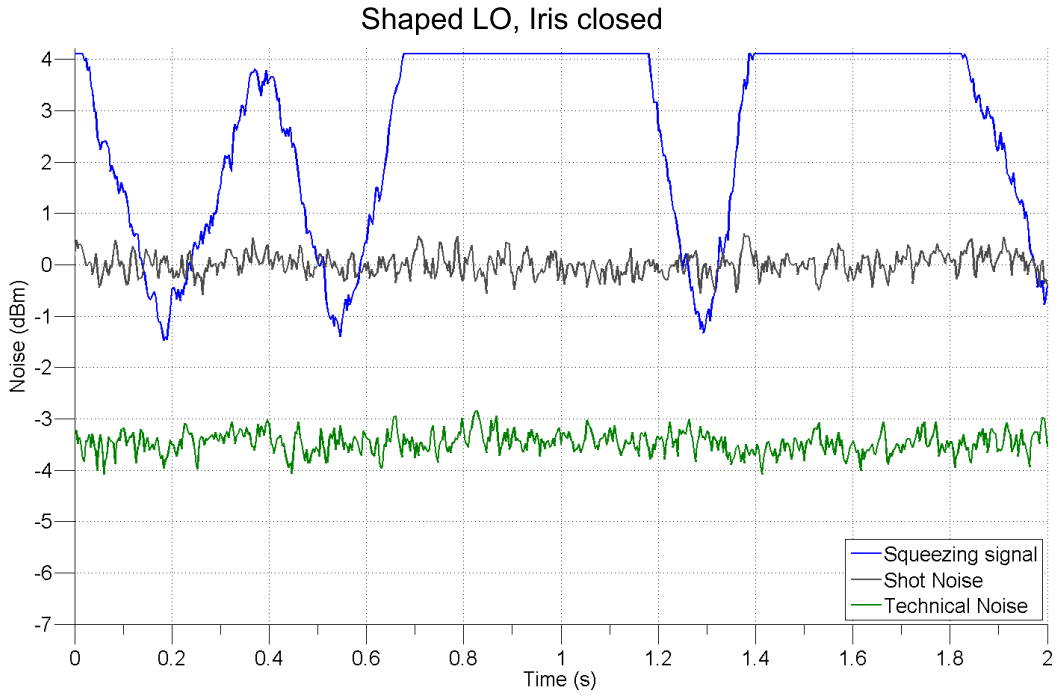

Figure 5.27: Shows Shows the homodyne reading for the shaped LO with the iris closed.

leading to a beam on which the noise is potentially significantly above the shot noise.

The solution to this is that classical noise scales with the square of the power of the beam while quantum noise scales linearly. This means reducing the amplitude of the beam brings the noise level down towards the shot noise limit.

In the experiment planned, the intention is to replace the 50/50 beam splitter used in the homodyne detector for a 99/1 beam splitter. Such a splitter has a 99% transmittance factor and as such will combine 99% of the squeezed vacuum signal with 1% of the bichromatic beam that formed the LO. By reducing the amplitude of the bright beam to 1% of its original power, the noise on the remaining beam should be at approximately the shot noise level.

As described previously, the noise remaining on the output from the 99/1 beam splitter is fundamentally connected to the relative phase of the two input fields. As

such to ensure the low amplitude noise of the output field this phase will have to be precisely locked.

As a first step, we intend to look at spatial squeezing. After combining 99% of the bichromatic signal field with 1% of the LO, the correlations should be such that the spatial variation in amplitude should be below the QNL.

In order to view these local amplitudes accurately across the profile of the beam we intend to use a camera with a particularly high quantum efficiency. The specifications for the camera are as follows:

- QE: 98% at 800 nm
- Pixel size: 13 µm x 13 µm
- Sensor size: 1024 x 1024 pixels
- Readout noise (at 2 MHz): 9 e- (where e- = electrons)
- Vertical shift speed: < 3.2 µs per row up to 18 µs per row (programmable)
- Dark noise (at 70 °C): 0.02e-/pixel/sec
- Full well capacity: 100 ke- (where 1 ke- = 1000 electrons)

and the device itself is shown in figure 5.28

By convolving the camera's pixel readouts with well-defined functions, subtractions can be made following standard TEM mode patterns to demonstrate the extent of these spatially distributed fluctuations with the aim of showing them to be below the QNL.

5.4.2 Phase-squeezing

In all of the results presented, the squeezing measured is that on the amplitude of the field. In every case, when the greatest anti-squeezing is seen, the opposite quadrature

Figure 5.28: Shows the high quantum efficiency camera that will be used in the future to monitor the intensity correlations on a pixel-by-pixel basis. The camera features a 98% quantum efficiency at 800 nm with a sensor size of 1024 x 1024 pixels each measuring 13 µm x 13 µm.

i.e. the phase of the field, should be squeezed below the shot noise. Measurement of the phase noise would enable finer analysis of the form of the quadrature ellipse as well as the phase relation between the LO and the signal field.

5.4.3 Camera Noise Measurement

The current detection program for the camera takes eight images in quick succession during one shutter cycle. The sensor region is divided into eight strips and the data from each image shifted down one strip after every image taken. The first one or two images as well as the final image collected are usually less clear due to the opening/closing of the shutter so typically only five of the images taken are used in the calculation.

These five collected images can then be analysed in any form such that intensity across half of the region is subtracted from the remaining intensity. This result is

then averaged over the collected image and over time will hopefully demonstrate that the transverse amplitude fluctuations taken per shot are below the minimum expected.

This will display more quantitatively the multi-mode nature of the reduced amplitude fluctuations.

Conclusion

In this thesis a description has been given of the phenomenon of squeezed light, electromagnetic radiation with reduced uncertainty below the QNL. We also described how 4WM in atomic ^{85}Rb vapour can generate two-mode squeezed states. The notable feature of this method is that, unlike many others, the squeezing produced is present across a large number of spatial modes simultaneously.

Heated atomic vapours had previously been used as a source of squeezed light for many years, although the degree of noise reduction was always limited by factors such as high absorption, Doppler broadening of atomic linewidths and lensing of the field within the medium. In order to explain the success of this arrangement a more detailed breakdown of the susceptibility responsible for the behaviour of the EM radiation in the medium was given. This analysis showed that for the correct arrangement of fields, despite the high levels of absorption, the high coupling strength of the system still allows for a large amount of gain to be produced on an incident probe field. The nature of the process also serves to produce a conjugate field featuring amplitude fluctuations correlated with those of the probe field.

An experiment was performed that showed good agreement with the calculated predictions for the gain response in the regime where this gain level and the absorption level were both relatively weak. At higher values the congruence is reduced due to a number of additional factors given and justified. Interestingly, we see the result that the situation that optimises the strength of the 4WM process and satisfies the

phase-matching condition sits too closely to the atomic resonance feature to produce strongly correlated output fields due to the high level of absorption. Instead, if the frequency of the applied field is increased and injected in a geometry that satisfies the effective phase matching condition then a balance can be reached between the coupling strength and the absorption that allows for the generation of fields with amplitude correlations detected to be around 6-8 dB below the SNL.

Taking these correlated output fields further, the multi-mode nature of the correlations emitted from the vapour have been utilised to generate a field of MSM quadrature squeezed vacuum. The nature of the squeezing in this field has been analysed and shown to produce noise levels of up to 3-4 dB below the QNL. This has been shown to be the case when the signal field is interrogated with an LO featuring a selection of transverse spatial profiles.

Special consideration has been given to the nature of the mode selection of the fields such that the correlations are both transmitted optimally from the TMSS to the SMSS and also that the correctly correlated regions are interrogated by the LO.

The LO itself has a bichromatic form, produced by combining a pair of bright fields also emitted via the 4WM process. This two-colour LO has been shown to be capable of detecting correlations separated by a frequency of 6 GHz. The maximum value of squeezing detected on the signal field was 4.2dB below the QNL.

When different modes of the field were analysed, noise reduction was still shown, albeit to a lower extent. This acts as the proof of principle that these MSM squeezed signals can hopefully be utilised to reduce the amplitude fluctuations of a bright field across a number of spatial modes simultaneously. Such an achievement would hopefully have a number of interesting potential applications in the fields of quantum information or imaging technology and would certainly serve as a fascinating new tool for the field of quantum imaging or perhaps quantum optics in general.

Appendix A

Derivation of the Susceptibilities

In order to arrive at the susceptibilities $\chi_{pp}, \chi_{cc}, \chi_{pc}, \chi_{cp}$ described in chapter 4 it is first necessary to describe the density matrix formalism from which the stationary solutions generate the complex decay rates and atomic population levels of the system. The form taken for this derivation follows that used in ref. [79].

The density operator $\hat{\rho}$ describes completely the probabilty for a system to be in any state or superposition of states. In terms of the possible eigenstates and probabilities it takes the form

$$\hat{\rho}_{nm} = \sum_{m} p_m |\psi_n\rangle\langle\psi_m| \tag{A.1}$$

where $|\psi_m\rangle$ is the mth eigenstate and p_m is the probability of being in that state.

Taken as a complete matrix over all available states m across an ensemble of atoms the diagonal terms $\hat{\rho}_{mm}$ refer to the populations of each state and the of-diagonal terms $\hat{\rho}_{nm}$ refer to the extent of the coherence between the two states. That is to say a non-zero value for $\hat{\rho}_{nm}$ indicates that the system is in a coherent superposition of the states n and m.

The evolution of the elements of the density matrix with time can be obtained

via the expression

$$i\hbar\frac{d\hat{\rho}_{nm}}{dt} = \left[\hat{\rho}, \hat{H}\right] \tag{A.2}$$

where $\hat{H}$ is the Hamiltonian for the system, which can typically be separated into

$$\hat{H} = \hat{H}_a + \hat{H}_{int}. \tag{A.3}$$

with $\hat{H}_a$ corresponding to the atomic Hamiltonian and $\hat{H}_{int}$ the interaction part. This interaction part is given by the dipole approximation as $\hat{H}_{int} = -\hat{\mathbf{d}}.E(t)$ where $\hat{\mathbf{d}}$ is the dipole moment operator and E(t) is the applied electric field.

To further simplify the situation the rotating wave approximation can be introduced in which elements of the density matrix are transformed to those in a rotating frame to be

$$\hat{\rho}_{nm} = \sigma e^{-i\omega_{f,nm}t} \tag{A.4}$$

where now ω_{nm} is the angular frequency of the field coupling the states n and m.

In this new form the equations of motion for the matrix elements are

$$\begin{aligned}\dot{\sigma}_{nm} = i(\Delta_{nm} - \gamma_{nm})\sigma_{nm} + \frac{i}{\hbar}\sum_{\nu}[&\mathbf{d}_{n\nu}\cdot\mathbf{E}(\mathbf{r},t)\sigma_{\nu m}e^{-i(\omega_{\nu m}-\omega_{nm})t} \\ &- \mathbf{d}_{\nu m}\cdot\mathbf{E}(\mathbf{r},t)\sigma_{n\nu}e^{-i(\omega_{n\nu}-\omega_{nm})t}]\end{aligned} \tag{A.5}$$

$$\begin{aligned}\dot{\sigma}_{nn} = &\frac{i}{\hbar}\sum_{\nu}\left[\mathbf{d}_{n\nu}\cdot\mathbf{E}(\mathbf{r},t)\sigma_{\nu n}e^{-i\omega_{\nu n}t} - \mathbf{d}_{\nu n}\cdot\mathbf{E}(\mathbf{r},t)\sigma_{n\nu}e^{-i\omega_{n\nu}t}\right] \\ &+ \sum_{E_m>E_n}\Gamma_{nm}\sigma_{mm} - \sum_{E_m<E_n}\Gamma_{mn}\sigma_{nn}\end{aligned} \tag{A.6}$$

where in this notation Δ_{mn} is the detuning of the ω_{mn} field from the transition from level n to m, Γ_{nm} is the specific decay rate from n to m, γ_{nm} is the dipole dephasing

between the two states n, m and is related to the population decay rates Γ_n by

$$\gamma_n m = (\Gamma_n - \Gamma_m)/2 + \gamma_{nm}^{col}, \tag{A.7}$$

where γ_{nm}^{col} contains the dephasing rate from atomic collisions.

To now obtain the full atomic response of the system the polarisation must also be introduced. For a dilute atomic vapour, thus assuming no interactions, the polarisation is equal to

$$\mathbf{P} = N\langle\hat{\mathbf{d}}\rangle \tag{A.8}$$

where N is the atomic number density and $\langle\hat{\mathbf{d}}\rangle$ is the averaged atomic dipole moment. This can be expanded across all relevant transitions

$$\mathbf{P} = N\sum_{n,m}\mathbf{d}_{nm}\sigma_{nm}e^{-i\omega_{nm}t} \tag{A.9}$$

giving the polarisation response to a specific field

$$E_f = \mathcal{E}_f e^{i(\mathbf{k}_f\mathbf{r}-\omega_f t)} \tag{A.10}$$

coupling the n, m transition is described as

$$\mathbf{P}(\omega_{f,nm}) = N\mathbf{d}_{nm}\sigma_{nm}e^{i(\mathbf{k}_f\mathbf{r}-\omega_f t)} = \epsilon_0\chi(\omega_{f,nm})\mathcal{E}_f e^{i(\mathbf{k}_f\mathbf{r}-\omega_f t)} \tag{A.11}$$

From here the susceptibility can now be obtained in the form

$$\chi(\omega_{f,nm}) = \frac{N\mathbf{d}_{nm}\sigma_{nm}}{\epsilon_0\mathcal{E}_f} \tag{A.12}$$

meaning the frequency-dependent susceptibility of the medium can be explicitly

obtained from the stationary RWA elements of the density matrix of the system.

Now the present situation can be introduced, where a single strong pump field E_0 couples the transitions $|1\rangle \rightarrow |3\rangle, |2\rangle \rightarrow |4\rangle$. The electric field in the medium can be expressed as

$$\mathbf{E}(\mathbf{r},t) = \mathcal{E}_0 e^{i(\mathbf{k}_0\mathbf{r}-\omega_0 t)}\epsilon_0 + \mathcal{E}_p e^{i(\mathbf{k}_p\mathbf{r}-\omega_p t)}\epsilon_p + \mathcal{E}_c e^{i(\mathbf{k}_c\mathbf{r}-\omega_c t)}\epsilon_c + c.c. \tag{A.13}$$

Here the subscripts $0, p, c$ refer to elements of the total field corresponding to the pump, probe and conjugate frequency respectively, with $\mathcal{E}$ representing the field amplitude, $\mathbf{k}$ the wave vector, ω the frequency and ϵ a unit vector corresponding to the polarisation of each field.

Using these forms, the equations of motion for the density matrix elements in the RWA are as follows

$$\dot{\sigma}_{11} = \frac{i}{2}(\Omega_1^* e^{-i\mathbf{k}_0\cdot\mathbf{r}}\sigma_{31} + \Omega_p^* e^{-i\mathbf{k}_p\cdot\mathbf{r}}\sigma_{41} - \Omega_1 e^{i\mathbf{k}_0\cdot\mathbf{r}}\sigma_{13} - \Omega_p e^{i\mathbf{k}_p\cdot\mathbf{r}}\sigma_{14}) + \Gamma_{13}\sigma_{33} + \gamma_{14}\sigma_{44} \tag{A.14}$$

$$\dot{\sigma}_{22} = \frac{i}{2}(\Omega_c^* e^{-i\mathbf{k}_c\cdot\mathbf{r}}\sigma_{32} + \Omega_2^* e^{-i\mathbf{k}_0\cdot\mathbf{r}}\sigma_{42} - \Omega_c e^{i\mathbf{k}_c\cdot\mathbf{r}}\sigma_{23} - \Omega_2 e^{i\mathbf{k}_0\cdot\mathbf{r}}\sigma_{24}) + \Gamma_{23}\sigma_{33} + \gamma_{24}\sigma_{44} \tag{A.15}$$

$$\dot{\sigma}_{33} = \frac{i}{2}(\Omega_1 e^{i\mathbf{k}_0\cdot\mathbf{r}}\sigma_{13} + \Omega_c e^{i\mathbf{k}_c\cdot\mathbf{r}}\sigma_{23} - \Omega_1^* e^{-i\mathbf{k}_0\cdot\mathbf{r}}\sigma_{31} - \Omega_c^* e^{-i\mathbf{k}_c\cdot\mathbf{r}}\sigma_{32}) - \Gamma_3\sigma_{33} \tag{A.16}$$

$$\dot{\sigma}_{44} = \frac{i}{2}(\Omega_p e^{i\mathbf{k}_p\cdot\mathbf{r}}\sigma_{14} + \Omega_2 e^{i\mathbf{k}_0\cdot\mathbf{r}}\sigma_{24} - \Omega_p^* e^{-i\mathbf{k}_p\cdot\mathbf{r}}\sigma_{41} - \Omega_2^* e^{-i\mathbf{k}_0\cdot\mathbf{r}}\sigma_{42}) - \Gamma_4\sigma_{44} \tag{A.17}$$

$$\dot{\sigma}_{43} = \frac{i}{2}(\Omega_2 e^{i\mathbf{k}_0\cdot\mathbf{r}}\sigma_{23} + \Omega_p e^{i\mathbf{k}_p\cdot\mathbf{r}}\sigma_{13} - \Omega_1^* e^{-i\mathbf{k}_0\cdot\mathbf{r}}\sigma_{41} - \Omega_c^* e^{-i\mathbf{k}_c\cdot\mathbf{r}}\sigma_{42}) + (i\Delta_2 - i\Delta_1 - \gamma_{43})\sigma_{43} \tag{A.18}$$

$$\dot{\sigma}_{42} = \frac{i}{2}(\Omega_2 e^{i\mathbf{k}_0\cdot\mathbf{r}}\sigma_{22} + \Omega_p e^{i\mathbf{k}_p\cdot\mathbf{r}}\sigma_{12} - \Omega_c e^{i\mathbf{k}_c\cdot\mathbf{r}}\sigma_{43} - \Omega_2 e^{i\mathbf{k}_0\cdot\mathbf{r}}\sigma_{44}) + (i\Delta_2 - i\delta - \gamma_{42})\sigma_{42} \tag{A.19}$$

$$\dot{\sigma}_{41} = \frac{i}{2}(\Omega_2 e^{i\mathbf{k}_0\cdot\mathbf{r}}\sigma_{21} + \Omega_p e^{i\mathbf{k}_p\cdot\mathbf{r}}\sigma_{11} - \Omega_1 e^{i\mathbf{k}_0\cdot\mathbf{r}}\sigma_{43} - \Omega_p e^{i\mathbf{k}_p\cdot\mathbf{r}}\sigma_{44}) + (i\Delta_2 - \gamma_{43})\sigma_{41} \tag{A.20}$$

$$\dot{\sigma}_{32} = \frac{i}{2}(\Omega_c e^{i\mathbf{k}_c\cdot\mathbf{r}}\sigma_{22} + \Omega_1 e^{i\mathbf{k}_0\cdot\mathbf{r}}\sigma_{12} - \Omega_c e^{i\mathbf{k}_c\cdot\mathbf{r}}\sigma_{33} - \Omega_2 e^{i\mathbf{k}_0\cdot\mathbf{r}}\sigma_{34}) + (i\Delta_1 - i\delta - \gamma_{32})\sigma_{32} \tag{A.21}$$

$$\dot{\sigma}_{31} = \frac{i}{2}(\Omega_c e^{i\mathbf{k}_c\cdot\mathbf{r}}\sigma_{21} + \Omega_1 e^{i\mathbf{k}_0\cdot\mathbf{r}}\sigma_{11} - \Omega_1 e^{i\mathbf{k}_0\cdot\mathbf{r}}\sigma_{33} - \Omega_p e^{i\mathbf{k}_p\cdot\mathbf{r}}\sigma_{34}) + (i\Delta_1 - \gamma_{31})\sigma_{31} \tag{A.22}$$

$$\dot{\sigma}_{21} = \frac{i}{2}(\Omega_c^* e^{-i\mathbf{k}_c\cdot\mathbf{r}}\sigma_{31} + \Omega_2^* e^{-i\mathbf{k}_0\cdot\mathbf{r}}\sigma_{41} - \Omega_1 e^{i\mathbf{k}_0\cdot\mathbf{r}}\sigma_{23} - \Omega_p e^{i\mathbf{k}_p\cdot\mathbf{r}}\sigma_{24}) + (i\delta - \gamma_{21})\sigma_{21} \tag{A.23}$$

It is this set of equations that need to be solved under the conditions appropriate for considering the 4WM in order to provide the susceptibilities in the forms they take in equations 4.2a through 4.2d in section 4. These appropriate conditions include the

assumption that the transitions $|1\rangle \rightarrow |2\rangle$, $|3\rangle \rightarrow |4\rangle$ are dipole forbidden, that each field couples only one transition and that the two Rabi couplings from the pump are at the same frequency $\Omega_1 = \Omega_2 = \Omega_0$.

Bibliography

[1] Strekalov DV, Sergienko AV, Klyshko DN, Shih YH. Observation of Two-Photon Ghost Interference and Diffraction. Physical Review Letters. 1995 May;74(18):3600–3603. Available from: http://link.aps.org/doi/10.1103/PhysRevLett.74.3600.

[2] Treps N, Grosse N, Bowen WP, Fabre C, Bachor HA, Lam PK. A Quantum Laser Pointer. Science. 2003 Aug;301(5635):940–943. Available from: http://www.sciencemag.org/content/301/5635/940.

[3] Lugiato LA, Gatti A, Brambilla E. Quantum imaging. Journal of Optics B: Quantum and semiclassical optics. 2002;4(3):176183. Available from: http://www.tp.physique.usherbrooke.ca/experiences_fichiers/Quantum%20imaging/ob2372.pdf.

[4] Kolobov MI, Kumar P. Sub-shot-noise microscopy: imaging of faint phase objects with squeezed light. Optics Letters. 1993 Jun;18(11):849–851. Available from: http://ol.osa.org/abstract.cfm?URI=ol-18-11-849.

[5] Boto AN, Kok P, Abrams DS, Braunstein SL, Williams CP, Dowling JP. Quantum Interferometric Optical Lithography: Exploiting Entanglement to Beat the Diffraction Limit. Physical Review Letters. 2000 Sep;85(13):2733–2736. Available from: http://link.aps.org/doi/10.1103/PhysRevLett.85.2733.

[6] D'Angelo M, Chekhova M, Shih Y. Two-Photon Diffraction and Quantum Lithography. Physical Review Letters. 2001 Jun;87(1). Available from: http://link.aps.org/doi/10.1103/PhysRevLett.87.013602.

[7] Fabre C, Fouet JB, Matre A. Quantum limits in the measurement of very small displacements in optical images. Optics Letters. 2000;25(1):7678. Available from: http://www.opticsinfobase.org/abstract.cfm?&id=286.

[8] Lantz E, Devaux F. Parametric amplification of images. Quantum and Semiclassical Optics: Journal of the European Optical Society Part B. 1997 Apr;9(2):279. Available from: http://iopscience.iop.org/1355-5111/9/2/014.

[9] Kolobov MI, Fabre C. Quantum limits on optical resolution. Physical Review Letters. 2000;85(18):37893792. Available from: http://link.aps.org/doi/10.1103/PhysRevLett.85.3789.

[10] Corzo NV, Marino AM, Jones KM, Lett PD. Noiseless Optical Amplifier Operating on Hundreds of Spatial Modes. Physical Review Letters. 2012 Jul;109(4):043602. Available from: http://link.aps.org/doi/10.1103/PhysRevLett.109.043602.

[11] Rayleigh JWS. The collected optics papers of Lord Rayleigh. Washington, DC: Optical Society of America; 1994.

[12] Zalevsky Z, Mendlovic D. Optical Superresolution. Springer; 2004.

[13] Park SC, Park MK, Kang MG. Super-resolution image reconstruction: a technical overview. Signal Processing Magazine, IEEE. 2003;20(3):2136. Available from: http://ieeexplore.ieee.org/xpls/abs_all.jsp?arnumber=1203207.

[14] Irani M, Peleg S. Improving resolution by image registration. CVGIP: Graphical Models and Image Processing. 1991 May;53(3):231–239. Available from: http://www.sciencedirect.com/science/article/pii/104996529190045L.

[15] Kimble HJ, Mandel L. Theory of resonance fluorescence. Physical Review A. 1976;13(6):2123. Available from: http://pra.aps.org/abstract/PRA/v13/i6/p2123_1.

[16] Carmichael HJ, Walls DF. A quantum-mechanical master equation treatment of the dynamical Stark effect. Journal of Physics B: Atomic and Molecular Physics. 1976 Jun;9(8):1199. Available from: http://iopscience.iop.org/0022-3700/9/8/007.

[17] Kimble HJ, Dagenais M, Mandel L. Photon antibunching in resonance fluorescence. Physical Review Letters. 1977;39(11):691695. Available from: http://authors.library.caltech.edu/6051/.

[18] Reid MD, Walls DF, Dalton BJ. Squeezing of quantum fluctuations via atomic coherence effects. Physical Review Letters. 1985;55(12):12881290. Available from: http://link.aps.org/doi/10.1103/PhysRevLett.55.1288.

[19] Slusher RE, Hollberg L, Yurke B, Mertz JC, Valley JF. Squeezed states in optical cavities: A spontaneous-emission-noise limit. Physical Review A. 1985 May;31(5):3512–3515. Available from: `http://link.aps.org/doi/10.1103/PhysRevA.31.3512`.

[20] Ho ST, Wong NC, Shapiro JH. Single-beam squeezed-state generation in sodium vapor and its self-focusing limitations. Optics Letters. 1991 Jun;16(11):840–842. Available from: `http://ol.osa.org/abstract.cfm?URI=ol-16-11-840`.

[21] Raizen MG, Orozco LA, Xiao M, Boyd TL, Kimble HJ. Squeezed-state generation by the normal modes of a coupled system. Physical Review Letters. 1987 Jul;59(2):198–201. Available from: `http://link.aps.org/doi/10.1103/PhysRevLett.59.198`.

[22] Maeda MW, Kumar P, Shapiro JH. Observation of squeezed noise produced by forward four-wave mixing in sodium vapor. Optics Letters. 1987 Mar;12(3):161–163. Available from: `http://ol.osa.org/abstract.cfm?URI=ol-12-3-161`.

[23] Lambrecht A, Coudreau T, Steinberg AM, Giacobino E. Squeezing with cold atoms. EPL (Europhysics Letters). 1996 Oct;36(2):93. Available from: `http://iopscience.iop.org/0295-5075/36/2/093`.

[24] Levenson MD, Shelby RM, Aspect A, Reid M, Walls DF. Generation and detection of squeezed states of light by nondegenerate four-wave mixing in an optical fiber. Physical Review A. 1985 Sep;32(3):1550–1562. Available from: `http://link.aps.org/doi/10.1103/PhysRevA.32.1550`.

[25] Milburn G, Reid M, Walls D, Shelby R, Levenson M. Theory of Squeezed Light Generation in Optical Fibers. Journal of the Optical Society of America a-Optics Image Science and Vision. 1986 Dec;3(13):P47–P47.

[26] Shelby RM, Levenson MD, Perlmutter SH, DeVoe RG, Walls DF. Broad-Band Parametric Deamplification of Quantum Noise in an Optical Fiber. Physical Review Letters. 1986 Aug;57(6):691–694. Available from: `http://adsabs.harvard.edu/abs/1986PhRvL..57..691S`.

[27] Wu LA, Kimble HJ, Hall JL, Wu H. Generation of Squeezed States by Parametric Down Conversion. Physical Review Letters. 1986 Nov;57(20):2520–2523. Available from: `http://link.aps.org/doi/10.1103/PhysRevLett.57.2520`.

[28] Tapster PR, Rarity JG, Satchell JS. Use of parametric down-conversion to generate sub-Poissonian light. Physical Review A. 1988 Apr;37(8):2963–2967. Available from: http://link.aps.org/doi/10.1103/PhysRevA.37.2963.

[29] Eberle T, Steinlechner S, Bauchrowitz J, Händchen V, Vahlbruch H, Mehmet M, et al. Quantum Enhancement of the Zero-Area Sagnac Interferometer Topology for Gravitational Wave Detection. Physical Review Letters. 2010 Jun;104(25). Available from: http://link.aps.org/doi/10.1103/PhysRevLett.104.251102.

[30] Mehmet M, Ast S, Eberle T, Steinlechner S, Vahlbruch H, Schnabel R. Squeezed light at 1550 nm with a quantum noise reduction of 12.3 dB. Optics Express. 2011 Dec;19(25):25763–25772. Available from: http://www.opticsexpress.org/abstract.cfm?URI=oe-19-25-25763.

[31] Lassen M, Delaubert V, Janousek J, Wagner K, Bachor HA, Lam P, et al. Tools for Multimode Quantum Information: Modulation, Detection, and Spatial Quantum Correlations. Physical Review Letters. 2007 Feb;98(8). Available from: http://link.aps.org/doi/10.1103/PhysRevLett.98.083602.

[32] Yonezawa H, Furusawa A. Continuous-variable quantum information processing with squeezed states of light. Optics and Spectroscopy. 2010 Mar;108(2):288–296. Available from: http://link.springer.com/10.1134/S0030400X10020189.

[33] Caves CM. Quantum-mechanical noise in an interferometer. Physical Review D. 1981;23(8):1693. Available from: http://prd.aps.org/abstract/PRD/v23/i8/p1693_1.

[34] Collaboration TLS. A gravitational wave observatory operating beyond the quantum shot-noise limit. Nature Physics. 2011 Dec;7(12):962–965. Available from: http://www.nature.com/nphys/journal/v7/n12/full/nphys2083.html.

[35] Grote H, Danzmann K, Dooley KL, Schnabel R, Slutsky J, Vahlbruch H. First Long-Term Application of Squeezed States of Light in a Gravitational-Wave Observatory. Physical Review Letters. 2013 May;110(18):181101. Available from: http://link.aps.org/doi/10.1103/PhysRevLett.110.181101.

[36] Armstrong JA, Bloembergen N, Ducuing J, Pershan PS. Interactions between Light Waves in a Nonlinear Dielectric. Physical Review. 1962 Sep;127(6):1918–1939. Available from: http://link.aps.org/doi/10.1103/PhysRev.127.1918.

[37] Giordmaine JA, Miller RC. Tunable Coherent Parametric Oscillation in LiNbO3 at Optical Frequencies. Physical Review Letters. 1965 Jun;14(24):973–976. Available from: http://link.aps.org/doi/10.1103/PhysRevLett.14.973.

[38] Jedrkiewicz O, Jiang YK, Brambilla E, Gatti A, Bache M, Lugiato L, et al. Detection of Sub-Shot-Noise Spatial Correlation in High-Gain Parametric Down Conversion. Physical Review Letters. 2004 Dec;93(24). Available from: http://link.aps.org/doi/10.1103/PhysRevLett.93.243601.

[39] Yao E, Franke-Arnold S, Courtial J, Padgett MJ, Barnett SM. Observation of quantum entanglement using spatial light modulators. Optics Express. 2006;14(26):1308913094. Available from: http://eprints.gla.ac.uk/28371/1/28371.pdf.

[40] Brida G, Genovese M, Ruo Berchera I. Experimental realization of sub-shot-noise quantum imaging. Nature Photonics. 2010 Feb;4(4):227–230. Available from: http://www.nature.com/doifinder/10.1038/nphoton.2010.29.

[41] Galvez EJ. Preparing photon pairs entangled in any desired spatial modes via interference. In: SPIE Defense, Security, and Sensing; 2011. p. 805706805706. Available from: http://proceedings.spiedigitallibrary.org/proceeding.aspx?articleid=1271039.

[42] Padgett M, Leach J, Jack B, Romero MJ, Giovannini D, Franke-Arnold S, et al. Spatial Light Modulators: Single-Photon, Spatial-Mode Analyzers. In: International Conference on Quantum Information. OSA Technical Digest (CD). Optical Society of America; 2011. p. QTuE2. Available from: http://www.opticsinfobase.org/abstract.cfm?URI=ICQI-2011-QTuE2.

[43] Pittman TB, Shih YH, Strekalov DV, Sergienko AV. Optical imaging by means of two-photon quantum entanglement. Physical Review A. 1995 Nov;52(5):R3429–R3432. Available from: http://link.aps.org/doi/10.1103/PhysRevA.52.R3429.

[44] Jack B, Yao AM, Leach J, Romero J, Franke-Arnold S, Ireland DG, et al. Entanglement of arbitrary superpositions of modes within two-dimensional orbital angular momentum state spaces. Physical Review A. 2010 Apr;81(4). Available from: http://link.aps.org/doi/10.1103/PhysRevA.81.043844.

[45] Lassen M, Delaubert V, Harb CC, Lam PK, Treps N, Bachor HA. Generation of Squeezing in Higher Order Hermite - Gaussian Modes with an Optical

Parametric Amplifier. Journal of the European Optical Society: Rapid Publications. 2006 Jun;1. Available from: https://www.jeos.org/index.php/jeos_rp/article/view/44.

[46] Liu K, Cui SZ, Yang RG, Zhang JX, Gao JR. Experimental Generation of Multimode Squeezing in an Optical Parametric Amplifier. Chinese Physics Letters. 2012 Jun;29(6):060304. Available from: http://stacks.iop.org/0256-307X/29/i=6/a=060304?key=crossref.7996b12912de76eaa3f8fbb8117e1449.

[47] Arnaud JA. Degenerate Optical Cavities. Applied Optics. 1969 Jan;8(1):189–195. Available from: http://ao.osa.org/abstract.cfm?URI=ao-8-1-189.

[48] Chalopin B, Scazza F, Fabre C, Treps N. Direct generation of a multi-transverse mode non-classical state of light. Optics Express. 2011 Feb;19(5):4405–4410. Available from: http://www.opticsexpress.org/abstract.cfm?URI=oe-19-5-4405.

[49] Morizur JF, Armstrong S, Treps N, Janousek J, Bachor HA. Spatial reshaping of a squeezed state of light. The European Physical Journal D. 2011 Jan;61(1):237–239. Available from: http://link.springer.com/article/10.1140/epjd/e2010-10616-x.

[50] Averchenko VA, Golubev YM, Filonenko KV, Fabre C, Treps N. Quantum correlations of pulses of optical parametric oscillator synchronously pumped above threshold. Optics and Spectroscopy. 2011 Jun;110(6):925–935. Available from: http://link.springer.com/article/10.1134/S0030400X11060026.

[51] McCormick CF, Boyer V, Arimondo E, Lett PD. Strong relative intensity squeezing by four-wave mixing in rubidium vapor. Optics letters. 2007;32(2):178180. Available from: http://www.opticsinfobase.org/ol/fulltext.cfm?uri=ol-32-2-178&id=119985.

[52] Boyer V, McCormick C, Arimondo E, Lett P. Ultraslow Propagation of Matched Pulses by Four-Wave Mixing in an Atomic Vapor. Physical Review Letters. 2007 Oct;99(14). Available from: http://link.aps.org/doi/10.1103/PhysRevLett.99.143601.

[53] Boyer V, Marino AM, Pooser RC, Lett PD. Entangled Images from Four-Wave Mixing. Science. 2008 Jul;321(5888):544–547. Available from: http://www.sciencemag.org/cgi/doi/10.1126/science.1158275.

[54] Glorieux Q, Guidoni L, Guibal S, Likforman JP, Coudreau T. Quantum correlations by four-wave mixing in an atomic vapor in a nonamplifying regime: Quantum beam splitter for photons. Physical Review A. 2011;84(5):053826. Available from: http://pra.aps.org/abstract/PRA/v84/i5/e053826.

[55] Corzo N, Marino AM, Jones KM, Lett PD. Multi-spatial-mode single-beam quadrature squeezed states of light from four-wave mixing in hot rubidium vapor. Optics Express. 2011;19(22):2135821369. Available from: http://www.opticsinfobase.org/oe/fulltext.cfm?uri=oe-19-22-21358.

[56] Marino AM, Clark JB, Glorieux Q, Lett PD. Extracting spatial information from noise measurements of multi-spatial-mode quantum states. The European Physical Journal D. 2012 Nov;66(11). Available from: http://link.springer.com/content/pdf/10.1140%2Fepjd%2Fe2012-30037-1.pdf.

[57] Turnbull MT, Petrov PG, Embrey CS, Marino AM, Boyer V. Role of the phase-matching condition in nondegenerate four-wave mixing in hot vapors for the generation of squeezed states of light. Physical Review A. 2013 Sep;88(3):033845. Available from: http://link.aps.org/doi/10.1103/PhysRevA.88.033845.

[58] Pich K, Leach J, Johnson AS, Salvail JZ, Kolobov MI, Boyd RW. Experimental realization of optical eigenmode super-resolution. Optics Express. 2012 Nov;20(24):26424–26433. Available from: http://www.opticsexpress.org/abstract.cfm?URI=oe-20-24-26424.

[59] Beskrovnyy V, Kolobov M. Quantum limits of super-resolution in reconstruction of optical objects. Physical Review A. 2005 Apr;71(4). Available from: http://link.aps.org/doi/10.1103/PhysRevA.71.043802.

[60] Loudon R. The quantum theory of light. Oxford; New York: Oxford University Press; 2000.

[61] Fock V. Note to the Quantification of the harmonic Oscillator in a Magnetic Field. Zeitschrift Fur Physik. 1928 May;47(5-6):446–448. WOS:000207399000013.

[62] Glauber RJ. Coherent and incoherent states of the radiation field. Physical Review. 1963;131(6):2766. Available from: http://prola.aps.org/abstract/PR/v131/i6/p2766_1.

[63] Loudon R, Knight P. Squeezed Light. Journal of Modern Optics. 1987 Jun;34(6-7):709–759. Available from: http://www.tandfonline.com/doi/abs/10.1080/09500348714550721.

[64] Walls DF, Zoller P. Reduced Quantum Fluctuations in Resonance Fluorescence. Physical Review Letters. 1981 Sep;47(10):709–711. Available from: http://link.aps.org/doi/10.1103/PhysRevLett.47.709.

[65] Mandel L. Squeezed states and sub-Poissonian photon statistics. Physical Review Letters. 1982;49(2):136. Available from: http://prl.aps.org/abstract/PRL/v49/i2/p136_1.

[66] Breitenbach G, Schiller S, Mlynek J. Measurement of the quantum states of squeezed light. Nature. 1997 May;387(6632):471–475. Available from: http://www.nature.com/nature/journal/v387/n6632/full/387471a0.html.

[67] Casimir HBG. On the Attraction Between Two Perfectly Conducting Plates. FrontPhys, KonNedAkadWetenschProc, IndagMath. 1948;100N3-4, 10, 51, 65:61–63, 342–344, 793–795, 261–263. Available from: http://inspirehep.net/record/24990?ln=en.

[68] Casimir HBG, Polder D. The Influence of Retardation on the London-van der Waals Forces. Physical Review. 1948 Feb;73(4):360–372. Available from: http://link.aps.org/doi/10.1103/PhysRev.73.360.

[69] Lamb WE, Retherford RC. Fine Structure of the Hydrogen Atom by a Microwave Method. Physical Review. 1947 Aug;72(3):241–243. Available from: http://link.aps.org/doi/10.1103/PhysRev.72.241.

[70] Einstein A, Podolsky B, Rosen N. Can Quantum-Mechanical Description of Physical Reality Be Considered Complete? Physical Review. 1935 May;47(10):777–780. Available from: http://link.aps.org/doi/10.1103/PhysRev.47.777.

[71] Heidmann A, Horowicz RJ, Reynaud S, Giacobino E, Fabre C, Camy G. Observation of quantum noise reduction on twin laser beams. Physical Review Letters. 1987;59(22):25552557. Available from: http://link.aps.org/doi/10.1103/PhysRevLett.59.2555.

[72] Collett M, Loudon R, Gardiner C. Quantum-Theory of Optical Homodyne and Heterodyne-Detection. Journal of Modern Optics. 1987 Jul;34(6-7):881–902. WOS:A1987J991300010.

[73] Hecht E. Optics. Reading, Mass.: Addison-Wesley; 2002.

[74] Boyd RW. Nonlinear Optics. Academic Press; 2008.

[75] Franken PA, Hill AE, Peters CW, Weinreich G. Generation of Optical Harmonics. Physical Review Letters. 1961 Aug;7(4):118–119. Available from: http://link.aps.org/doi/10.1103/PhysRevLett.7.118.

[76] Burnham DC, Weinberg DL. Observation of Simultaneity in Parametric Production of Optical Photon Pairs. Physical Review Letters. 1970 Jul;25(2):84–87. Available from: http://link.aps.org/doi/10.1103/PhysRevLett.25.84.

[77] Pooser RC, Marino AM, Boyer V, Jones KM, Lett PD. Quantum correlated light beams from non-degenerate four-wave mixing in an atomic vapor: the D1 and D2 lines of ^{85}Rb and ^{87}Rb. Optics express. 2009;17(19):1672216730. Available from: http://www.opticsinfobase.org/abstract.cfm?URI=oe-17-19-16722.

[78] Steck DA. Rubidium 85 D line data; 2001. Available from: http://www.steck.us/alkalidata/rubidium87numbers.pdf.

[79] Marino AM. Experimental studies of two-mode squeezed states in rubidium vapor. ProQuest Dissertations And Theses; Thesis (PhD)–University of Rochester, 2006; Publication Number: AAI3245848; Source: Dissertation Abstracts International, Volume: 67-12, Section: B, page: 7147; 184 p. 2006;Available from: http://adsabs.harvard.edu/abs/2006PhDT.....226M.

[80] Lukin MD, Hemmer PR, Löffler M, Scully MO. Resonant Enhancement of Parametric Processes via Radiative Interference and Induced Coherence. Physical Review Letters. 1998 Sep;81(13):2675–2678. Available from: http://link.aps.org/doi/10.1103/PhysRevLett.81.2675.

[81] Caves CM. Quantum limits on noise in linear amplifiers. Physical Review D. 1982;26(8):1817. Available from: http://prd.aps.org/abstract/PRD/v26/i8/p1817_1.

[82] Glorieux Q. ETUDE THEORIQUE ET EXPERIMENTALE DES CORRELATIONS QUANTIQUES OBTENUES PAR MELANGE A QUATRE ONDES DANS UNE VAPEUR ATOMIQUE. Université Paris-Diderot-Paris VII; 2010. Available from: http://hal.archives-ouvertes.fr/tel-00558505/.

[83] Jasperse M, Turner LD, Scholten RE. Relative intensity squeezing by four-wave mixing with loss: an analytic model and experimental diagnostic. Optics Express. 2011 Feb;19(4):3765–3774. Available from: http://www.opticsexpress.org/abstract.cfm?URI=oe-19-4-3765.

[84] Lukin MD, Hemmer PR, Scully MO. Resonant nonlinear optics in phase-coherent media. In: Bederson B, Walther H, editors. Advances in Atomic Molecular, and Optical Physics, Vol. 42. vol. 42. San Diego: Elsevier Academic Press Inc; 2000. p. 347–386.

[85] Harris SE, Field JE, İmamoğlu A. Nonlinear optical processes using electromagnetically induced transparency. Physical Review Letters. 1990;64(10):11071110. Available from: http://link.aps.org/doi/10.1103/PhysRevLett.64.1107.

[86] Boller KJ, İmamoğlu A, Harris SE. Observation of electromagnetically induced transparency. Physical Review Letters. 1991 May;66(20):2593–2596. Available from: http://link.aps.org/doi/10.1103/PhysRevLett.66.2593.

[87] Figueroa E, Vewinger F, Appel J, Lvovsky AI. Decoherence of electromagnetically induced transparency in atomic vapor. Optics Letters. 2006 Sep;31(17):2625–2627. Available from: http://ol.osa.org/abstract.cfm?URI=ol-31-17-2625.

[88] Arditi M, Carver TR. Pressure, light, and temperature shifts in optical detection of 0-0 hyperfine resonance of alkali metals. Physical Review. 1961;124(3):800. Available from: http://prola.aps.org/abstract/PR/v124/i3/p800_1.

[89] Corwin KL, Lu ZT, Hand CF, Epstein RJ, Wieman CE. Frequency-Stabilized Diode Laser with the Zeeman Shift in an Atomic Vapor. Applied Optics. 1998 May;37(15):3295–3298. Available from: http://ao.osa.org/abstract.cfm?URI=ao-37-15-3295.

[90] Chron B, Gilles H, Hamel J, Moreau O, Sorel H. Laser frequency stabilization using Zeeman effect. Journal de Physique III. 1994 Feb;4(2):401–406. Available from: http://jp3.journaldephysique.org/articles/jp3/abs/1994/02/jp3v4p401/jp3v4p401.html.

[91] Boyer V, Arimondo E, Lett PD. Strong relative intensity squeezing by four-wave mixing in rubidium vapor. Optics letters. 2007;32(2):178180. Available from: http://www.opticsinfobase.org/abstract.cfm?id=119985.

[92] Zhang J. Einstein-Podolsky-Rosen sideband entanglement in broadband squeezed light. Physical Review A. 2003 May;67(5). Available from: http://link.aps.org/doi/10.1103/PhysRevA.67.054302.

[93] Schori C, Srensen JL, Polzik ES. Narrow-band frequency tunable light source of continuous quadrature entanglement. Physical Review A. 2002 Sep;66(3). Available from: http://link.aps.org/doi/10.1103/PhysRevA.66.033802.

[94] Marino AM, Stroud Jr CR, Wong V, Bennink RS, Boyd RW. Bichromatic local oscillator for detection of two-mode squeezed states of light. JOSA B. 2007;24(2):335339. Available from: http://www.opticsinfobase.org/josab/fulltext.cfm?uri=josab-24-2-335&id=125575.